MODELING SOIL SURFACE ROUGHNESS WITH DUAL-POLARIZATION ADVANCED SYNTHETIC APERTURE RADAR (ASAR) IMAGERY

By Kerstin Haslinger

A Thesis

Submitted in Partial Fulfillment

of the Requirements for the Degree of

Master of Arts

in Rural Geography

Northern Arizona University

May 2010

Approved:

_____

Ruihong Huang, Ph.D., Chair

_____

Alan Lew, Ph.D.

_____

Erik Schiefer, Ph.D.

ABSTRACT

MODELING SOIL SURFACE ROUGHNESS WITH DUAL-POLARIZATION ADVANCED SYNTHETIC APERTURE RADAR (ASAR) IMAGERY

KERSTIN HASLINGER

Soil surface roughness was modeled using the Integral Equation Model (IEM) which is based on radar backscatter as a function of soil surface roughness and soil surface moisture. The inputs to the IEM are the two backscatter bands from an ASAR dual-polarization image taken over the Hopi Reservation in northeast Arizona in May 2004. Output are two models of the parameters root mean squared height (h_{RMS}) and correlation length (L_c), both of which are generated by the IEM. Results showed that there is weak correlation between the in-field h_{RMS} and the modeled parameters on field scale. Error could be caused by the coarse interval used to determine the modeled h_{RMS}. This research could be employed in agricultural decision-making.

ACKNOWLEDGEMENTS

I sincerely express my gratitude to my advisor Dr. Ruihong Huang, Dr. Alan Lew, and Dr. Erik Schiefer for their support and would like to thank them for serving on my thesis committee.

I would like to thank Robert Weber and Glenn Dunno of Pinnacle Mapping Technologies for their support in providing me the required ASAR image and field data.

TABLE OF CONTENTS

LIST OF TABLES

LIST OF FIGURES

DEDICATION

I would like to dedicate this research to my daughter Erin.

CHAPTER 1 – INTRODUCTION

In the past, mapping of soil surface properties, that is soil moisture, soil texture, and soil roughness, has been a tedious undertaking, which required an enormous amount of fieldwork and yielded data restricted to the sampled points only (Taylor 1961; Johnson 1962). With the emergence of remote sensing tools on airborne and orbital platforms, it became easier to track soil surface properties using thermal imagery as well as radar imagery, though the methods used were still flawed (Hanks 1980; Heidmann 1990; Fung, Li, and Chen 1992; Ulaby, Batlivala, and Dobson 1978). During the last decade, research advanced a great deal in terms of soil surface properties detection via remote sensing (Ulaby et al. 1996; Ridley et al. 1996; Taconet et al. 1996; Chen et al. 1995; Benallegue et al. 1995; Engman and Chauhan 1995; Dobson et al. 1995; Taconet et al. 1994; Troch 1996; Altese et al. 1996). Synthetic aperture radar (SAR), a type of radar system that uses an antenna which can cover large areas, became the tool of choice for many scientists, considering the fact that the physical properties of microwave radar interact especially with the dielectric property of water (Moran et al. 2000; Moeremans and Dautrebande 2000; Wagner et al. 1999; Tansey et al. 1999; Meade et al. 1999; Saarenketo 1998; Schoups et al. 1998; Engen and Johnson 1999). The dielectric property is an indicator of radar reflectivity (the higher the dielectric constant, the more reflection of radar beams).

There still are questions, however, above all about the accuracy of soil moisture predictions by use of SAR, especially when using the C-band range. This range of relatively short wavelengths is too short to be effective enough for deep surface penetration; it commonly penetrates only up to 5 cm depth, given favorable

circumstances (Avery and Berlin 1992; D'Urso and Minacapilli 2006; Altuncu, Akduman, and Yapar 2007; Svoray and Shoshany 2004; Baghdadi and Zribi 2006). Several factors, such as vegetation and soil texture, are also of importance for a reliable interpretation of a SAR scene, thus complicating C-band SAR predictions of soil properties. To overcome these complications, a few models have been constructed which analyze the radar backscatter in terms of soil properties. One of these is the Integral Equation Model (IEM) which replicates radar backscatter as a function of soil surface height (root mean squared height or h_{RMS}), correlation length (L_C), and soil surface moisture (Θ_S) (Bindlish and Barros 2000; Baghdadi et al. 2004; Rahman et al. 2008; Baghdadi and Zribi 2006; Baghdadi, Holah, and Zribi 2006). The h_{RMS} measures the standard deviation of corresponding mean soil surface height in centimeters (Rahman et al. 2007; Bryant et al. 2007). The correlation length L_C describes the length between two points at a distance beyond which the heights of a rough surface are no longer correlated to each other (Rahman et al. 2007; Mela and Louie 2001), it is an index of homogeneity measuring the furthest distance from a point at which the soil surface height is still the same. Any roughness height values beyond the correlation length are considered entirely random.

This study examines soil surface roughness prediction using C-band SAR imagery for mostly homogeneously, barely vegetated semi-arid to arid rangeland, based on the IEM. An IEM derived methodology for the prediction of the soil surface roughness parameter h_{RMS} is applied to an Envisat Advanced Synthetic Aperture Radar (ASAR) alternating polarization image by use of a Geographic Information System (GIS). With

a successful prediction of soil surface roughness, a deduction about soil surface moisture would be possible.

CHAPTER 2 – LITERATURE REVIEW

SOIL PROPERTIES RETRIEVAL USING SAR SYSTEMS

Earlier work in soil properties detection via SAR concentrated on radar wavelengths of the L-band frequency (Engman and Chauhan, 1995). The L-band has a frequency of approximately 1 to 2 GHz and its wavelength ranges from 15 to 30 cm (Avery and Berlin, 1992, 162). This band allows for surface penetration to a depth substantial for soil moisture detection, but may be hindered by inopportune properties of the cover and subsurface materials. At the turn of the 21st century, the SAR band used for soil roughness and moisture detection changed to C-band, a fact which is most likely due to availability and affordability of C-band images (Zribi and Dechambre, 2003; Moran et al., 2002; Moran et al., 2000; Magagi and Kerr, 2001). The C-band has an approximate frequency of 4 to 8 GHz (Sullivan 2000, 8) and its wavelength ranges from 3.8 to 7.5 cm (Avery and Berlin 1992, 162). Because of its shorter wavelength λ, the C-band signals cannot reach to the same subsurface depth as L-band signals, thus restricting it to soil surface parameters. As an example, a C-band signal of 5.35 GHz penetrates to an average depth of about 5 cm (Moran et al. 2000).

The shallow subsurface backscattering, meaning the radar beams are reflected by subsurface material rather than by dielectric property, attained by the C-band SAR system is a relatively new method for soil surface properties detection, which appeared first in published peer-reviewed articles around 1998. At the time, its application was usually complimented or validated by other methods, such as applications using thermal imagery of the same location and access time, soil indices, statistics, or hydrologic

models (Zribi and Dechambre 2003; Moran et al. 2002; Magagi and Kerr 2001; Chehbouni et al. 2001). Several of the older articles reviewed for this research project discuss the validation of soil moisture rates and soil roughness parameters detected by C-band SAR systems, which confirms that researchers are still looking for a fast and easy-to-use, yet reliable method for soil surface properties detection via SAR systems.

ENVISAT ASAR

The European Space Agency (ESA, 2004) launched its Envisat satellite into a sun-synchronous flight path (meaning it mimics the sun's motion across the sky) on March 1st, 2002 and started the data acquisition four days later (Figure 1). By January 2004, Envisat completed its 10,000th orbit, the equivalent of 450 million kilometers of travel.

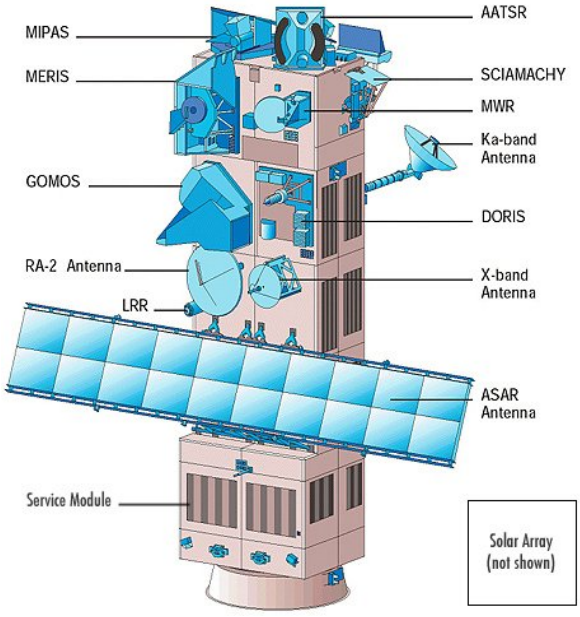

Figure 1. The Envisat satellite (Source: ESA 2005).

The satellite is orbiting the earth from pole to pole fourteen times a day at an altitude of roughly 800 kilometers and a speed of 7.45 km/s (European Space Agency, 2005).

According to ESA, the satellite repeats its reference orbit once every 35 days (501 orbits in a cycle) which translates to complete coverage of the globe in one to three days for most of its sensors. Onboard the satellite is a payload of a dozen remote sensing tools, one of which is called ASAR, an acronym that stands for "Advanced Synthetic Aperture Radar". ASAR is independent of weather and works during the day as well as at night (Desnos et al., 2000). The ASAR remote sensing tool makes use of a matrix of incidence angles (the angle at which the beam reaches the earth's surface) and polarizations (the orientation of the oscillation of the radar waves, either vertical or horizontal) with the result of 37 different operating modes (ESA, 2004). This allows for a multitude of applications, both at regional and global scale, that include monitoring of ice-sheets, oceans, agriculture and forestry, surface elevation, geology, topography, hydrology, flooding, and vegetation (Desnos et al., 2000; European Space Agency, 2005). The multitude of operating modes, however, consequently calls for a new way of testing the accuracy of the ASAR backscatter performance. The outcome of these tests provides an average radiometric resolution of 1.7 dB and an average noise equivalent (measures the sensitivity of the radar system) of approximately 23 dB across all possible operation modes. At the same time, the average radiometric stability (a measure of precision) is 0.47 dB. The average spatial resolution (azimuth x range) at alternating polarizations for all ASAR products is 29 m x 30 m.

Due to the fact that ASAR uses an active antenna which can cause gain and phase instabilities, a threefold of radiometric calibrations has been devised, made up of internal and external calibration, as well as external characterization (Desnos et al., 2000; ESA, 2004). The calibration includes algorithms like chirp replica construction

(a correlation function which adjusts the SAR backscatter) and elevation gain (backscatter amplification) monitoring. The external characterization is done by use of an image of the Amazon rainforest, which is known for being "a stable, large-scale, isotropic distributed target with a relatively high backscatter and a well-understood relationship between backscatter and incidence angle" (ESA 2004: 2.11.4.1). The absolute calibration of the ASAR operating mode used for this study is further discussed in the methodology.

According to the Envisat-1 Products Specifications, the Level 0 Alternating Polarization (AP) product consists of time ordered Annotated Instrument Source Packets (AISPs) which are collected in the instrument's image mode. In the case of the data used for this study, the alternating polarization (AP) cross-polar H Level 0 is used which has a polarization combination of horizontal / horizontal (HH) and horizontal / vertical (HV). These two polarizations are co-registered within 0.25 of a sample.

The Alternating Polarization Ellipsoid Geocoded Image (AP_APG) is a Level 1 product that has been generated from an AP cross-polar H Level 0 product by use of SPECAN (spectral analysis) algorithm, corrections, and relative calibration. The AP_APG imagery used in this study is geolocated and resampled to WGS-84, Lat Long map projection.

The geometric sampling has a pixel spacing of 12.5 m by 12.5 m (European Space Agency 2005). The geometric accuracy as given by the Envisat Products Specifications is 25 m. The algorithms used for generation of the AP-APG imagery include: data decompression; raw data correction; calibration pulse processing; antenna elevation

gain function calculation; noise power estimation; image formation (SPECAN); geolocation; and map projection resampling.

THE INTEGRAL EQUATION MODEL

These complex derivations take into account Fourier transforms (W^m, a kind of signal processing) of the surface correlation coefficient, Fresnel reflection coefficients (description of wave reflection), and Kirchhoff surface Field Coefficients (F_{qp}, F_{qp}^*, description of wave scattering on rough surfaces). Baghdadi et al. further calibrated the formula with semi-empirical values for the optimal correlation length (L_{opt}) so that it can be used especially on bare agricultural soils (Baghdadi et al. 2004).

The IEM is a physical model established on electromagnetic scattering theories, thus it can be applied on any surface conditions or radar set-up, while statistical models are only valid for like radar and surface conditions as in the experimental set-up they are derived from (Baghdadi et al. 2004). With the IEM, radar backscatter σ^0 is predicted as a function of sensor configuration and surface conditions that simplified can be stated as

$$\sigma^0 = f(\Theta_S, h_{RMS}, L_C)$$

whereby all three parameters (soil surface moisture Θ_S, soil roughness h_{RMS}, and correlation length L_C) are typically unknown parameters (Rahman et al. 2007). By inversion of this function, one can predict each of the soil surface parameters by substituting the other two parameters with calibration data (for example by in-field measurements).

Rahman et al. developed an inversion of the IEM using a so-called dry scene where the soil moisture content is minimal, thus leaving only the two soil roughness

parameters as unknowns (Rahman et al. 2007). This allows for an accurate prediction of the soil surface roughness parameters. Because the correlation length L_C is directly related to the soil surface roughness h_{RMS}, it is then possible to construct a valid derivation of the correlation length. In turn, with the correlation length known, the IEM can be used to estimate the soil roughness parameter h_{RMS} (Rahman et al. 2008). Rahman et al. expanded their research to predict soil surface moisture, now that they derived both roughness parameters. For their study, the authors used multi-angle ASAR imagery, meaning imagery with more than one incidence angle. In their conclusion, Rahman et al. noted that the alternative multi-polarization imagery (i.e. AP_APG) would be advantageous, because it would do away with registration errors that may happen when matching multi-angle imagery.

EFFECT OF VEGETATION

Depending on the wavelength of the radar beam, the backscatter will include vegetation. As a general guideline it can be said that the longer the wavelength, the better the penetration of vegetation by the radar beam (Jensen 2007). Therefore, an X-band radar with a wavelength of less than 3 cm will result in a backscatter of the top part of the vegetation present at the site, while an L-band radar with a wavelength of more than 20 cm will result in a backscatter that includes the entire vegetation as well as the soil surface. Therefore, C-band radar with a wavelength range from 3.8 to 7.5 cm will produce backscatter that penetrates vegetation to some degree. This, of course, depends on the height of the vegetation: a forest with tall trees will require longer wavelength to penetrate than ankle-high grasses. According to Moran in her email, the following applies to C-band radar backscatter on vegetation (Moran 2008):

> "a) the C-band radar seems to penetrate our sparse grassland vegetation (LAI<1) and particularly so when it is dry;
> b) we found that radar could be used to map shrub density (so it is more sensitive to woody vegetation, even though vegetation is sparse); …"

This means that the vegetation present at the site, measured by the LAI (leaf area index), will not alter the radar backscatter over all, if the vegetation of the study site consists of sparse, dried-out grasses and is void of woody vegetation.

In an article by Thoma et al., the authors adjusted the scale of the radar imagery in order to rid the image of backscatter errors due to vegetation (Thoma et al. 2008). Their imagery had an original resolution of 7 m x 7 m per pixel. The authors used a 5x5 median filter to reduce speckle, followed by a spatial averaging of the image to obtain higher accuracy. The resulting image had to be adjusted due to filtering and averaging, resulting in a product that had a resolution of 162 m x 162 m per pixel for their watershed site in southern Arizona (Walnut Gulch Experimental Watershed). The article by Thoma et al. is complementing an article by Hutchinson on the detection of near-surface soil moisture in grasslands of Kansas (Hutchinson 2003). In his study, Hutchinson concluded that C-band radar is "capable of monitoring general near-surface soil moisture conditions over highly productive vegetated ecosystems such as tallgrass prairie" (Hutchinson 2003, 234-235). . Though that study focused on soil surface moisture retrieval, it also validates this soil surface roughness study: both soil surface moisture and soil surface roughness are measured at the same level (i.e. at the soil surface) and both parameters are included in the IEM. Furthermore, the study sites in Kansas and southern Arizona feature more and denser vegetation than the study site used for this research project, thus vegetation is no hindrance in terms of C-band radar backscatter.

CHAPTER 3 – DATA ACQUISITION AND PROCESSING

STUDY SITE

This research is designed for soil surface properties detection on semi-arid to arid rangeland. A location suitable for this study features sparse, homogeneously distributed short vegetation. Also it should not feature rocks or rock fragments (surface or subsurface). The study site offers a wide variety of locales for random field sampling; at least 30 samples are needed for a viable statistical analysis. Furthermore, the sampled locations have to be either level surface or of gentle slope to (a), ensure an even distribution of soil surface properties over a large area, and (b), reduce the risk of topology error of the radar image analysis.

The Hopi Reservation is most suitable for this study, because it fulfills all the above requirements. An already ongoing project --an analysis of soils on the Hopi Reservation suitable for agriculture by Pinnacle Mapping Technologies (Flagstaff, Arizona) from May 2004-- provided the ASAR data and soil surface properties sample information needed for this study. Said project and the use of its data for this study were authorized by the Hopi Tribe's Department of Natural Resources, Water Resources Program, Consulting Agreement #03-050, and supervised by Mr. Nat Nutongla. Aside from sampling of soil moisture rates at depth, surface roughness and soil texture throughout the reservation conducted by Pinnacle Mapping Technologies, no other fieldwork was necessary. Because of this study's focus on soil surface properties modeling via ASAR data, site descriptions were general only; out of respect for the Hopi Tribe, any possible cultural location were neither studied nor mentioned in this study.

The Hopi Reservation is located on the Colorado Plateau at an approximate elevation of 5,675 feet (according to GPS data available for this study) (Map 1). Though the area features buttes, mesas, and rolling hills, the sample sites are all located on level ground (Figure 1). The sample sites all have a slope of less than 5%, most of them are considered flat (less than 2% slope). The vegetation is sparse, composed mainly of desert grasses (Figure 2). Most of the grasses are short (in at least one case due to overgrazing)(Figure 3), sometimes accompanied by short brush like snakeweed, saltbush, or sage. A few of the sites also feature scattered taller bushes like Mormon tea or pinion pine with juniper in the distance (Figure 5). A biological or organic soil crust has been noted at only two sample sites, which have been determined shrubland, featuring mainly saltbush and snakeweed. Most of the other sample sites have a crust of dried topsoil that may be a sign of high clay or clay-sized particle content (Figure 4). For the most part, this crust is easily disturbed, meaning it crumbles when lightly touched. At some sites, the crust consists of a thick layer of baked topsoil with mudcracks (Figure 6). None of the sample sites include rock fragments at or below the surface. Though there is a site where the soil has been compacted (fragipan), the majority of sample sites consist of sandy material.

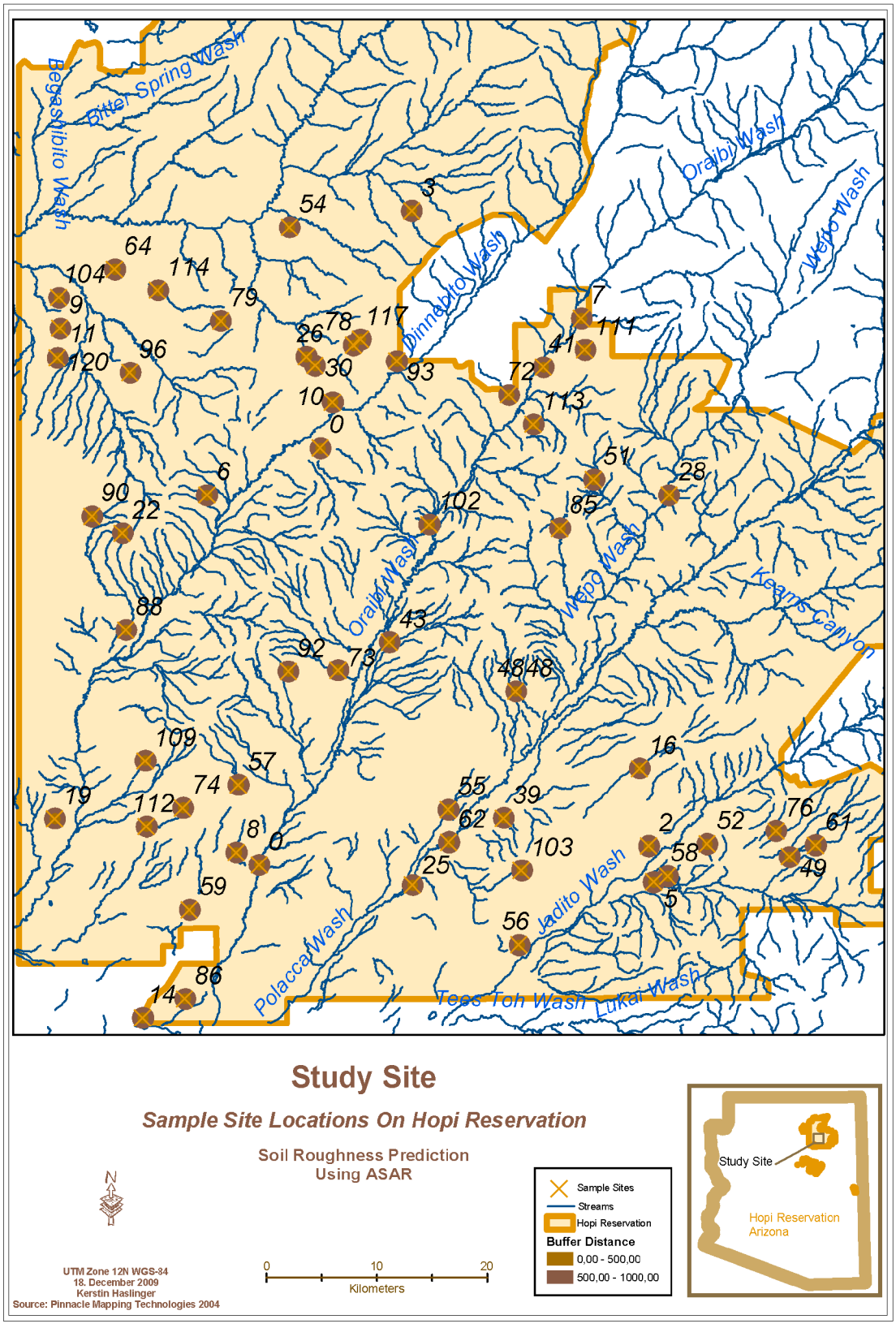

Figure 2. Study Site: Sample Site Locations on Hopi Reservation.

Figure 3. Sample site 88. Desert grasses and snakeweed are prominent at this sample site.

Figure 4. Sample site 79. Vegetation is extremely short and dried out; the patches of desert grass are overgrazed.

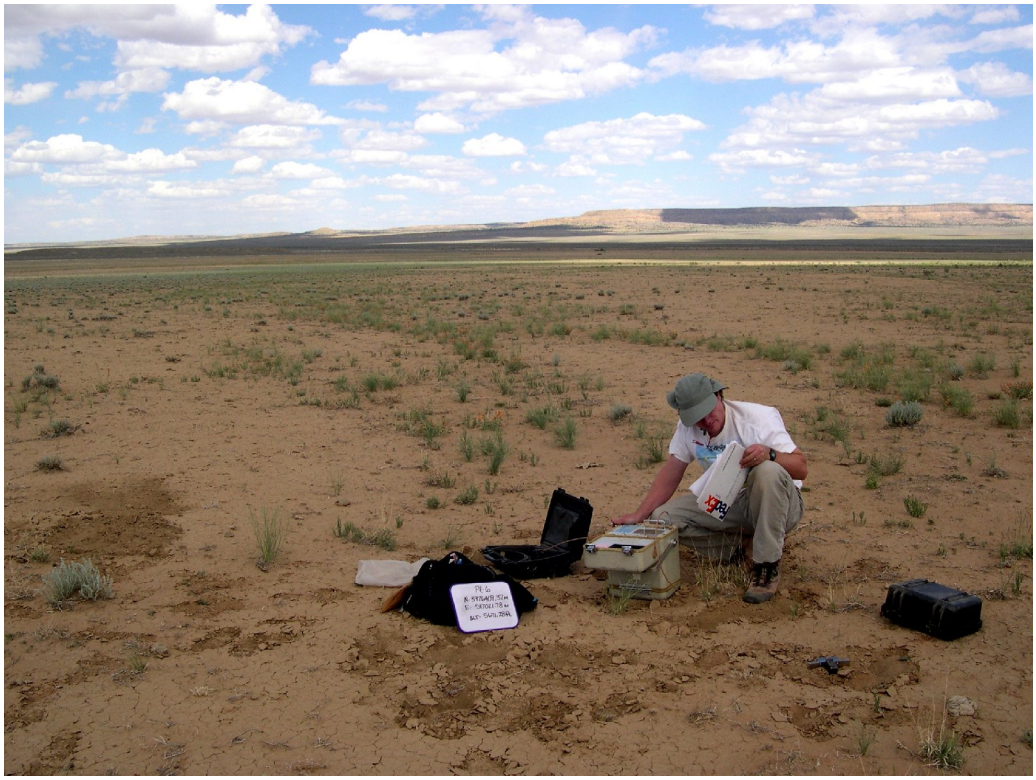

Figure 5. Sample site 6. The soil is covered by a clayey crust that crumbles easily when disturbed (for example, by walking on it).

Figure 6. Sample site 117. Here, also, an easily disturbed clayey crust covers the sandy soil. Visible in the distance is a patch of scattered pinion pine and juniper.

Figure 7. Sample site 55. The thick clay crust at this site shows signs of the mudcrack pattern usual for a dry playa.

Figure 8. Sample site 3. Short grasses and brush are spread over a crusted sandy soil.

Data Acquisition and Preparation

With permission of the Hopi tribe, the author of this research through Pinnacle Mapping Technologies obtained ASAR data. The radar imagery was further described in the header analysis below. The ASAR image was taken on May 8, 2004, which makes the image a "dry scene", meaning there has been little rainfall and the soil moisture content is very low.

Other information necessary for this study included GIS layers of hydrology, soil types, and infrastructure present on the reservation; a Digital Elevation model (DEM); and data collected in the field May 7 to 9, 2004. The sample sites were generated by random, using slope as the main characteristic to ensure a reasonably flat surface. The field data products consisted of gravimetric and volumetric soil moisture rates, GPS locations, vegetation profiles, soil texture categorization, and micro-relief calculations for each of the 70 sample sites.

In the field, several procedures were completed at each sample site. First, a volumetric soil moisture measurement was taken at a depth of 0 to 20 cm, using one of three products: ESI MP-917, Campbell Scientific TDR 100 and TRASE. A soil sample of roughly 250 g was collected and stored in an airtight bag for further analysis. The vegetation in the vicinity of the sample site was recorded. Digital photographs were taken to document the surrounding area of each sample site. The soil surface roughness was traced several times in the immediate neighborhood (< 10 m) of the sample site by use of a pin-meter, consisting of 50 one-centimeter diameter rods that record the local elevation at micro-scale level.

At the lab, the field data were then transcribed into an Excel table that was used for several calculations. First, the radar reflectivity of the study site was checked by means of the Raleigh Criterion and the Peak & Oliver Modified Criterion. Both criterions are indicators of soil surface roughness respective to radar scattering and penetration. The Peak & Oliver Modified Criterion features an intermediate category and therefore allows for more detailed distinguishing than the Raleigh Criterion that only decides between smooth and rough surfaces. For this study, the Raleigh Criterion was determined by the formula $h_{RMS} > \frac{\lambda}{8 * \cos\Theta}$ for rough surfaces, and the Peak & Oliver Modified Criterion by $h_{RMS} < \frac{\lambda}{25 * \cos\Theta}$ for smooth, $\frac{\lambda}{25} < h_{RMS} < \frac{\lambda}{4.4 * \cos\Theta}$ for intermediate and $h_{RMS} > \frac{\lambda}{4.4 * \cos\Theta}$ for rough surfaces, where λ = 5.3GHz. The two criterions were evaluated at maximum (43.5°), average (41.2°), minimum (38.9°), and random incidence angle Θ (40.5°) in order to check the full range of possible outcomes (Appendix A). The results, especially those of the Peak & Oliver Modified Criterion calculations, indicated that generally all sample sites are suitable for this study. The reflectivity calculations were stored in an Excel table.

In this Excel workbook, called "FieldDataWork" (FDW), each sample site was a record with the site number and a unique ID. The UTM easting, northing, and elevation also functioned as an identifier. Another column in the table was set up for the dominant vegetation. The vegetation as described in the field was stored in the Excel workbook (Appendix B), where the different types of vegetation in general and plants in

particular, as well as the decision about the dominant vegetation (e.g. grasses versus shrubs) were recorded.

Also recorded in the Excel workbook was the soil moisture information (Appendix C). The soil samples collected in the field were taken to the U.S. Forestry Service's soil laboratory on campus for gravimetric soil moisture analysis. There, portions of roughly 100 g of each sample were weighed before and after a 24-hour drying period. For each sample site, the resulting difference between wet and dried soil was used to compute the soil moisture percentage present. Also, the gravimetric water content was calculated by the formula $w = \frac{m_w}{ms}$, where w is the gravimetric water content, m_w the mass of water, and m_s the mass of dry soil (van Es and Ogden 1997). The in-field volumetric soil moisture measurements, taken with three different probes and calibrated by Pinnacle Mapping Technologies, were also recorded in the table. Because the probes averaged the soil moisture data for a soil column from top to 20cm depth, the resulting volumetric soil moisture data were used only as an approximation in the decision on whether the May 2004 ASAR image could be used as a "dry scene" or not. However, the gravimetric soil moisture test, though from samples at depth, resulted in a mean gravimetric water content of 0.06 m^3m^{-3} for all sample sites. Digging out the soil samples, the common observation was that soil moisture increased with depth which further supported the decision that the top soil had to be drier than the gravimetric water content of the soil samples. A gravimetric water content between 0.02 m^3m^{-3} and 0.08 m^3m^{-3} was considered dry (Rahman et al. 2007), and therefore the May 2004 ASAR image could indeed by used as a "dry scene".

For the soil texture analysis, a methodology has been devised after consulting several authors' analyses (Birkeland 1999; Integrated Publishing 2004; Western Upper Peninsula Center for Science 2004; Francek and Valek 2004; Butler 2004; Gerakis and Baer 1999). The remaining share of all soil samples, about 150 g, was left to dry out at room temperature, each sieved with a 4 mm sieve to rid the soil sample of all larger particles (of which there were only a few), then portioned to a 100 g sample. These weighed samples were then, one-by-one, analyzed for soil texture consistency by use of a shaker at the Northern Arizona University Forestry department's soil science laboratory. The shaking apparatus consists of several mesh grids, stacked from coarse to fine: $2mm > x > 1mm$ and $1mm > x > 0.5mm$ for sand, $0.5mm > x > 0.063mm$ for silt, and $0.063mm > x$ for clay distinction. Each sample was shaken at a constant rate for a set time period of 15 minutes, and the content left in each of the mesh grids was weighed individually. These recorded weights were then converted into percentages using an Excel table in the FDW workbook. The subsequent soil type classification was based on these percentages and was done in part with the soil texture triangle software called TRIANGLE by Gerakis and Baer (Gerakis and Baer 1999). The results showed that soils were mostly of silt loam, followed by silt and sandy loam (Appendix D). The clay content in all of the soils was less than 10%.

The root mean square height (h_{RMS}) of each sample site was calculated by the formula $\sqrt{\left(\frac{1}{n} * \sum_{i}^{n} (z_i - z)\right)^2}$, where z is the mean height measurement, z_i is an individual height measurement, and n is the count of height measurements. There were several pinmeter readings taken at each sample site, but only one data set of averaged

height measurements per sample site is currently available for this study. The h_{RMS} equation was applied on these averaged readings (by use of an Excel table in the FDW) and therefore the results were only approximations (Appendix E).

All results were combined in an Excel table in the WDF workbook (Appendix F). This table was converted to dBase IV (DBF) format in order to employ it in an ArcGIS project. The field data results table was imported into a new ArcGIS project and the XY data were displayed using the table fields "Easting" and "Northing" from the GPS locations as X and Y fields, respectively. Though ArcView reported that the XY data event layer had no known projection, the GPS locations were in UTM Zone 12N WGS-84. Two buffered layers of the sample site event layer were created with buffer radiuses of 110 m and 200 m. For their study of the Walnut Gulch Experimental Watershed, Rahman et al. used an initial buffer of 110 m x 110 m in their study (Rahman et al. 2008) which they widened to 150 m x 150 m due to image registration errors. Such image registration errors were not present in this study because of the use of dual band imagery, therefore a 110m x 110m buffer was deemed sufficient. Thoma et al. argued that best results could be achieved with the driest soils at broadest scale (Thoma et al. 2008). The authors found that a ground resolution of 162 m was the smallest effective resolution for their Walnut Gulch Experimental Watershed study site (same as used by Rahman et al.). For this study, a second buffer with an increase in buffer radius of approximately 80 percent (= 200m) was chosen to verify or contrast results of the initial 110 m buffer radius (Figure 9). Figure 9 also depicts the variety of pixel values possible in side the buffers which may have negatively influenced the final results.

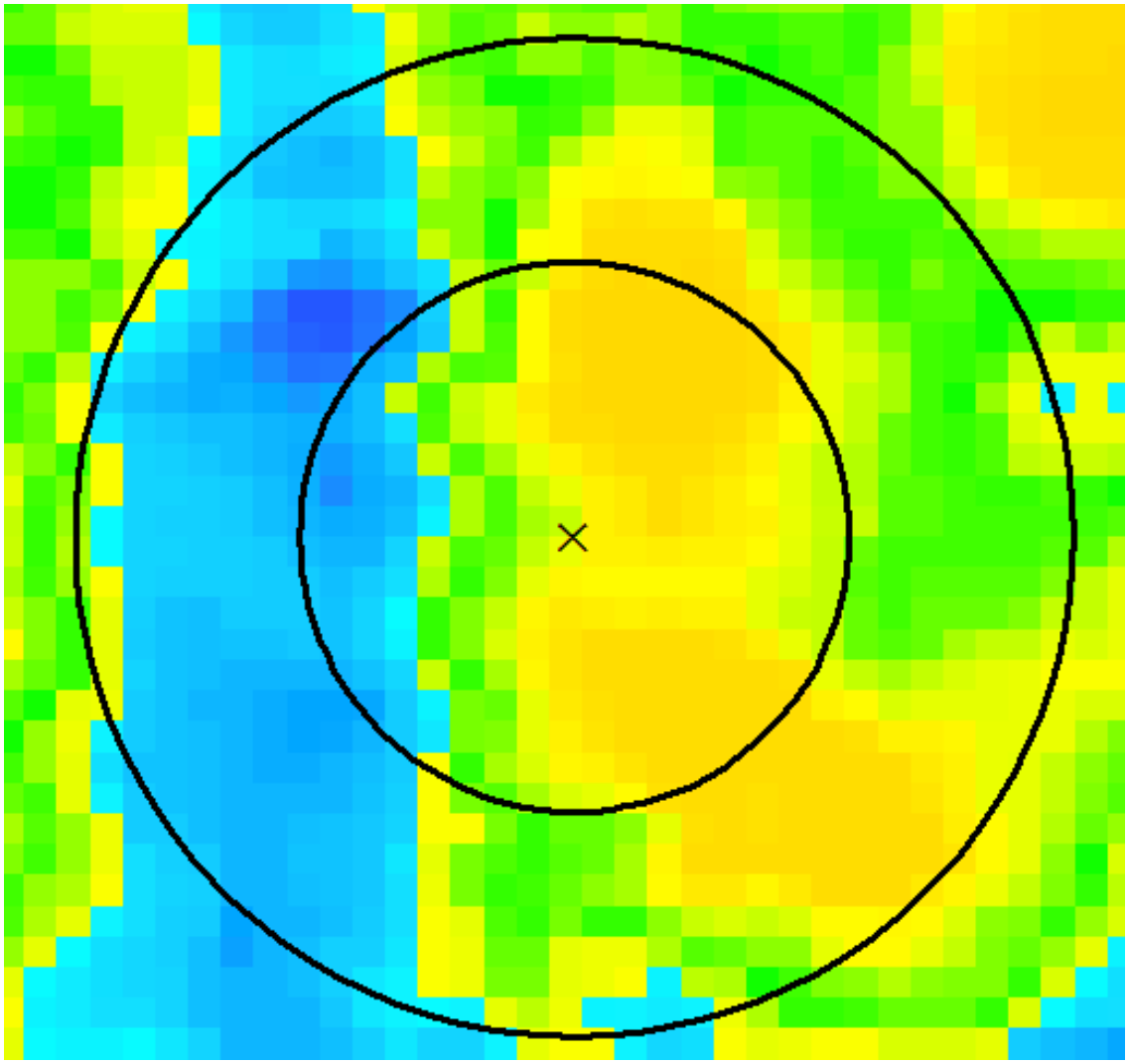

Figure 9. Sample Site XY-data point with two buffer rings (110 m, 200 m) on HH-band, showing individual pixels.

Several GIS layers obtained by Pinnacle Mapping Technologies were also employed, mainly as cartographic references. These layers included an outline of the Hopi reservation, major streams, and roads. All GIS layers were previously reprojected to UTM Zone 12 WGS-84.

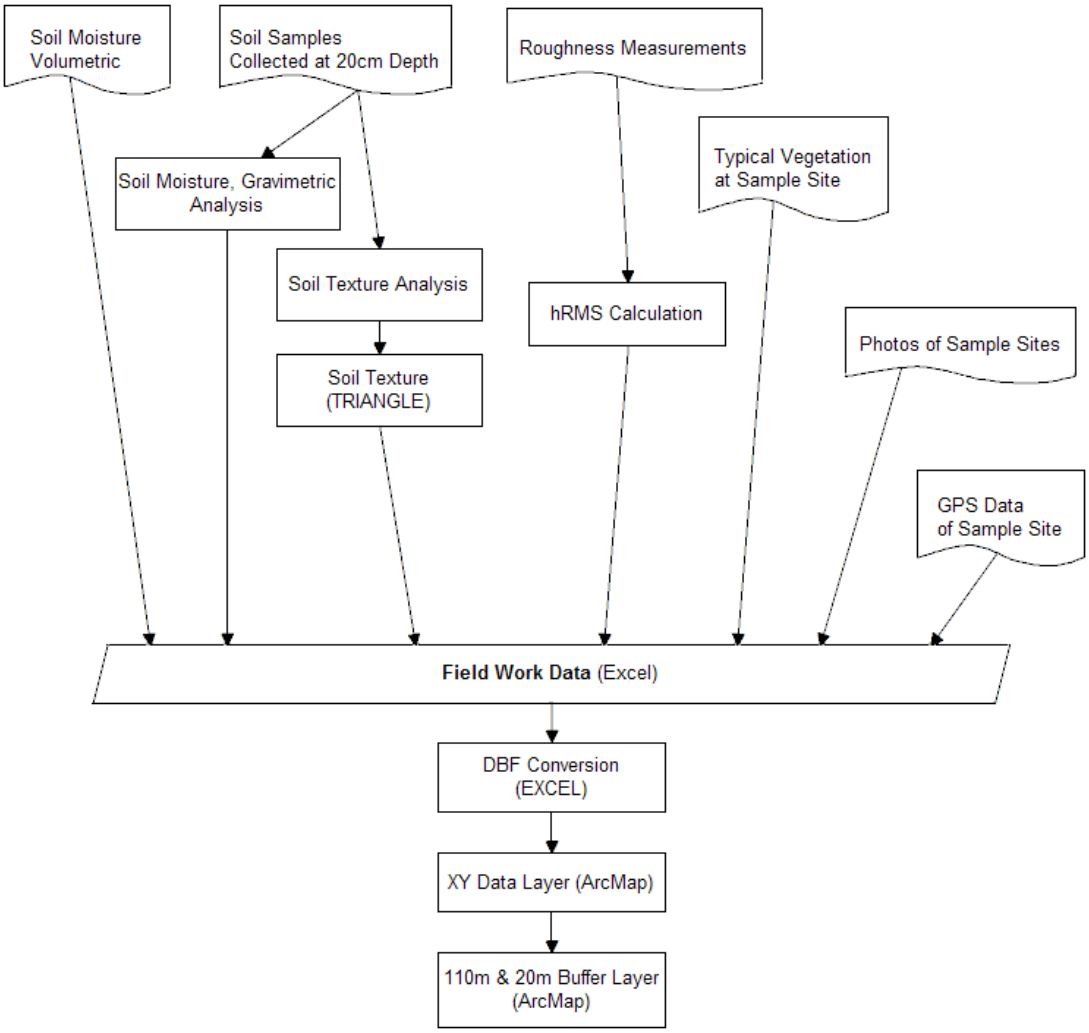

Figure 10. Flowchart Field Data Collection and Preparation.

ASAR Header Analysis

The ASAR Handbook gives a detailed description of the image header file (Appendix G) (ESA 2009). The ASAR image used for this project is a level B1 product, meaning it had already been processed by ESA (Appendix G)). Level 1 (N1) products are only one processing step above raw data (higher level products are also available from ESA). According to the ASAR handbook,

> "Level 1B products are geolocated products in which data has been converted into engineering units, auxiliary data has been separated from measurements, and selected calibrations have been applied to the data. These products are the foundation from which higher-level products are derived. Level 0 products are transformed into Level 1B products by application of algorithms and calibration data to form a baseline engineering product." (ESA 2004, Chapter 2).

The ASAR operating mode product for this research is named ASA_APG_1P, which translates to alternating polarization, ellipsoid geolocated ASAR imagery (ESA 2004). The image consists of two co-registered bands acquired simultaneously (time ordered). The first band, or Image Data Set (MDS), has cross-polarization HV (Appendix H). The second MDS has co-polarization HH (Appendix H). The incidence angle and worst-case backscatter σ_0 depend on the Image Swath (IS), which in this case is IS6. This translates to an incidence angle of 39.1 to 42.8 degrees and a worst-case σ_0 of –22.0 dB; further a swath width of 70 km and a ground position from nadir of 550 to 620 km. The projection is WGS 84 Lat Long (UTM, by resampling); the pixel size is 12.5 m by 12.5 m. The imagery has a radar frequency of 5.33 GHz (Appendix G)).

ASAR PREPROCESSING BY ESA

As mentioned in the literature review, every raw ASAR image has been preprocessed by ESA before application of any other parameters or formatting steps. The included processes were: validation of raw ASAR data; block adaptive quantization (BAQ) decoding; raw data analysis; raw data correction; replica construction and power estimation; and noise power estimation (ESA 2004: 2.6.1.2.1). For backscatter calibration of ground range detected products (of which ASA_APG-1P is one of them), the calibration formula is

$$\sigma^0_{i,j} = \frac{DN^2_{i,j}}{K} * \sin(\alpha_{i,j})$$

$$\gamma_{i,j} = \frac{\sigma^0_{i,j}}{\cos(\alpha_{i,j})}$$

for i=1…L and j=1…M,

where K is the absolute calibration constant; $DN^2_{i,j}$ is the pixel intensity value at image line and column "i,j"; $\sigma_{i,j}$ is sigma naught at image line and column "i,j"; $\alpha_{i,j}$ is the incidence angle at image line and column "i,j"; $\gamma_{i,j}$ is gamma at image line and column "i,j"; and L,M are number of image lines and columns (Rosich and Meadows 2004). Sigma naught is converted to decibel by the following formula:

$$\sigma^0[dB] = 10 * \log_{10}(\sigma^0).$$

Because ASAR images arrive already calibrated by ESA, further calibration may not be necessary. However, adding more processing steps, such as speckle filters (median or Lee), to the level 1B product after acquisition from ESA will increase the error.

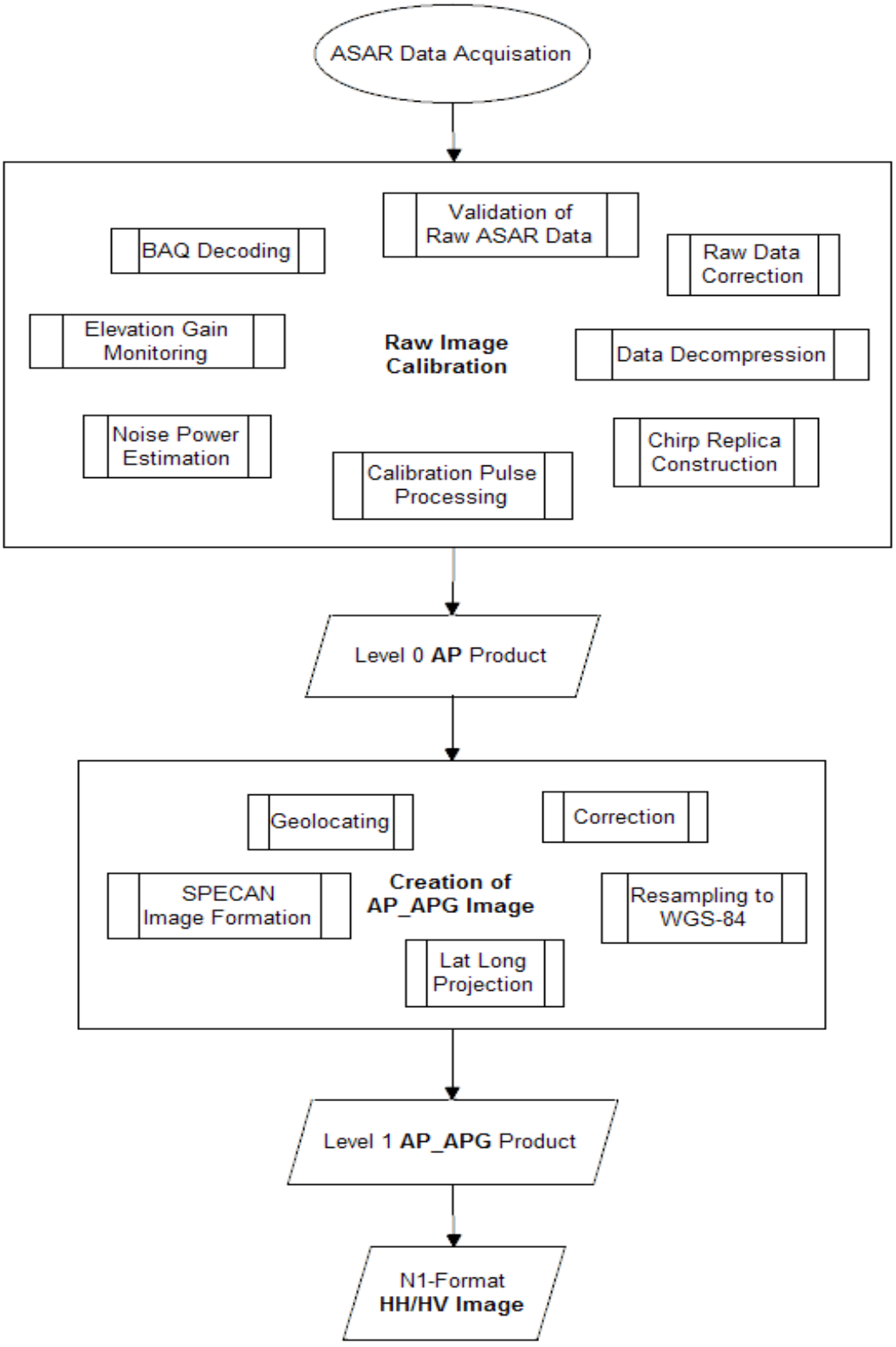

Figure 11. Flowchart ESA Pre-Processing

ASAR PROCESSING

The processing and analysis steps of this study tracked the example given by Rahman et al. (Rahman et al. 2008). The authors documented their project of employing the IEM to predict soil surface roughness parameters and soil surface moisture in a series of journal articles, using the like-polarized bands of four different ASAR APG images (Thoma et al. 2004; Rahman et al. 2007; Rahman et al. 2008). The equations developed by Rahman et al. were also utilized in this study. This was possible, because the conditions present and images employed for their research were similar to the conditions and image in this study.

The software employed for processing and image analysis of the ASAR image is called Nest ESA SAR Toolbox (NEST) and available free of charge from ESA (ESA/Array Systems Computing Inc. 2009). ESA has developed a series of software tools to aid the conversion and filtering of raw Envisat data (as in Level 1B AP data format), previously released as Basic Envisat SAR Toolbox (BEST), which lacked user friendliness and tended to crash. Perhaps due to these disadvantages, ESA developed NEST, a user-friendly application with intuitive GUI (graphical user interface), better control options, and more processing and analysis tools. The current version of NEST is Nest 3B, released in October 2009, and can be downloaded at http://www.array.ca/nest/tiki-index.php. The steps taken with NEST included header analysis, amplitude to power conversion, speckle filtering, statistical analysis, and band arithmetic.

The raw image file is in ESA N1 file format and could not be imported into any of the standard image processing software available to the author, consequently had to be

converted into a standard image file first. The ASAR May scene available for this study was imported into NEST. By importing an ASAR image, the software automatically added all image information grouped by metadata and bands to the project. Any alterations or processing steps on the image completed had to be saved in order to not accidentally lose them; NEST uses the BEAM-DIM file format for this.

The first processing step was the conversion of both amplitude bands (HH and HV) from "Linear to dB". It was necessary to convert to decibel units (dB), because the raw image's digital numbers (DN) were given in units of amplitude which were values local to this particular image and cannot be used globally. The conversion was done automatically by NEST; no further user input was needed to calculate the dB values. The converted image was then speckle filtered. The NEST speckle filter tool allows for different filtering options. A median filter with 9 by 9 pixels was used for de-speckling the image, cleaning the salt-and-pepper raw image by removing noise (Appendix I). After the speckle filtering, the band statistics and histograms were calculated and the file was saved (Appendix I). Further image enhancement was not deemed necessary, because there were no extreme data values. Also, image registration was not needed, because the two bands were co-registered, and image-to-ground registration was evened out by an increase in pixel size later on.

CHAPTER 4 –MODELING ROUGHNESS WITH THE IEM

BACKSCATTER DIFFERENCE

In NEST, the image file was saved as BEAM-DIM after de-speckling and dB conversion. Using the NEST utility tool "Band Arithmetic", a backscatter difference map $\Delta\sigma^0$ was created (Appendix J). According to Zribi and Dechambre, the backscatter difference $\Delta\sigma^0$ is a proportion of the roughness parameters h_{RMS} and L_c (Z-index), such that

$$g\left(\Delta\sigma^0\right) = \frac{h_{RMS}^2}{L_c}$$

when two different incidence angles are applied, all else being equal (Zribi and Dechambre 2003). In the case of this study, the incidence angle (range) was virtually the same for both bands, however the polarization was different. It was assumed that the function by Zribi and Dechambre was applicable for this study, as long as all else was equal. The formula entered in the Equation Calculator in NEST was

$$\Delta\sigma^0 = \sigma^0 HH - \sigma^0 HV ,$$

where $\Delta\sigma^0 HH$ is the backscatter of the HH band and $\Delta\sigma^0 HV$ the backscatter of the HV band (Appendix J).

Rahman et al. modified the above Z-index formula and set it equal to another function developed by Zribi and Dechambre (Zribi and Dechambre 2003; Rahman et al. 2008):

$$\frac{\left(0.618 + 0.09 * \Delta\sigma^0\right)}{\left(1 - 0.138 * \Delta\sigma^0\right)} = \frac{h_{RMS}^{2.5}}{L_c} .$$

The left side of this formula was used to calculate the Z-index. This was also done with the NEST "Band Arithmetic" tool. The resulting image depicted the proportion of both roughness parameters for each pixel value (Appendix J).

NUMERICAL SOLUTION FOR H_{RMS} AND CALCULATION OF L_C

Since the Z-index maps the proportion of the roughness parameters, it was plugged into a formula that Rahman et al. fitted with their data as an approximation of the IEM (Rahman et al. 2008):

$$\sigma^0_{dry} = -27.94 + 32.58h_{RMS} - 18.78h^2_{RMS} + 2.65h^3_{RMS}$$
$$+ \frac{1}{z-index} * \left(-1.40h^{2.5}_{RMS} + 0.86h^{3.5}_{RMS} + 0.12h^{4.5}_{RMS}\right)$$
$$+ \left(\frac{1}{z-index}\right)^2 * \left(0.05h^5_{RMS} - 0.04h^6_{RMS}\right)$$

This exponential formula cannot be solved other than numerically. An Excel table was created for this task, with possible h_{RMS} values on the x-axis and Z-index values (as determined from the Z-index map histogram) on the y-axis. Each possible pair of Z-index and h_{RMS} values was plugged in the exponential formula so that every cell returns a particular solution for a pair of h_{RMS} and Z-index values (Appendix K). By means of this look-up table, an h_{RMS} reclassification scheme was devised that groups common σ^0_{dry} and Z-index pairs with an h_{RMS} value. Back in NEST, the $\sigma^0_{dry} HH$ band was reclassified by a set of virtual bands of which each was assigned a particular h_{RMS} value (Figure 12). All of these virtual bands were then combined in one band by adding them with the NEST "Band Arithmetic" tool. The resulting band depicts the h_{RMS} map (Appendix L).

Dry Scene Backscatter Reclassification *Classification of hRMS*	hRMS
Amplitude_HH_dB >= 25 ?0.1:0	0.1
Amplitude_HH_dB<25 and Amplitude_HH_dB>=24?0.3:0	0.3
Amplitude_HH_dB<24 and Amplitude_HH_dB>=23?3.0:0	3.0
Amplitude_HH_dB<23 and Amplitude_HH_dB>=22?0.2:0	0.2
Amplitude_HH_dB<22 and Amplitude_HH_dB>=21 and Zindex2<0 ?2.2:0	2.2
Amplitude_HH_dB<22 and Amplitude_HH_dB>=21 and Zindex2>=0 ?3.2:0	3.2
Amplitude_HH_dB<21 and Amplitude_HH_dB>=20?0.3:0	0.3
Amplitude_HH_dB<20 and Amplitude_HH_dB>=19 and Zindex2<0 ?2.1:0	2.1
Amplitude_HH_dB<20 and Amplitude_HH_dB>=19 and Zindex2>0 ?3.1:0	3.1
Amplitude_HH_dB<19 and Amplitude_HH_dB>=18?0.4:0	0.4
Amplitude_HH_dB<18 and Amplitude_HH_dB>=17?2.1:0	2.1
Amplitude_HH_dB<17 and Amplitude_HH_dB>=16?0.5:0	0.5
Amplitude_HH_dB < 16 ?1.3:0	1.3
If Statement : Statement ? True : False	

Table 1. h_{RMS} Classification

With the h_{RMS} map available, one can now solve the Z-index equation for the roughness parameter L_c. The formula

$$z - index = \frac{h_{RMS}^{2.5}}{L_c}$$

was applied on the h_{RMS} map, again using the NEST "Band Arithmetic" tool. The resulting image illustrates the L_c values for this particular ASAR image. As a result of this study, the two roughness parameters h_{RMS} and L_c have been mapped using the IEM and a dual-polarity ASAR image (Figures 15 and 16, Appendix L).

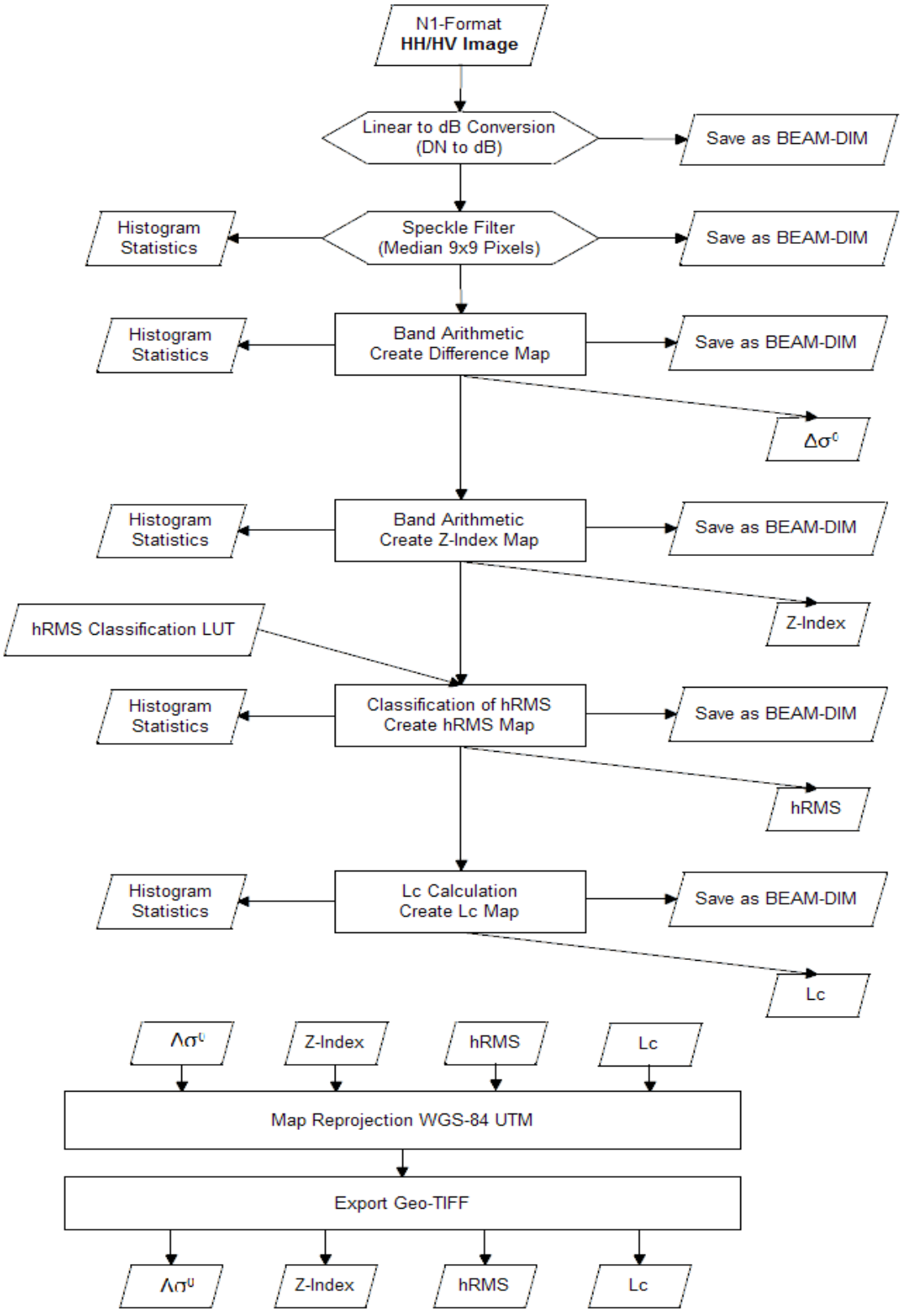

Figure 12. Flowchart NEST Processing

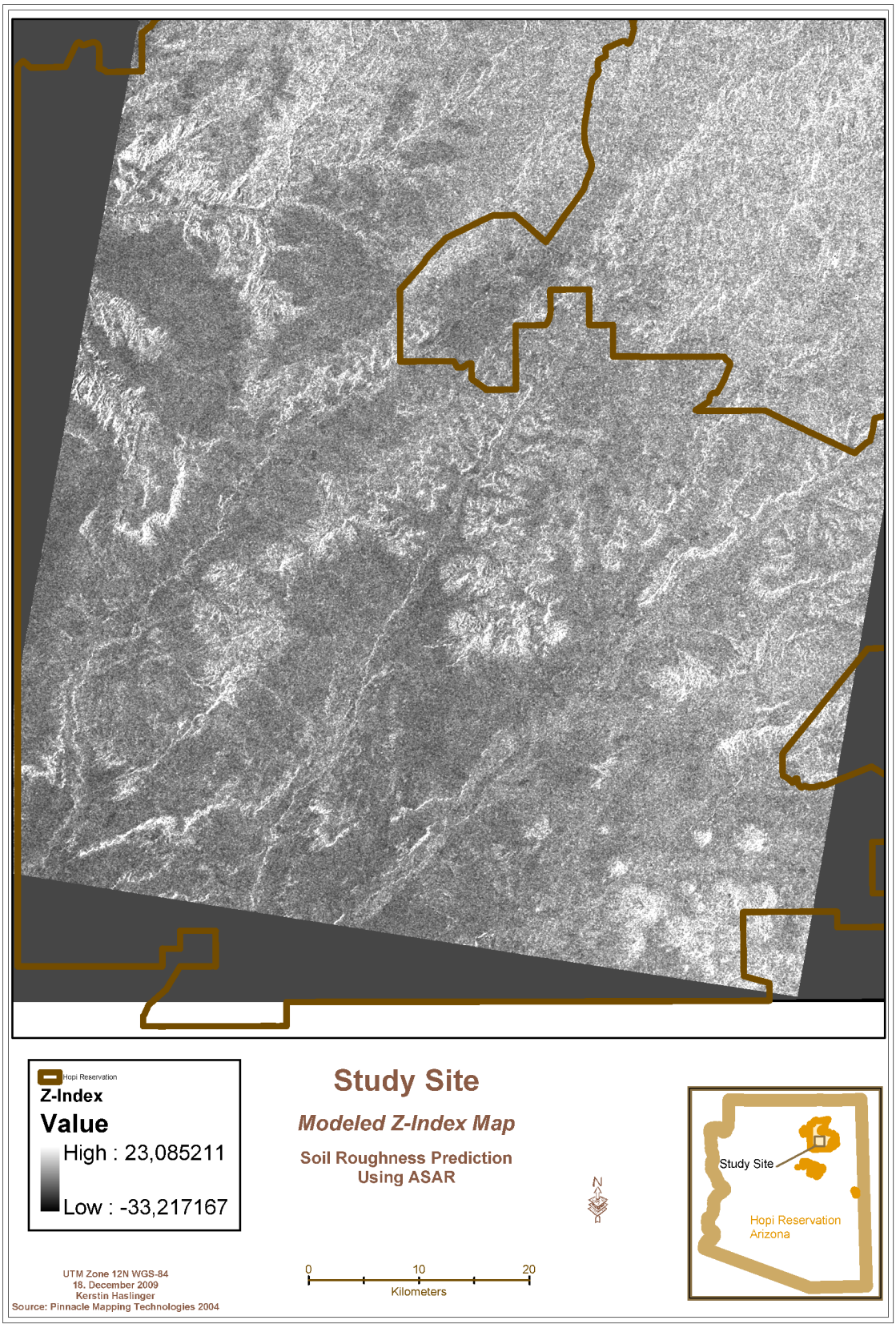

Figure 13. Modeled Z-Index map.

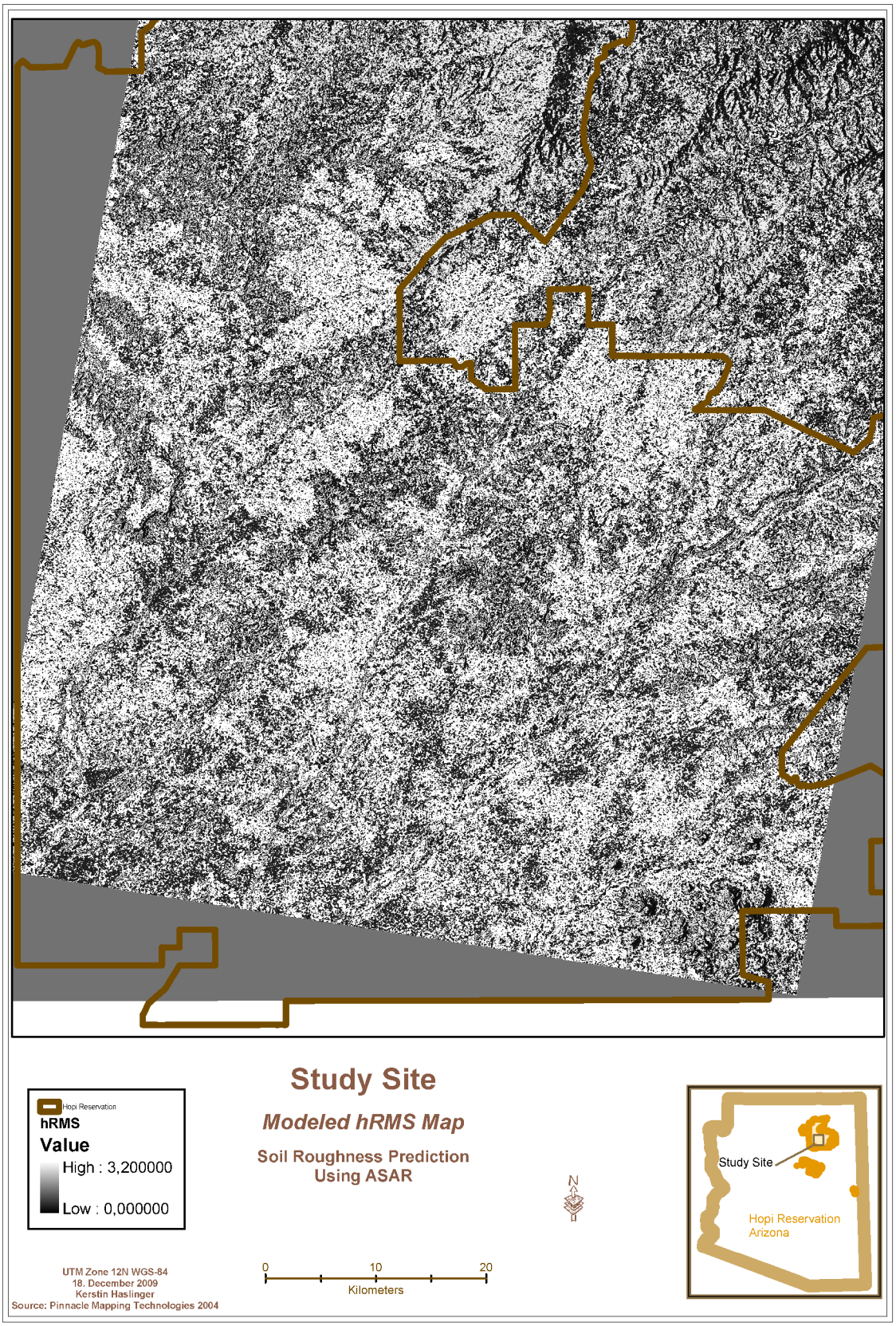

Figure 14. Modeled h_{RMS} map.

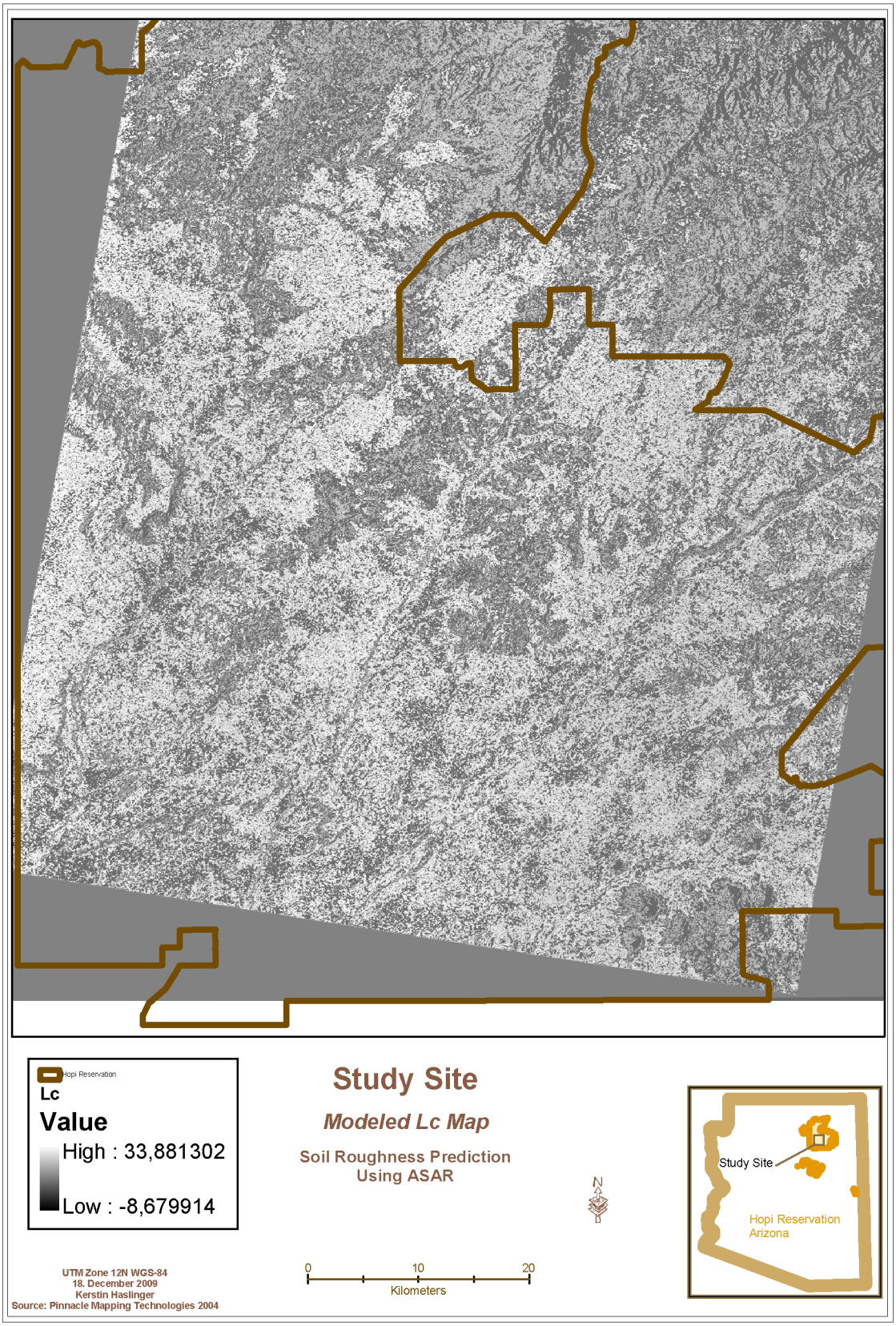

Figure 15. Modeled L_c map.

CHAPTER 5 – STATISTICAL ANALYSIS AND DISCUSSION

EXTRACTING VARIABLE VALUES

Though NEST is a very good tool for ASAR image processing and band arithmetic, it lacks statistical analysis tools. The NEST file format for ASAR images is not applicable in other image processing and GIS software packages, therefore all bands of interest have to be converted to GeoTIFF file format for further processing and analysis. Unfortunately, the NEST version of the GeoTIFF format cannot be imported into ArcGIS, so it has to be converted to IMG format using ERDAS Imagine first. All relevant bands of the de-speckled image were exported as GeoTIFF and imported in ERDAS Imagine. With the import, the bands were converted to IMG format. They were also reprojected to UTM Zone 12 WGS-84 to fit the GIS layers and XY-event layer.

The ASAR image bands h_{RMS}, L_c, HH-dB, and Z-index were imported into ArcGIS. First, the XY-data event layer of the field data points and the buffered layers were stripped of all points and buffers that were not located on the ASAR image (Appendix M). The buffer layers were then checked to verify that their ID values coincide with their corresponding points of the XY-data layer. This step had to be taken to ensure that the field data for each sample location was matched with the correct location on the ASAR image.

Using the Zonal Statistics tool in the Spatial Analyst extension, the mean value for each buffer zone was calculated on each of the four calculated ASAR bands. Thus, all pixel values within each of the two buffered zones around each sample site were statistically evaluated (Figure 9). The resulting statistical description was stored in

look-up tables (LUT) which were related to the appropriate buffer layer: the statistical mean and standard deviation for each point in the 110 m buffer zones were stored in a LUT and related to the 110 m buffer layer; the statistical mean and standard deviation for each point in the 200 m buffer zones are stored in another LUT which is related to the 200 m buffer layer. A set of Vonoroi plots depicted a Thiessen Polygon comparison of the h_{RMS} values of the field data and the two buffered mean values for each sample point (Appendix N). The statistical information was then transcribed to the XY-data layer of the field data points. The XY-data event layer was then saved as a shapefile (SHP) that stores the XY-data in a DBF format table.

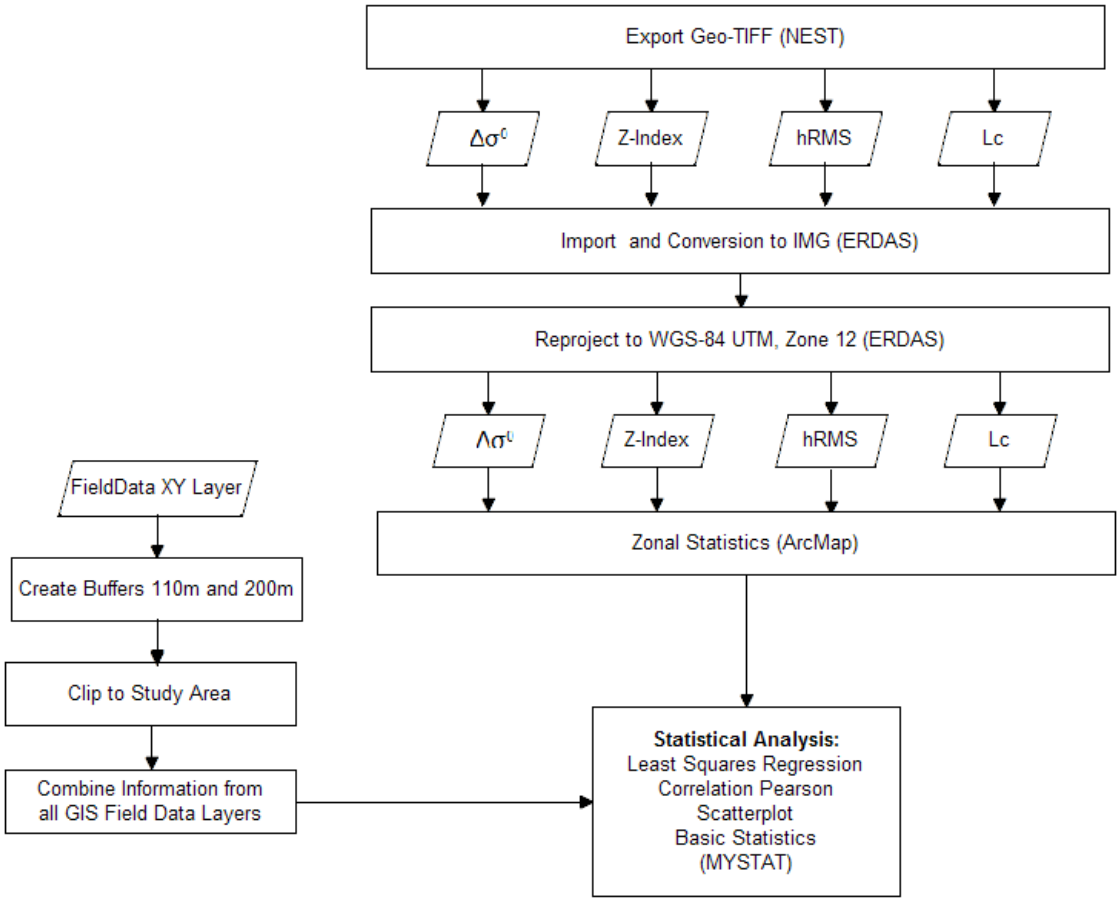

Figure 16. Flowchart Data Preparation for Statistical Analysis

STATISTICAL ANALYSIS

The DBF format can be opened by Excel, where the tables are rearranged and then transcribed into MYSTAT, the free-of-charge student version of the statistical software SYSTAT. In MYSTAT, the table was prepared for the statistical analysis: the table itself had to be variable values only, so the column headers were cut and pasted to the appropriate table variable name boxes; some variables were imported in string format and had to be changed to number format. The statistical analysis consisted of three parts, namely descriptive statistics, correlation and regression (Figures 18, 19 and 20, respectively). It focused mainly on the relationships between the in-field value of h_{RMS} and the modeled mean values of Z-index and h_{RMS} within the buffered areas. There were 43 valid cases of in-field h_{RMS} mean values, therefore the statistical analysis was reduced to those modeled sites which corresponded with these in-field values (Figure 18). Compared to the mean in-field h_{RMS}, the arithmetic mean decreased slightly in the modeling of the Z-index, but almost doubled in the modeled h_{RMS}.

	HRMS_IN_FIELD	ZI1	ZI2	HRMS1	HRMS2
N of Cases	43	52	52	52	52
Minimum	0.450	0.807	0.823	0.548	0.863
Maximum	2.850	1.499	1.373	3.135	2.859
Arithmetic Mean	1.398	1.073	1.072	2.018	2.019
99.0% Lower Confidence Limit	1.163	1.015	1.022	1.749	1.804
99.0% Upper Confidence Limit	1.633	1.132	1.121	2.287	2.235
Standard Deviation	0.571	0.156	0.134	0.726	0.581
Variance	0.326	0.024	0.018	0.527	0.337

Table 2. Descriptive Statistics of in-field h_{RMS} in combination with the buffered means of Z-index and h_{RMS} (where 1 = mean of buffer 110 m, 2 = mean of buffer 200 m).

The correlation analysis featured the four pairings of the in-field h_{RMS} and the buffered counterparts from the Z-index and h_{RMS} bands (Figure 19). Of these pairings, the combinations in-field h_{RMS} and modeled Z-index had a Pearson's R of 0.240 for the

110m buffer and 0.298 for the 200m buffer, while the corresponding modeled h_{RMS} mean values of these buffered areas had a Pearson's R of 0.118 and 0.174, respectively. The elliptical shape of the correlation plots illustrated a weak correlation between in-field h_{RMS} and Z-index values and an almost non-existent correlation between the in-field h_{RMS} and the modeled counterparts. It was not surprising that the combination of $h_{RMS}1$ (110 m buffer) and $h_{RMS}2$ (200 m buffer) revealed a large correlation (0.889); after all, the entire 110 m buffer zone was included in the 200 m buffer. The correlation between Z-index1 (110m buffer) and Z-index2 (200m buffer) is even stronger (0.928).

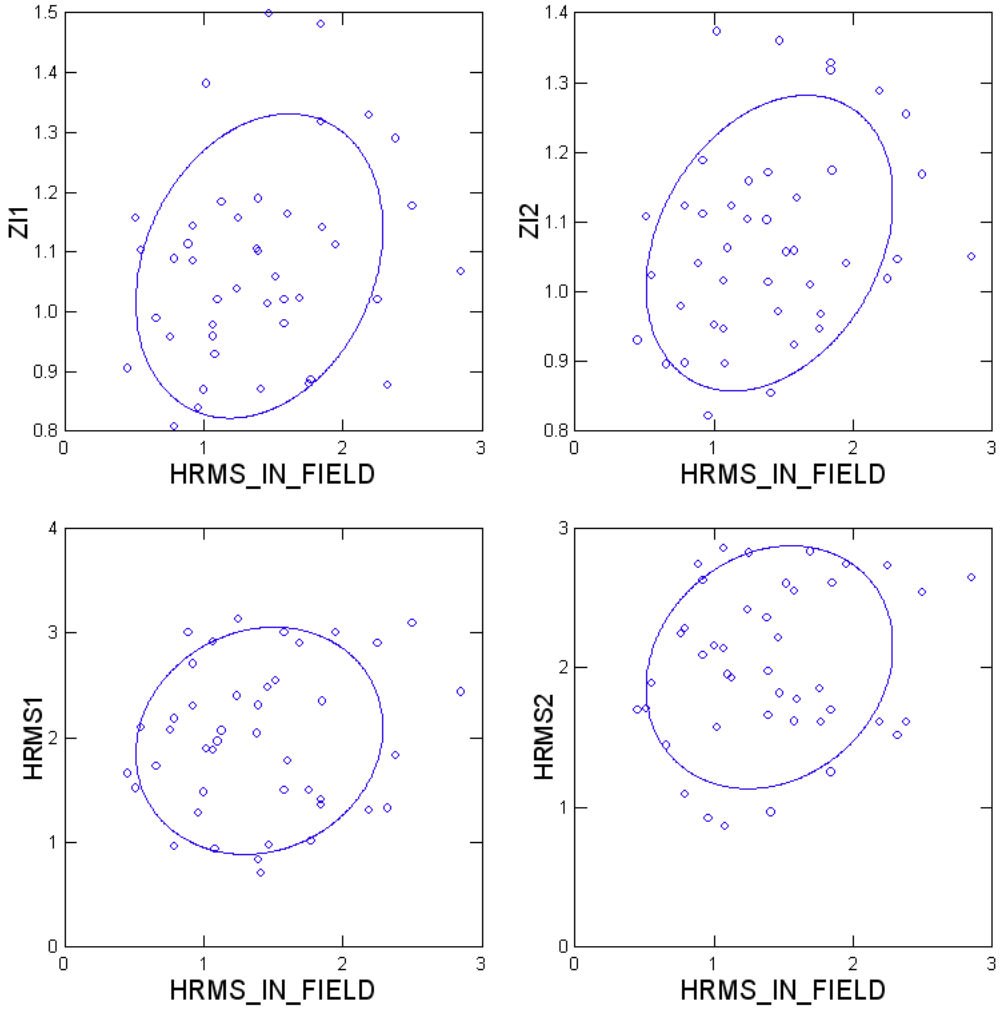

Figure 17. Pearson Correlation Matrix of h_{RMS} in combination with the buffered means of Z-index and h_{RMS} (where 1 = mean of buffer 110 m, 2 = mean of buffer 200 m).

Pearson Correlation Matrix

	HRMS_IN_FIELD	ZI1	ZI2	HRMS1	HRMS2
HRMS_IN_FIELD	1.000				
ZI1	0.240	1.000			
ZI2	0.298	0.928	1.000		
HRMS1	0.118	0.072	0.065	1.000	
HRMS2	0.174	0.081	0.133	0.889	1.000

Table 3. Pearson Correlation Matrix of h_{RMS} in combination with the buffered means of Z-index and h_{RMS} (where 1 = mean of buffer 110 m, 2 = mean of buffer 200 m).

The regression analysis paired in-field h_{RMS} with the modeled Z-index and h_{RMS} values, as well as the two modeled h_{RMS} values with each other and with the backscatter band σ^0_{dry} in least squares regression, all at a confidence interval of 0.99%. For the combinations of in-field h_{RMS} with modeled $h_{RMS}1$ (110 m buffer) and $h_{RMS}2$ (200 m buffer), the values of regression coefficient R indicated moderate relation of R = 0.118 at a P-value of 0.452 and R = 0.174 at a P-value of 0.263, respectively (Figure 20). The pairings of in-field h_{RMS} with Z-index1 (110m buffer) and Z-index2 (200m buffer) resulted in a regression coefficient of R = 0.240 at a P-value of 0.120 and 0.298 at a P-value of 0.052, respectively (Figure 20). The least squares regression of the two buffered h_{RMS} values against each other yielded a near perfect regression correlation of R = 0.889 with a mean squared error of 0.067 and a P-value of $1.68*10^{-15}$.

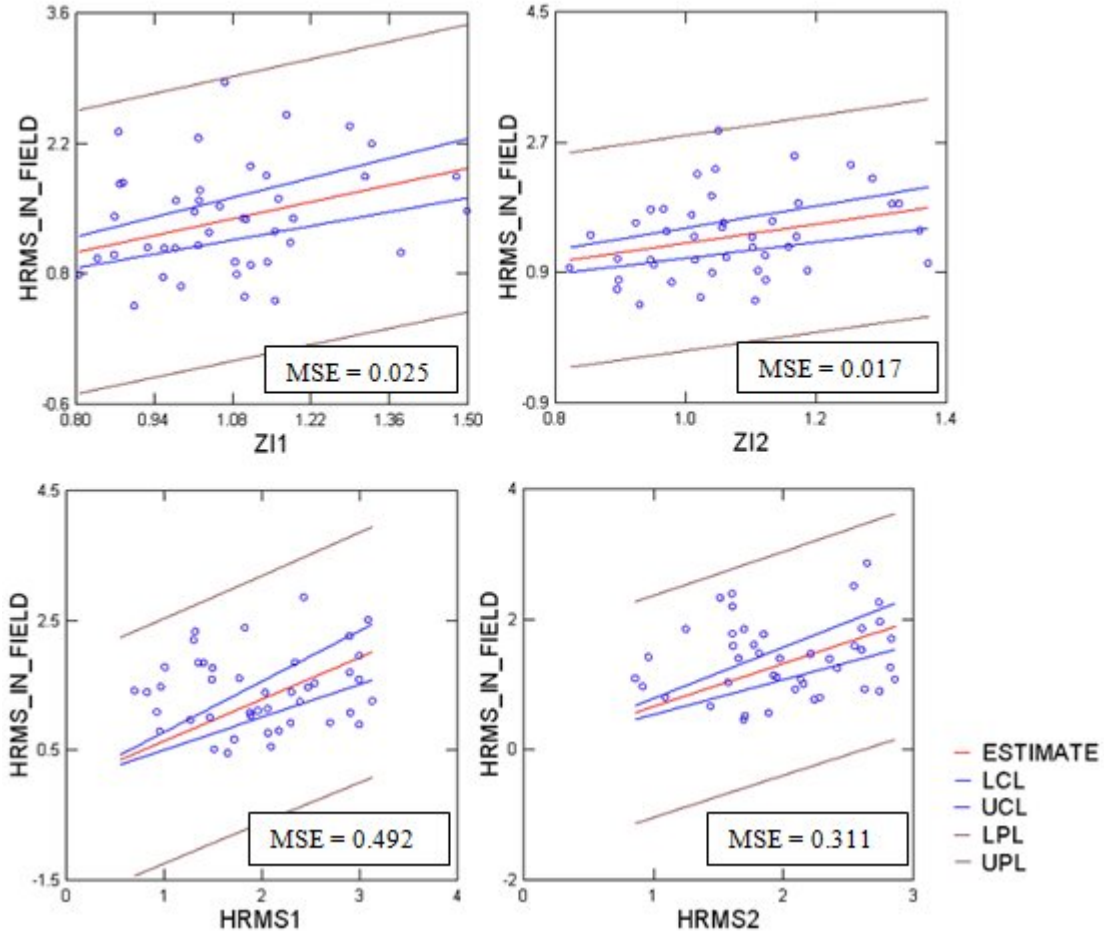

Figure 18. Least Squares Regression Plots of in-field h_{RMS} in combination with the buffered means of Z-index and h_{RMS} (where 1 = mean of buffer 110 m, 2 = mean of buffer 200 m).

Neither the in-field h_{RMS} nor the modeled values of h_{RMS} and Z-index showed any relation with the σ^0_{dry} band (Figure 21). The mean values of L_c were not included in the statistical analysis, because L_c is proportional to h_{RMS} as defined by the Z-index.

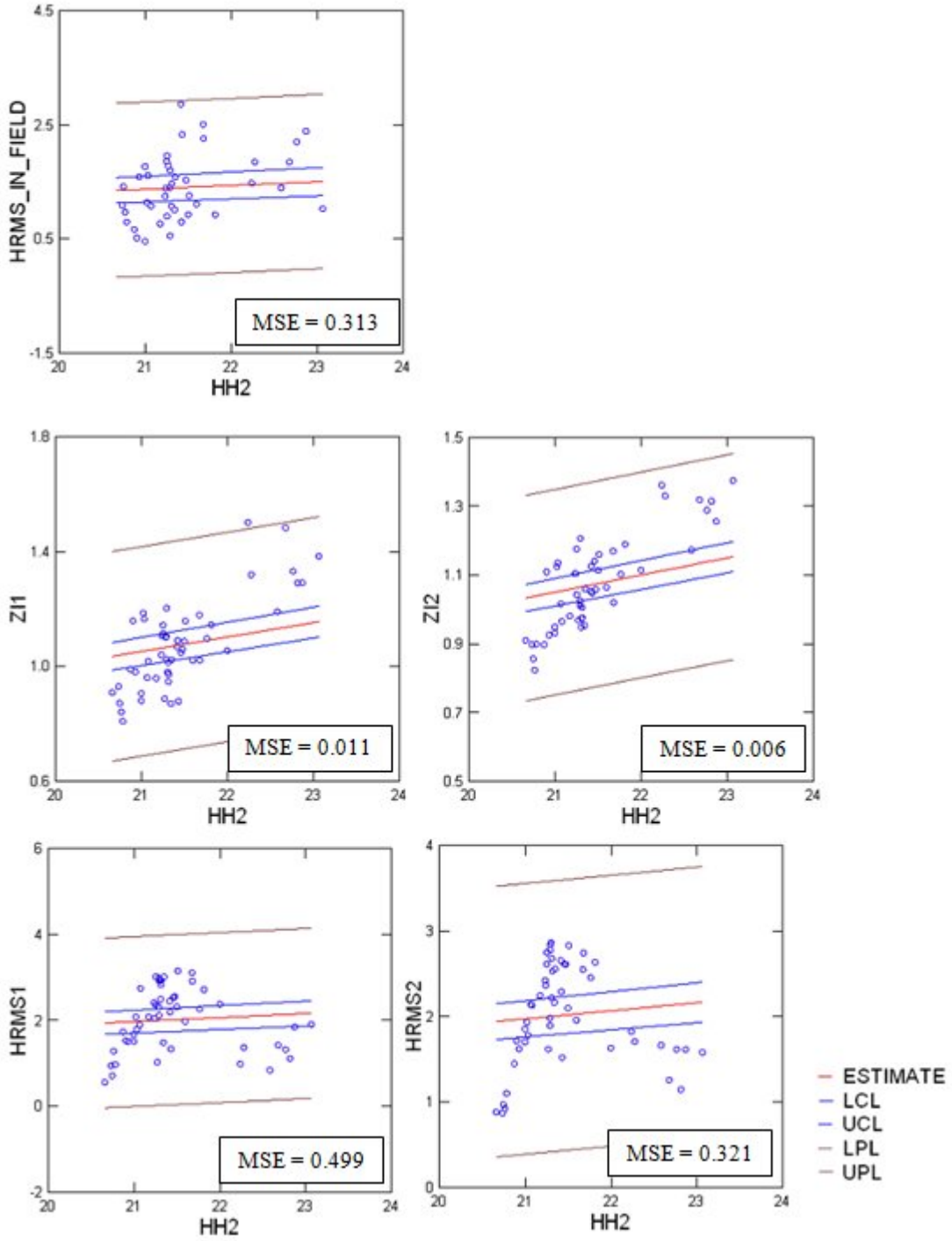

Figure 19. Least Squares Regression Plots of Z-index and h_{RMS} in combination with the buffered mean of $\sigma^0_{dry,HH}$ (where 1 = mean of buffer 110 m, 2 = mean of buffer 200 m).

DISCUSSION

The mapping of distributed soil surface roughness used to be a tedious undertaking. It encompassed several days of fieldwork that only yielded data restricted to the sampled points. Furthermore, the data were only valid for the point in time of their collection, hence the data could not be utilized to cover a larger area or time range. These shortcomings have been partially remedied by use of remote sensing tools, such as thermal imagery. During the last decade, radar technology has been employed to enhance the modeling and mapping of soil surface properties. Especially C-band radar imagery seemed to be a perfect candidate for modeling soil surface properties because of its short penetration rate. The Integral Equation Model (IEM) has been constructed as a tool to predict soil surface properties by use of radar imagery, however it needed several in-field variables to work properly. Recently, a method was developed which maps the soil surface roughness parameters solely with radar images instead of in-field parameters. That study by Rahman et al. focused on multi-angled radar data (Rahman et al. 2008), which added error to the process due to the incidence angle estimations and the time lag between the capture of the images.

The use of an ASAR dual polarity image in this study removed the problematic time lag, as well as the incidence angle discrepancy, because both like- and cross-polarized bands were taken with the same sensor at the same time, using the same incidence angle. The dual polarity image used for this study was taken during dry conditions, which reduced the number of unknown IEM variables to just the roughness variables h_{RMS} and L_c. The Z-index illustrates the relationship between these two variables. Both roughness variables h_{RMS} and L_c were modeled with IEM. First, a

difference map of the two polarized bands was calculated and employed to retrieve the Z-index. With the help of an Excel table the possible values of h_{RMS} for each Z-index value was calculated, which in turn were used to prescribe a h_{RMS} classification look-up table. The resulting h_{RMS} map was then utilized to find the corresponding L_c values.

The statistical analysis showed a relationship between the in-field and the modeled mean values of the roughness parameter h_{RMS}, though the correlation is weak. There seemed to be a trend whereby the modeled values of this research were distorted which can be detected by comparison of the arithmetic mean. The arithmetic mean of the in-field h_{RMS} was calculated at 1.398 cm, while it was nearly twice as high for the modeled values (2.018 cm for the 110 m buffer and 2.019 cm for the 200 m buffer). Contrary to the modeled h_{RMS} statistical values in correlation and regression, the Z-index performed at a much better rate (Figures 16 and 17). The decrease in Pearson's R values and regression coefficients between the Z-index map and the modeled h_{RMS} map most likely can be attributed to the classification scheme which determined h_{RMS}. The numerical solution was calculated using a coarse sequence of Z-index / h_{RMS} pairings; a finer interval may have yielded a different classification scheme and therefore could have resulted in a more accurate h_{RMS} map. An increase in classes could also have resulted in a better fitting correlation of in-field and modeled mean values. In addition, the IEM equations applied in this study were derived for a similar study by Rahman et al. that utilized like-polarized $\sigma^0_{dry,VV}$ radar images with multi-angle images on a comparable study site (Rahman et al. 2008, 393). An adjustment in these equations may have been helpful, though the outcome of this study resembled that of the study by Rahman et al..

The same decrease in relation was also seen in the regression analysis of Z-index map and h_{RMS} map paired with σ^0_{dry}. It became evident that by employing the IEM, that is calibrating h_{RMS} by use of the polynomial equation, the results were distorted. However, this did not necessarily mean that the calculation was wrong, as the in-field h_{RMS} values performed almost at the same rate as the modeled h_{RMS} map.

Another observation of the statistical analysis was that there was only a slight increase in correlation between the 110 m buffered values and the 200 m buffered values. In their study, Rahman et al. had to increase the scale of the buffered area to 150 m by 150 m because of unfavorable sub-surface phenomena (Rahman et al. 2008, 394). In hindsight, the increased buffer size (from 110 m to 200 m) did not seem to be necessary in my study, mainly because of the homogeneity of the soil-surface and sub-surface, though a larger buffer size generally results in a better fit.

This research compared similarly to the study by Rahman et al. in 2008. The image-derived h_{RMS} and L_c values behaved in the same way in both studies. Though Rahman et al. attributed most of their error to sub-surface rock fragments, these were not present at the Hopi Reservation sample sites. It could be that the model itself is in need of an adjustment. For example, the error could have been due to the size of the speckle filter, as Rahman et al. reasoned in their study. However, concluding their study with the modeling of soil surface moisture θ_0, the prediction of the study by Rahman et al. met the in-field measurements with minimal error. This outcome was validated by a study by Thoma et al. (Thoma et al. 2006) which compared different methods of retrieving soil surface roughness and consequently soil surface moisture θ_0.

It can be said that the method of modeling soil surface roughness applied herein is valid on similar surfaces (semi-arid rangeland) with a resolution slightly lower than that of the ASAR image. This method can be helpful in determining soil surface properties for various applications without the use of ancillary data. As Rahman et al. did in their study (Rahman et al. 2008), once the soil surface roughness variables h_{RMS} and L_c have been calculated and adjusted, the IEM can be utilize to calculate of the soil surface moisture θ_0. It is then possible to model soil surface roughness and soil surface moisture θ_0 for entire regions exclusively without or with minimal fieldwork. This could be of benefit to regional planning as much as agriculture. It could assist by selection of rangelands suitable for agriculture, or determination of the state of the soil before planting or shortly thereafter. It could also be employed to detect overgrazing of rangelands.

Further research could explore the modeling of soil surface roughness and subsequently the modeling of soil surface moisture with dual-polarization ASAR imagery by means of adjusted IEM equations and a revised h_{RMS} reclassification. The IEM derived equations applied in this study were taken from a similar study. Though the study sites were similar, an adjustment in the equations may foster more accurate results. Fine tuning the h_{RMS} classification could be done several ways. For one, in the numerical solution for $\sigma^0_{dry,HH}$ that was used to define the h_{RMS} classification, $\sigma^0_{dry,HH}$ was calculated by means of a coarse interval of possible values of h_{RMS} and the Z-index. A more refined interval may result in a different pattern and therefore a refined h_{RMS} classification. Also, the h_{RMS} classification's range of classes could be expanded which may improve the results as well.

BIBLIOGRAPHY

Acocella, V., and R. Funiciello. 1999. The interaction between regional and local tectonics during resurgent doming: the case of the island of Ischia, Italy. *Journal of Volcanology and Geothermal Research* 88:109-123.

Altese, E., O. Bolognani, M. Mancini, and P. Troch. 1996. Retrieving soil moisture over bare soil from ERS 1 synthetic aperture radar data: sensitivity analysis based on a theoretical surface scattering model and field data. *Water Resources Research* 32:653-661.

Avery, T. E., and G. L. Berlin. 1992. *Fundamentals of remote sensing and airphoto interpretation.* New York: Macmillan Publishing Company.

Baghdadi, N., I. Gherboudj, M. Zribi, M. Sahebi, C. King, and F. Bonn. 2004. Semi-empirical calibration of the IEM backscattering model using radar images and moisture and roughness field measurements. *International Journal of Remote Sensing* 25:3593-3623.

Baghdadi, N., N. Holah, and M. Zribi. 2006. Calibration of the Integral Equation Model for SAR data in C-band and HH and VV polarizations. *International Journal of Remote Sensing* 27:805-816.

Baghdadi, N., and M. Zribi. 2006. Evaluation of radar backscatter models IEM, OH and Dubois using experimental observations. *International Journal of Remote Sensing* 27:3831-3852.

Barstow R. 2004. ASAR Product Format Specifications.

Benallegue, M., O. Taconet, D. Vidal-Madjar, and M. Normand. 1995. The use of radar backscattering signals for measuring soil moisture and surface roughness*1. *Remote Sensing of Environment* 53:61-68.

Bindlish, R., and A. P. Barros. 2001. Parameterization of vegetation backscatter in radar-based, soil moisture estimation. *Remote Sensing of Environment* 76:130-137.

———2000. Multifrequency Soil Moisture Inversion from SAR Measurements with the Use of IEM. *Remote Sensing of Environment* 71:67-88.

Bindlish, R., T. J. Jackson, A. J. Gasiewski, B. Stankov, M. Klein, M. H. Cosh, I. Mladenova, C. V. Watts, V. Lakshmi, J. Bolten, and T. Keefer. 2008. Aircraft based soil moisture retrievals under mixed vegetation and topographic conditions. *Remote Sensing of Environment* 112:375-390.

Birkeland, P. W. 1999. *Soils and geomorphology.* New York: Oxford University Press.

Boll, J., van Rijn, R. P. G., K. W. Weiler, J. A. Ewen, J. Daliparthy, S. J. Herbert, and T. S. Steenhuis. 1996. Using ground-penetrating radar to detect layers in a sandy field soil. *Geoderma* 70:117-132.

Butler, K. Soil Texture and particle size determination background information. 2004 Available from http://cropsoil.psu.edu/Courses/SOILS101/Labs/texture.html#Study (last accessed September 2004).

Chehbouni, A., Y. Nouvellon, Y. H. Kerr, M. S. Moran, C. Watts, L. Prevot, D. C. Goodrich, and S. Rambal. 2001. Directional effect on radiative surface temperature measurements over a semiarid grassland site. *Remote Sensing of Environment* 76:360-372.

Chen, K. S., S. K. Yen, and W. P. Huang. 1995. A simple model for retrieving bare soil moisture from radar-scattering coefficients. *Remote Sensing of Environment* 54:121-126.

Cheng, Y., S. L. Ustin, D. Riano, and V. C. Vanderbilt. 2008. Water content estimation from hyperspectral images and MODIS indexes in Souteastern Arizona. *Remote Sensing of Environment* 112:363-374.

Cosh, M. H., T. J. Jackson, M. S. Moran, and R. Bindlish. 2008. Temporal persistence and stability of surface soil moisture in a semi-arid watershed. *Remote Sensing of Environment* 112:304-313.

Cox, N. J. 1983. On the estimation of spatial autocorrelation in Geomorphology. *Earth Surface Processes and Landforms* 8:89-93.

Cumming, I. G. /.,Frank H. 2005. *Digital processing of synthetic aperture radar data.* Norwood, MA: Artech House, Inc.

Das, N. N., B. P. Mohanty, M. H. Cosh, and T. J. Jackson. 2008. Modeling and assimilation of root zone soil moisture using remotes sensing observations in Walnut Gulch Watershed during SMEX04. *Remote Sensing of Environment* 112:415-429.

Desnos, Y. -., C. Buck, J. Guijarro, J. -. Suchail, R. Torres, and E. Attema. 2000. ASAR - Envisat's Advanced Synthetic Aperture Radar. *ESA Bulletin* 102:10.

Dobson, C. M., F. T. Ulaby, and L. E. Pierce. 1995. Land-cover classification and estimation of terrain attributes using synthetic aperture radar*1. *Remote Sensing of Environment* 51:199-214.

Durney, C. H. /.,Douglas A. 2000. *Basic introduction to bioelectromagnetics.* Boca Raton, Fla. ; London : CRC Press.

Engen, G., and H. Johnson. 1999. *A new method for calibration of SAR images.* ESA, .

Engman, E. T., and N. Chauhan. 1995. Status of microwave soil moisture measurements with remote sensing. *Remote Sensing of Environment* 51:189-198.

Engman, E. T., and J. R. Wang. 1987. Evaluating roughness models of radar backscatter. *IEEE Transactions on Geoscience and Remote Sensing* GE-25:709-713.

ESA. ASAR Handbook. 2009 Available from http://envisat.esa.int/dataproducts/asar/CNTR.htm (last accessed December 2009).

———Envisat. 2005 Available from http://envisat.esa.int/ (last accessed October 2005).

———ASAR Handbook. 2004 Available from http://envisat.esa.int/dataproducts/asar/CNTR.htm (last accessed October 2005).

———ENVISAT: ASAR Science and Applications. In ESA Publications Division [database online]. 1998 Available from http://envisat.esa.int (last accessed October 2005).

ESA/Array Systems, C. I. NEST - Next ESA SAR Toolbox. 2009 Available from http://www.array.ca/nest/tiki-index.php (last accessed October 2009).

Francek, M., and D. Valek. Soil Sieve Analysis. 2004 Available from http://www.cst.cmich.edu/users/Franc1M/esc334/exercises/soil_sieve_analysis.htm (last accessed September 2004).

Fung, A. K., Z. Li, and K. S. Chen. 1992. Backscattering from a randomly rough dielectric surface. *IEEE Transactions on Geoscience and Remote Sensing* 30:356-369.

Garrigues, S., D. Allard, and F. Baret. 2008. Modeling temporal changes in surface spatial heterogeneity over an agricultural site. *Remote Sensing of Environment* 112:588-602.

Gebremichael, M., and E. R. Vivoni. 2008. Spatial sampling uncertainty in SMEX04 soil moisture fields: a data-based resampling experiment. *Remote Sensing of Environment* 112:326-336.

Gerakis, A., and B. Baer. A computer program for soil texture classification. 1999 Available from http://soil.scijournals.org/cgi/content/full/63/4/807 (last accessed September 2004).

———TRIANGLE - a program for soil textural classification. 1999 Available from http://nowlin.css.msu.edu/software/triangle_form.html (last accessed October 2004).

Glenn, N. F., and J. R. Carr. 2004. The effects of soil moisture on synthetic aperture radar delineation of geomorphic surfaces in the Great Basin, Nevada, USA. *Journal of Arid Environments* 56:643-657.

Glenn, N. F., and J. R. Carr. 2003. The use of geostatistics in relating soil moisture to RADARSAT-1 SAR data obtained over the Great Basin, Nevada, USA. *Computers & Geosciences* 29:577-586.

Goyal, S. K., M. S. Seyfried, and P. E. O'Neill. 1999. Correction of Surface Roughness and Topographic Effects on Airborne SAR in Mountainous Rangeland Areas. *Remote Sensing of Environment* 67:124-136.

Hammon, I. W., G. A. McMechan, and X. Zeng. 2000. Forensic GPR: finite-difference simulations of responses from buried human remains. *Journal of Applied Geophysics* 45:171-186.

Hanks, R. J. 1980. *Applied soil physics : soil water and temperature applications.* Berlin ; New York : Springer-Verlag.

Heathman, G. C., P. J. Starks, L. R. Ahuja, and T. J. Jackson. 2003. Assimilation of surface soil moisture to estimate profile soil water content. *Journal of Hydrology* 279:1-17.

Heidmann, L. J. 1990. *Comparison of moisture retention curves for representative basaltic and sedimentary soils in Arizona prepared by two methods.* Fort Collins, Colo. : USDA Forest Service, Rocky Mountain Forest and Range Experiment Station.

Henderson, F. M. e., and A. J. e. Lewis. 1998. *Manual of remote sensing: Principles & applications of imaging radar.* New York, NY: John Wiley & Sons, Inc.

Hill, M. J., G. E. Donald, and P. J. Vickery. 1999. Relating Radar Backscatter to Biophysical Properties of Temperate Perennial Grassland. *Remote Sensing of Environment* 67:15-31.

Hollmann, M. Radar World. 2001 Available from http://www.radarworld.org (last accessed August 2004).

Horn, R. The DLR Airborne SAR Project E-SAR. 1997 Available from http://www.op.dlr.de/ne-hf/projects/ESAR/igars96_scheiber.html (last accessed October 2004).

Huisman, J. A., J. J. J. C. Snepvangers, W. Bouten, and G. B. M. Heuvelink. 2002. Mapping spatial variation in surface soil water content: comparison of ground-penetrating radar and time domain reflectometry. *Journal of Hydrology* 269:194-207.

Huisman, J. A., C. Sperl, W. Bouten, and J. M. Verstraten. 2001. Soil water content measurements at different scales: accuracy of time domain reflectometry and ground-penetrating radar. *Journal of Hydrology* 245:48-58.

Integrated Publishing. Sieve Analysis, Dry. Available from http://www.tpub.com/content/engineering/14069/css/14069_536.htm (last accessed September 2004).

Jackson, T. J., and M. S. Moran. 2008. Introduction to soil moisture experiments 2004 (SMEX04) Special Issue. *Remote Sensing of Environment* 112:301-303.

Jarlan, L., P. Mazzega, E. Mougin, F. Lavenu, G. Marty, P. L. Frison, and P. Hiernaux. 2003. Mapping of Sahelian vegetation parameters from ERS scatterometer data with an evolution strategies algorithm. *Remote Sensing of Environment* 87:72-84.

Johnson, A. I. 1962. *Methods of measuring soil moisture in the field.* Reston, Va.? : Denver, CO : U.S. Dept. of the Interior, U.S. Geological Survey ; For sale by the Books and Open-File Reports Section.

Kasischke, E. S., J. M. Melack, and M. Craig Dobson. 1997. The use of imaging radars for ecological applications--A review. *Remote Sensing of Environment* 59:141-156.

Kasischke, E. S., K. B. Smith, L. Bourgeau-Chavez, E. A. Romanowicz, S. Brunzell, and C. J. Richardson. 2003. Effects of seasonal hydrologic patterns in south Florida wetlands on radar backscatter measured from ERS-2 SAR imagery. *Remote Sensing of Environment* 88:423-441.

Kim, Y., and J. van Zyl. 2004. *Vegetation Effects on soil moisture estimation.* New Jersey: IEEE, pp. II: 800-802.

Kustas, W. P., E. M. Perry, P. C. Doraiswamy, and M. S. Moran. 1994. Using satellite remote sensing to extrapolate evapotranspiration estimates in time and space over a semiarid Rangeland basin. *Remote Sensing of Environment* 49:275-286.

Langley, K., S. Hamran, J. Hagen, K. Melvold, A. Baumberger, K. Hogda, R. Storvold, J. Kohler, and O. Brandt. 2004. Preliminary Results Using C-band Ground Penetrating Radar to Determine Backscatter Sources Within Glaciers. *American Geophysical Union, Fall Meeting 2004, abstract #C43A-0219*.

Laur, H., P. Bally, P. Meadows, J. Sanchez, B. Schaettler, E. Lopinto, and D. Esteban. 2004. Derivation of backscattering coefficient sigma naught in ESA ERS SAR PRI products. *ERS SAR Calibration*.

Lesurf, J. Dielectric Constant. 2002 Available from http://www.st-andrews.ac.uk/~www_pa/Scots_Guide/info/comp/passive/capacit/dielec/di_const/dicon.html (last accessed August 2004).

Levrini, G., and M. Zink. The ASAR User Guide, Issue 1.2e. 2004 Available from http://envisat.esa.int/dataproducts/asar/CNTR.htm (last accessed May 2005).

Li, F., W. P. Kustas, M. C. Anderson, J. H. Prueger, and R. L. Scott. 2008. Effect of remote sensing spatial resolution on interpreting tower-based flux observations. *Remote Sensing of Environment* 112:337-349.

Li, Z., X. Ren, X. Li, and L. Wang. 2004. Soil moisture measurement and retrieval using ENVISAT ASAR imagery. *IEEE International Geoscience and Remote Sensing Symposium* 0-7803-8742-2/04:3539-3542.

Lin, G. 1996. Monosoonal precipitation responses of shrubs in a cold desert community on the Colorado Plateau. *Oecologia* 106:8-17.

Loew, A. M. W. 2004. *A two parameter backscattering model for bare soil surfaces: from theory to application.* New Jersey: IEEE, pp. II: 811-814.

Magagi, R. D., and Y. H. Kerr. 2001. Estimating surface soil moisture and soil roughness over semiarid areas from the use of the copolarization ratio. *Remote Sensing of Environment* 75:432-445.

Mahafza, B. R. 2000. *Radar system analysis and design using MATLAB.* Boca Raton, FL: CRC Press LLC.

McCabe, M. F., E. F. Wood, R. Wojcik, M. Pan, J. Sheffield, H. Gao, and H. Su. 2008. Hydrological consistency using multi-sensor remote sensing data for water and energy cycle studies. *Remote Sensing of Environment* 112:430-444.

Meade, N. G., L. D. Hinzman, and D. L. Kane. 1999. Spatial Estimation of Soil Moisture Using Synthetic Aperture Radar in Alaska. *Advances in Space Research* 24:935-940.

Meadows, P., and T. Wright. ASAR IMP image quality. 2002 Available from http://www.envisat.esa.int/calval/workshop/asar/20_imp_prod.pdf (last accessed May 2005).

Mela, K., and J. N. Louie. 2001. Correlation length and fractal dimension interpetation from seismic data using variograms and power spectra. *Geophysics* 66:1372-1378.

Moeremans, B., and S. Dautrebande. 2000. Soil moisture evaluation by means of multi-temporal ERS SAR PRI images and interferometric coherence. *Journal of Hydrology* 234:162-169.

Moran, M. S., D. C. Hymer, J. Qi, and Y. Kerr. 2002. Comparison of ERS-2 SAR and Landsat TM imagery for monitoring agricultural crop and soil conditions. *Remote Sensing of Environment* 79:243-252.

Moran, M. S., D. C. Hymer, J. Qi, and E. E. Sano. 2000. Soil moisture evaluation using multi-temporal synthetic aperture radar (SAR) in semiarid rangeland. *Agricultural and Forest Meteorology* 105:69-80.

Moran, M. S., Y. Inoue, and E. M. Barnes. 1997. Opportunities and limitations for image-based remote sensing in precision crop management. *Remote Sensing of Environment* 61:319-346.

Moran, M. S., A. F. Rahman, J. C. Washburne, D. C. Goodrich, M. A. Weltz, and W. P. Kustas. 1996. Combining the Penman-Monteith equation with measurements of surface temperature and reflectance to estimate evaporation rates of semiarid grassland. *Agricultural and Forest Meteorology* 80:87-109.

Moran, M. S., A. Vidal, D. Troufleau, J. Qi, T. R. Clarke, J. P. J. Pinter, T. A. Mitchell, Y. Inoue, and C. M. U. Neale. 1997. Combining multifrequency microwave and optical data for crop management. *Remote Sensing of Environment* 61:96-109.

Moran, S. Recent publications in Remote Sensing of Environment. 2008.

Mroz, A., and Z. Perski. ENVISAT-1/ASAR polarimetric and interferometric data for land cover mapping. 2003 Available from http://www.kfit.uwm.edu.pl/mroz/EARSeL_Symposium_Ghent_2003_paper_Mroz.pdf (last accessed June 2005).

Mustard, J. F. 2001. *Progress Report Year 2, NAG5-6003: The Dynamics of a Semi-Arid Region in Response to Climate and Water-Use Policy.*

Narayanan, R. M., and P. P. Hirsave. 2001. Soil moisture estimation models using SIR-C SAR data: a case study in New Hampshire, USA. *Remote Sensing of Environment* 75:385-396.

NASA Jet Propulsion Laboratory. Imaging Radar. 1994 Available from http://southport.jpl.nasa.gov/ (last accessed August 2004).

National Geospatial-Intelligence Agency. Principles of Radar. Available from http://www.nga.mil/MSISiteContent/StaticFiles/NAV_PUBS/RNM/310ch1.pdf (last accessed December 2009).

Neusch, T., and M. Sties. 1999. Application of the Dubois-model using experimental synthetic aperture radar data for the determination of soil moisture and surface roughness. *ISPRS Journal of Photogrammetry and Remote Sensing* 54:273-278.

Nouvellon, Y., S. Rambal, D. Lo Seen, M. S. Moran, J. P. Lhomme, A. Begue, A. G. Chehbouni, and Y. Kerr. 2000. Modelling of daily fluxes of water and carbon from shortgrass steppes. *Agricultural and Forest Meteorology* 100:137-153.

Oh, Y. 2004. *Comparison of two inversion methods for retrieval of soil moisture and surface roughness from polarimetric radar observation of soil surfaces.* New Jersey: IEEE, pp. II: 807-810.

Paloscia, S., P. Pampaloni, G. Macelloni, and S. Sigismondi. 1999. Microwave remote sensing of hydrological parameters on the NOPEX area. *Agricultural and Forest Meteorology* 98-99:375-387.

Paniconi, C., P. A. Troch, M. Mancini and M. A. Dessena. Soil moisture mapping from ASAR imagery for the Flumendose and Meuse river basins. 2000 Available from http://envisat.esa.int/pub/ESA_DOC/gothenburg/205panic.pdf (last accessed May 2005).

Pavlidis, T. 1982. *Algorithms for graphics and image processing.* Rockville, MD: Computer Science Press.

Prietzsch, C. C., J. S. Famiglietti, and J. A. Devereaux. 1999. Raeumliche und zeitliche Variabilitaet des Bodenwassergehalts abgeleitet aus passiven Radarfernerkundungdaten am Beispiel der Southern Great Plains. *Mitteilungen der Deutschen Bodenkundlichen Gesellschaft* 91:.

Pultz, T. J., Y. Crevier, R. J. Brown, and J. Boisvert. 1997. Monitoring local environmental conditions with SIR-C/X-SAR*1. *Remote Sensing of Environment* 59:248-255.

Rahman, M. M., M. S. Moran, D. P. Thoma, R. Bryant, C. D. H. Collins, T. Jackson, B. J. Orr, and M. Tischler. 2008. Mapping surface roughness and soil moisture using multi-angle radar imagery without ancillary data. *Remote Sensing of Environment* 112:391-402.

Rahman, M. M., M. S. Moran, D. P. Thoma, R. Bryant, E. E. Sano, C. D. H. Collins, S. Skirvin, C. Kershner, and B. J. Orr. 2007. A derivation of roughness correlation length for parameterizing radar backscatter models. *International Journal of Remote Sensing* 28:3995-4012.

Ridley, J., F. Strawbridge, R. Card, and H. Phillips. 1996. Radar backscatter characteristics of a desert surface*1. *Remote Sensing of Environment* 57:63-78.

Rosich, B., and P. Meadows. 2004. Absolute calibration of ASAR level 1 products generated with PF-ASAR. ENVI-CLVL-EOPG-TN-03-0010:.

Saarenketo, T. 1998. Electrical properties of water in clay and silty soils. *Journal of Applied Geophysics* 40:73-88.

Sandia, N. L. Synthetic Aperture Radar. 2004 Available from http://www.sandia.gov/radar/sar.html (last accessed August 2004).

Sano, E. E., M. S. Moran, A. R. Huete, and T. Miura. 1998. C- and Multiangle Ku-Band Synthetic Aperture Radar Data for Bare Soil Moisture Estimation in Agricultural Areas. *Remote Sensing of Environment* 64:77-90.

Satalino, G., G. Pasquariello, F. Mattia, and L. Dente. 2004. *On the accuracy of soil moisture content retrieved, at pixel, segment or field scale, from Advanced-SAR data. A simulation study.* New Jersey: IEEE, pp. 3532-3535.

Schaber, G. G. 1998. *SAR studies in two Arizona deserts [microform] : sand penetration, geology, and the detection of military ordinance debris.* Flagstaff, Ariz. : Denver, Colo. : U.S. Dept. of the Interior, U.S. Geological Survey ; Books and Open-File Reports Section, distributor].

Schoups, G., P. A. Troch, and N. Verhoest. 1998. Soil Moisture Influences on the Radar Backscattering of Sugar Beet Fields. *Remote Sensing of Environment* 65:184-194.

Schowengerdt, R. A. 1997. *Remote Sensing: Models and methods for image processing.* San Diego, CA: Academic Press.

———1983. *Techniques for image processing and classification in remote sensing.* New York, NY: Academic Press, Inc.

Schreiber, W. F. 1993. *Fundamentals of electronic imaging systems.* New York, NY: Springer Verlag.

Schuler, D. L., J. Lee, and T. L. Ainsworth. 1999. Compensation of Terrain Azimuthal Slope Effects in Geophysical Parameter Studies Using Polarimetric SAR Data. *Remote Sensing of Environment* 69:139-155.

Shoshany, M., T. Svoray, P. J. Curran, G. M. Foody and A. Perevolotsky. ERS-2 SAR Soil Moisture and Herbaceous Biomass Monitoring across a semi-arid transect in Israel. 1998 Available from http://conferences.esa.int/98c07/papers/P100.PDF (last accessed May 2007).

Sikdar, M. C. I. 2004. *A modified empirical model for soil moisture estimation in vegetated areas using SAR data.* New Jersey: IEEE, pp. II: 803-806.

Small, D., B. Rosich, E. Meier, and D. Nuesch. 2004. *Geometric calibration and validation of ASAR imagery.* ESA, .

Srivastava, S. K., and V. Jayaraman. 2001. RELATING INTERFEROMETRIC SIGNATURE OF REPEAT PASS ERS-1 SAR SIGNALS TO DYNAMIC LAND COVER CHANGES. *Acta Astronautica* 48:37-44.

Srivastava, S. K., N. Yograjan, V. Jayaraman, P. P. N. Rao, and M. G. Chandrasekhar. 1997. On the relationship between ERS-1 SAR/backscatter and surface/sub-surface soil moisture variations in vertisols*1. *Acta Astronautica* 40:693-699.

Stanford, K. 2003. *Lecture Notes: Remote Sensing Techniques I and II, G.L. Berlin.*

———2002. Specialty Report: Soils.

Stein, Alfred ed.//Van der Meer,Freek ed. 1999. *Spatial statistics for remote sensing.* Boston, MS: Kluwer Academic Publishers.

Su, Z., P. A. Troch, and F. P. De Troch. 1997. A method for retrieving soil moisture using active microwave data. *Physics and Chemistry of the Earth* 22:235-239.

Sullivan, R. J. 2000. *Microwave radar : imaging and advanced concepts.* Boston ; London : Artech House.

Taconet, O., M. Benallegue, D. Vidal-Madjar, L. Prevot, M. Dechambre, and M. Normand. 1994. Estimation of soil and crop parameters for wheat from airborne radar backscattering data in C and X bands*1. *Remote Sensing of Environment* 50:287-294.

Taconet, O., D. Vidal-Madjar, C. Emblanch, and M. Normand. 1996. Taking into account vegetation effects to estimate soil moisture from C-band radar measurements. *Remote Sensing of Environment* 56:52-56.

Tansey, K. J., A. C. Millington, A. M. Battikhi, and K. H. White. 1999. Monitoring soil moisture dynamics using satellite imaging radar in northeastern Jordan. *Applied Geography* 19:325-344.

Tansey, K. J., K. H. White, A. C. Millington and A. M. Battikhi. Comparison of modelled backscatter response and ERS-1 SAR data for desert surfaces, the eastern Badia of Jordan. 2004 Available from http://earth.esa.int/symposia/papers/tansey/ (last accessed December 2004).

Taylor, S. A. 1961. *Evaluating soil water; a bulletin based on research conducted under the sponsorship of Western regional research projects W-9 and W-29 with the 12 Western States in cooperation with the U. S. Department of Agriculture,*

Agricultural Research Service, Logan: Agricultural Experiment Station, Utah State University.

Thoma, D., M. S. Moran, R. Bryant, M. M. Rahman, C. Holifield, and S. Skirvin. 2006. Comparison of two methods for extracting surface soil moisture from C-band radar imagery. *Water Resources Research* 42:.

Thoma, D. P., M. S. Moran, R. Bryant, M. M. Rahman, C. D. Holifield Collins, T. O. Keefer, R. Noriega, I. Osman, S. M. Skrivin, M. A. Tischle, D. D. Bosch, P. J. Starks, and C. Peters-Lidard. 2008. Appropriate scale of soil moisture retrieval from high resolution radar imagery for bare and minimally vegetated soils. *Remote Sensing of Environment* 112:403-414.

Tien, K. C., R. D. De Roo, J. Judge, and H. Pham. 2007. Comparison of Calibration Techniques for Ground-Based C-Band Radiometers. *IEEE Geoscience and Remote Sensing Letters* 4:83-87.

Troch, P. A. Remote Sensing of Soil Moisture Using EMAC/ESAR Data. 1996 Available from http://esapub.esrin.esa.it/eoq/eoq53/troc53.htm (last accessed October 2004).

Ulaby, Fawwaz T.//Moore, Richard K.//Fung,Adrian K. 1986. *Microwave remote sensing: active and passive.* Norwood, MA: Artech House, Inc.

Ulaby, F. T., P. P. Batlivala, and M. C. Dobson. 1978. Microwave backscatter dependence on surface roughness, soil moisture, and soil texture: part I - bare soil. *IEEE Transactions on Geoscience and Remote Sensing* GE-16:286-295.

Ulaby, F. T., P. C. Dubois, and J. van Zyl. 1996. Radar mapping of surface soil moisture. *Journal of Hydrology* 184:57-84.

United States Interagency Ad Hoc Working Group,on SAR. 1996. *Operational use of civil space-based Synthetic Aperture Radar (SAR).* Washington, D.C.? : U.S. National Aeronautics and Space Administration.

van der Meer, F. 1999. Can we map swelling clays with remote sensing? *International Journal of Applied Earth Observation and Geoinformation* 1:27-35.

van Es, H., and C. Ogden. Water in Soil. 1997 Available from http://www.css.cornell.edu/faculty/hmv1/watrsoil/theta.htm (last accessed January 2010).

Vivoni, E. R., M. Gebremichael, C. Watts, R. Bindlish, and T. J. Jackson. 2008. Comparison of ground-based and remotely sensed surface soil moisture estimates over complex terrain during SMEX04. *Remote Sensing of Environment* 112:314-325.

Wagner, W., G. Lemoine, and H. Rott. 1999. A Method for Estimating Soil Moisture from ERS Scatterometer and Soil Data. *Remote Sensing of Environment* 70:191-207.

Wagner, W., and K. Scipal. 2000. Der Einsatz von Radarsatelliten zur Ueberwachung der Bodenwasserresourcen in Afrika. *Petermanns Geographische Mitteilungen* 144:.

Wang, C., J. Qi, S. Moran, and R. Marsett. 2004. Soil moisture estimation in a semiarid rangeland using ERS-2 and TM imagery. *Remote Sensing of Environment* 90:178-189.

Wang, L., Z. Li, and X. Ren. 2004. *The effects of vegetation in soil moisture retrieval using microwave radiometer data.* New Jersey: IEEE, .

Wang, Y., J. L. Day, and F. W. Davis. 1998. Sensitivity of Modeled C- and L-Band Radar Backscatter to Ground Surface Parameters in Loblolly Pine Forest. *Remote Sensing of Environment* 66:331-342.

Western Upper Peninsula Center for Science, Mathematics,& Environmental Education. Get the dirt on soils - a teaching unit for Gr. 4-8. Available from http://wupcenter.mtu.edu/education/forest3.htm (last accessed September 2004).

Wigneron, J. P., P. Ferrazzoli, A. Olioso, P. Bertuzzi, and A. Chanzy. 1999. A Simple Approach To Monitor Crop Biomass from C-Band Radar Data. *Remote Sensing of Environment* 69:179-188.

Wolf, C. Radar Tutorial. Available from http://www.radartutorial.eu/ (last accessed December 2009).

Wooster, M. J., and D. A. Rothery. 1997. Thermal monitoring of Lascar volcano, Chile, using infrared data from the along-track scanning radiometer: a 1992-1995 time series. *Bulletin of Volcanology* 58:566-579.

Yilmaz, M. T., E. R. Hunt Jr., L. D. Goins, S. L. Ustin, V. C. Vanderbilt, and T. J. Jackson. 2008. Vegetation water content during SMEX04 from ground data and Landsat 5 Thematic Mapper imagery. *Remote Sensing of Environment* 112:350-362.

Zribi, M., N. Baghdadi, N. Holah, and O. Fafin. 2005. New methodology for soil surface moisture estimation and its application to ENVISAT-ASAR multi-incidence data inversion. *Remote Sensing of Environment* 96:485-496.

Zribi, M., N. Baghdadi, N. Holah, O. Fafin, and C. Guerin. 2005. Evaluation of a rough soil surface description with ASAR-ENVISAT radar data. *Remote Sensing of Environment* 95:67-76.

Zribi, M., V. Ciarletti, and O. Taconet. 2000. Validation of a Rough Surface Model Based on Fractional Brownian Geometry with SIRC and ERASME Radar Data over Orgeval. *Remote Sensing of Environment* 73:65-72.

Zribi, M., and M. Dechambre. 2003. A new empirical model to retrieve soil moisture and roughness from C-band radar data. *Remote Sensing of Environment* 84:42-52.

APPENDICES

APPENDIX A. RALEIGH CRITERION AND PEAK & OLIVER MODIFIED CRITERION EVALUATION

Site #	h' (cm)	A (cm)	β	Raleigh	P&O	β	Raleigh	P&O	β	Raleigh	P&O	β	Raleigh	P&O
3	1,25	5,3	38,9	rough	intermediate	41,2	rough	rough	43,5	rough	rough	40,5	smooth	intermediate
5	3,25	5,3	38,9	rough	rough	41,2	rough	rough	43,5	rough	rough	40,5	rough	intermediate
7	2,2	5,3	38,9	rough	rough	41,2	rough	rough	43,5	rough	rough	40,5	rough	intermediate
8	2,3	5,3	38,9	rough	rough	41,2	rough	rough	43,5	rough	rough	40,5	rough	intermediate
9	2,25	5,3	38,9	rough	rough	41,2	rough	rough	43,5	rough	rough	40,5	rough	intermediate
10	1,45	5,3	38,9	rough	rough	41,2	rough	rough	43,5	rough	rough	40,5	smooth	intermediate
11	4,1	5,3	38,9	rough	rough	41,2	rough	rough	43,5	rough	rough	40,5	rough	rough
14	3,25	5,3	38,9	rough	rough	41,2	rough	rough	43,5	rough	rough	40,5	rough	intermediate
16	3,05	5,3	38,9	rough	rough	41,2	rough	rough	43,5	rough	rough	40,5	rough	intermediate
19	2,45	5,3	38,9	rough	rough	41,2	rough	rough	43,5	rough	rough	40,5	rough	intermediate
22	1,8	5,3	38,9	rough	rough	41,2	rough	rough	43,5	rough	rough	40,5	smooth	intermediate
25	3	5,3	38,9	rough	rough	41,2	rough	rough	43,5	rough	rough	40,5	rough	intermediate
26	2,65	5,3	38,9	rough	rough	41,2	rough	rough	43,5	rough	rough	40,5	rough	intermediate
28	1,55	5,3	38,9	rough	rough	41,2	rough	rough	43,5	rough	rough	40,5	smooth	intermediate
30	1,6	5,3	38,9	rough	rough	41,2	rough	rough	43,5	rough	rough	40,5	smooth	intermediate
39	2,35	5,3	38,9	rough	rough	41,2	rough	rough	43,5	rough	rough	40,5	rough	intermediate
41	1,2	5,3	38,9	rough	intermediate	41,2	rough	rough	43,5	rough	rough	40,5	smooth	intermediate
43	0,5	5,3	38,9	smooth	intermediate	41,2	rough	rough	43,5	rough	rough	40,5	smooth	smooth
48	2,6	5,3	38,9	rough	rough	41,2	rough	rough	43,5	rough	rough	40,5	rough	intermediate
48	1,4	5,3	38,9	rough	rough	41,2	rough	rough	43,5	rough	rough	40,5	smooth	intermediate
49	2,35	5,3	38,9	rough	rough	41,2	rough	rough	43,5	rough	rough	40,5	rough	intermediate
51	2,05	5,3	38,9	rough	rough	41,2	rough	rough	43,5	rough	rough	40,5	rough	intermediate
52	1,7	5,3	38,9	rough	rough	41,2	rough	rough	43,5	rough	rough	40,5	smooth	intermediate
54	1,1	5,3	38,9	rough	intermediate	41,2	rough	rough	43,5	rough	rough	40,5	smooth	intermediate
55	3,15	5,3	38,9	rough	rough	41,2	rough	rough	43,5	rough	rough	40,5	rough	intermediate
56	4,55	5,3	38,9	rough	rough	41,2	rough	rough	43,5	rough	rough	40,5	rough	rough
57	1,1	5,3	38,9	rough	intermediate	41,2	rough	rough	43,5	rough	rough	40,5	smooth	intermediate
58	2,5	5,3	38,9	rough	rough	41,2	rough	rough	43,5	rough	rough	40,5	rough	intermediate
59	3,05	5,3	38,9	rough	rough	41,2	rough	rough	43,5	rough	rough	40,5	rough	intermediate
62	2,7	5,3	38,9	rough	rough	41,2	rough	rough	43,5	rough	rough	40,5	rough	intermediate
64	1,3	5,3	38,9	rough	rough	41,2	rough	rough	43,5	rough	rough	40,5	smooth	intermediate
68	2,55	5,3	38,9	rough	rough	41,2	rough	rough	43,5	rough	rough	40,5	rough	intermediate
72	1,75	5,3	38,9	rough	rough	41,2	rough	rough	43,5	rough	rough	40,5	smooth	intermediate
74	2,1	5,3	38,9	rough	rough	41,2	rough	rough	43,5	rough	rough	40,5	rough	intermediate
76	1,2	5,3	38,9	rough	intermediate	41,2	rough	rough	43,5	rough	rough	40,5	smooth	intermediate
78	1,35	5,3	38,9	rough	rough	41,2	rough	rough	43,5	rough	rough	40,5	smooth	intermediate
85	1,9	5,3	38,9	rough	rough	41,2	rough	rough	43,5	rough	rough	40,5	smooth	intermediate
88	2,2	5,3	38,9	rough	rough	41,2	rough	rough	43,5	rough	rough	40,5	rough	intermediate
92	1,75	5,3	38,9	rough	rough	41,2	rough	rough	43,5	rough	rough	40,5	smooth	intermediate
93	2,4	5,3	38,9	rough	rough	41,2	rough	rough	43,5	rough	rough	40,5	rough	intermediate
96	4,1	5,3	38,9	rough	rough	41,2	rough	rough	43,5	rough	rough	40,5	rough	rough
98	1,65	5,3	38,9	rough	rough	41,2	rough	rough	43,5	rough	rough	40,5	smooth	intermediate
103	2,75	5,3	38,9	rough	rough	41,2	rough	rough	43,5	rough	rough	40,5	rough	intermediate
104	4,1	5,3	38,9	rough	rough	41,2	rough	rough	43,5	rough	rough	40,5	rough	rough
109	2,7	5,3	38,9	rough	rough	41,2	rough	rough	43,5	rough	rough	40,5	rough	intermediate
110	1,45	5,3	38,9	rough	rough	41,2	rough	rough	43,5	rough	rough	40,5	smooth	intermediate
111	1,45	5,3	38,9	rough	rough	41,2	rough	rough	43,5	rough	rough	40,5	smooth	intermediate
113	3,05	5,3	38,9	rough	rough	41,2	rough	rough	43,5	rough	rough	40,5	rough	intermediate
117	1,4	5,3	38,9	rough	rough	41,2	rough	rough	43,5	rough	rough	40,5	smooth	intermediate
120	2,05	5,3	38,9	rough	rough	41,2	rough	rough	43,5	rough	rough	40,5	rough	intermediate
KFarm1	4,95	5,3	38,9	rough	rough	41,2	rough	rough	43,5	rough	rough	40,5	rough	rough
Kachina Met St	3,5	5,3	38,9	rough	rough	41,2	rough	rough	43,5	rough	rough	40,5	rough	intermediate
Navajo Farm	2,65	5,3	38,9	rough	rough	41,2	rough	rough	43,5	rough	rough	40,5	rough	intermediate
Navajo Farm	1,05	5,3	38,9	rough	intermediate	41,2	rough	rough	43,5	rough	rough	40,5	smooth	intermediate

APPENDIX B. VEGETATION AT THE SAMPLE SITES

	Dominant	Dominant	Dominant	Other	Abbreviations	Genus	Species	Common name
Point#	Veg type in **BOLD**	shrub	grass		SAVE GUSA	Sarcobatus Gutierrezia	vermiculatus sarothrae	greasewood snakeweed
2	shrubland	**ATCA**	unk grass		BRTE	Bromus	tectorum	cheat grass
3	grassland	Ephedra spp., GUSA	**ORHY**		ATCA	Atriplex	canescens	Four wing saltbush
5	shrubland	**ATCA**	ORHY	SPAM, BRTE	LEMO	Lepidium	momtanum	pepperweed
6	grassland		**ORHY, BOGR**	low density veg- sparse	CELA	Ceratoides	lanata	winter fat
7	shrubland	**SAVE**			HIJA	Hilaria	jamesii	galleta grass
8	grassland	GUSA	**ORHY**	Ephedra, Juniper, YUAN	ORHY	Oryzopsis	hymoides	indian rice grass
9	grassland	Ephedra spp., GUSA	**ORHY, BOGR**	YUAN	CHNA	Chrysothamnus	nauseosus	rabbit brush
10	grassland	CHNA, GUSA	**ORHY**	fallow ag field	YUAN	Yucca	angustissima	narrow leaf yucca
11	grassland	CHNA, GUSA	ORHY, SPAI	dow density veg on sand dunes	PHCE	Phacelia	crenulata	scorpion weed
14	grassland	ATCA	**ORHY**	HIJA, SPFL,BRTE	SPAI	Sporobolis	airoides	alkalai sacaton-grass
16	barren	GUSA, CHNA	unk grass	very low density veg	SPAM	Sphaeralcea	ambigua	globe mallow
16	grassland	CHNA, GUSA,	unk grass		unk			unknown plant
19	grassland	CHNA	**SPAI**	ORHY, YUAN	SPFL	Sporobolis	flexuosus	mesa dropseed-grass
22	grassland	GUSA	**ORHY**	Ephedra, Juniper, YUAN	BOGR	Bouteloua	gracilis	blue grama grass
25	shrubland	**CHNA,GUSA**		no grasses present	HOJU	Hordeum	jubatum	fox tail barley grass
26	grassland	CHNA	**HIJA**	GUSA, YUAN, BRTE,		Salsola		tumbleweed, russian thistle
28	shrubland	**SAVE**	HIJA	**claret cup cactus**	BSC	Biological Soil Crusts		
30	grassland	GUSA, CHNA	**ORHY**	BOGR, HOJU, juniper spp.	ARFI	Artemesia	filifolia	sand sage
39	grassland	ATCA, Ephedra	unk					
41	shrubland	**SAVE**						
43	shrubland	**ATCA**		lots of organic soil-dark				
48	grassland	ATCA	**ORHY**					
48	grassland	ATCA	**ORHY**	guard rail 250m west (First site)				
49	grassland			**SPAM (annual?) LEMO**				
51	shrubland	**CHNA,GUSA**	HIJA	LEMO				
52	grassland	ATCA, ARFI	unk	low density shrubs nearby				
54	grassland	ATCA	**HIJA**					
55	shrubland	unkown	unknown	unk succulent				
56	grassland	GUSA	**PHCE**	ephedra, SPAI				
57	grassland		**SPFL**					
58	grassland	ATCA, Cholla spp.	**HIJA**					
59	shrubland	**CHNA**	ORHY	GUSA, SPFL				
61	shrubland	ATCA						
62	mixed	GUSA, SAVE	unk grass					
64	shrubland	**Ephedra spp.**	BOGR	ORHY, BRTE, HOJU, YUAN, GUSA				
68	shrubland	**CELA**		Cholla spp.				
72	shrubland	**GUSA, ATCA**	Salsola	old farm plot				
73	shrubland	**Ephedra spp.**		CHNA				
74	grassland	Ephedra	**ORHY**	GUSA, BOGR, HIJA				
76	grassland		unk	sparse grasslands				
78	grassland		unk					
79	mixed		**LEMO**	LEMO, site near farm				
82	farmland	none	**none**	recently tilled soil SE edge of K-town				
85	grassland	CELA	**HIJA**					
86	barren			minor grasses				
88	shrubland	**GUSA**	BOGR	ATCA				
90	shrubland	**GUSA**	BOGR	ATCA, Ephedra.				
92	shrubland	**Ephedra spp.**	HIJA	CELA,ATCA,				
93	shrubland	**GUSA, ATCA**	ORHY	BSC,				
96	grassland	GUSA, Ephedra spp.	**BOGR, ORHY**	HOJU, HIJA, YUAN				
98	shrubland	GUSA		sparse PJ present				
102	grassland	**ATCA**	unk grass	CHNA, GUSA				
103	grassland	Ephedra spp.	unk grass					
103	grassland	Ephedra spp.	unk grass					
103	grassland	Ephedra spp.	unk grass					
103	grassland	Ephedra spp.	unk grass					
104	grassland	Ephedra spp., GUSA	**ORHY, BOGR**	YUAN				
107	shrubland	**SAVE**		GUSA, SPAM				
109	grassland	GUSA, YUAN	**BOGR, ORHY**					
110	shrubland	**GUSA**	ORHY	ATCA				
111	shrubland	**ATCA**		GUSA,LEMO				
112	shrubland	ARFI		old farm plot				
113	grassland	GUSA	**BRTE**					
114	barren			Navajo farm				
117	grassland	Ephedra spp.,	**ORHY**	Juniper				
120	grassland	GUSA	**BOGR, ORHY**					
Kachina	shrubland	**ATCA**	SPAI					
K-farm1	grassland	CHNA, GUSA	**ORHY, BOGR**	*adjacent to current ag site (pt 10)				
Tovar	grassland	ATCA	**ORHY**					

APPENDIX C. SOIL MOISTURE RATE AT THE SAMPLE SITES

Sample	Soil-moist	Tin	Wet + Tin	Dry + Tin	Soil-dry	Percentage	Sample	u=w/s
2	10,15	26,28	36,43	35,27	8,99	**12,90**	**2**	0,129
3	10,11	27,35	37,46	36,66	9,31	**8,59**	**3**	0,086
6	10,12	28,59	38,71	38,12	9,53	**6,19**	**6**	0,062
7	10,56	26,70	37,26	36,25	9,55	**10,58**	7	0,106
9	10,19	27,39	37,58	37,12	9,73	**4,73**	**9**	0,047
10	10,24	28,10	38,34	37,62	9,52	**7,56**	**10**	0,076
11	10,10	28,97	39,07	38,84	9,87	**2,33**	**11**	0,023
14	10,08	28,66	38,74	38,40	9,74	**3,49**	**14**	0,035
16	10,05	29,43	39,48	38,77	9,34	**7,60**	**16**	0,076
16	10,43	27,71	38,14	37,08	9,37	**11,31**	**16**	0,113
19	10,18	27,30	37,48	37,12	9,82	**3,67**	**19**	0,037
22	10,14	26,84	36,98	36,35	9,51	**6,62**	**22**	0,066
25	10,17	29,79	39,96	39,62	9,83	**3,46**	**25**	0,035
26	10,25	27,48	37,73	37,05	9,57	**7,11**	**26**	0,071
28	10,09	25,43	35,52	34,82	9,39	**7,45**	**28**	0,075
30	10,14	26,39	36,53	35,91	9,52	**6,51**	**30**	0,065
41	10,12	27,86	37,98	37,16	9,30	**8,82**	**41**	0,088
43	10,15	28,79	38,94	38,26	9,47	**7,18**	**43**	0,072
48	10,05	27,72	37,77	37,56	9,84	**2,13**	**48**	0,021
49	10,38	28,04	38,42	37,96	9,92	**4,64**	**49**	0,046
54	10,06	29,45	39,51	38,91	9,46	**6,34**	**54**	0,063
55	10,57	26,51	37,08	35,65	9,14	**15,65**	**55**	0,156
56	10,24	28,80	39,04	38,50	9,70	**5,57**	**56**	0,056
57	10,19	28,32	38,51	37,80	9,48	**7,49**	**57**	0,075
58	10,23	28,18	38,41	37,57	9,39	**8,95**	**58**	0,089
59	10,19	29,99	40,18	39,89	9,90	**2,93**	**59**	0,029
61	10,22	28,67	38,89	37,72	9,05	**12,93**	**61**	0,129
62	10,41	30,75	41,16	40,71	9,96	**4,52**	**62**	0,045
64	10,08	29,44	39,52	39,24	9,80	**2,86**	**64**	0,029
68	10,23	27,43	37,66	36,85	9,42	**8,60**	**68**	0,086
72	10,14	27,41	37,55	36,90	9,49	**6,85**	**72**	0,068
73	10,01	27,87	37,88	37,64	9,77	**2,46**	**73**	0,025
74	10,05	25,44	35,49	35,02	9,58	**4,91**	**74**	0,049
76	10,22	28,44	38,66	37,57	9,13	**11,94**	**76**	0,119
78	9,96	28,14	38,10	37,69	9,55	**4,29**	**78**	0,043
79	10,18	28,93	39,11	38,50	9,57	**6,37**	**79**	0,064
85	10,08	29,36	39,44	38,49	9,13	**10,41**	**85**	0,104
86	10,17	27,49	37,66	37,38	9,89	**2,83**	**86**	0,028
90	10,03	28,60	38,63	38,29	9,69	**3,51**	**90**	0,035
92	10,01	28,05	38,06	37,62	9,57	**4,60**	**92**	0,046
93	10,13	29,86	39,99	39,63	9,77	**3,68**	**93**	0,037
96	10,06	28,81	38,87	38,56	9,75	**3,18**	**96**	0,032
98	10,10	30,77	40,87	40,17	9,40	**7,45**	**98**	0,074
102	10,03	27,41	37,44	36,99	9,58	**4,70**	**102**	0,047
103	10,01	27,79	37,80	37,35	9,56	**4,71**	**103**	0,047
104	10,11	27,52	37,63	37,26	9,74	**3,80**	**104**	0,038
109	10,19	27,66	37,85	37,41	9,75	**4,51**	**109**	0,045
110	10,14	28,84	38,98	38,64	9,80	**3,47**	**110**	0,035
111	10,19	25,26	35,45	34,89	9,63	**5,82**	**111**	0,058
112	10,14	29,18	39,32	38,14	8,96	**13,17**	**112**	0,132
113	10,02	28,17	38,19	37,41	9,24	**8,44**	**113**	0,084
114	10,12	29,32	39,44	39,28	9,96	**1,61**	**114**	0,016
114-1	10,16	27,87	38,03	37,82	9,95	**2,11**	**114-1**	0,021
117	10,06	27,61	37,67	37,02	9,41	**6,91**	**117**	0,069
120	10,19	27,95	38,14	37,46	9,51	**7,15**	**120**	0,072
K MET	10,01	25,91	35,92	35,55	9,64	**3,84**	**K MET**	0,038
K Farm 1	10,28	28,57	38,85	38,03	9,46	**8,67**	**K Farm 1**	0,0867

APPENDIX D. SOIL TEXTURE AT THE SAMPLE SITES

Soil Samples 2 through 28

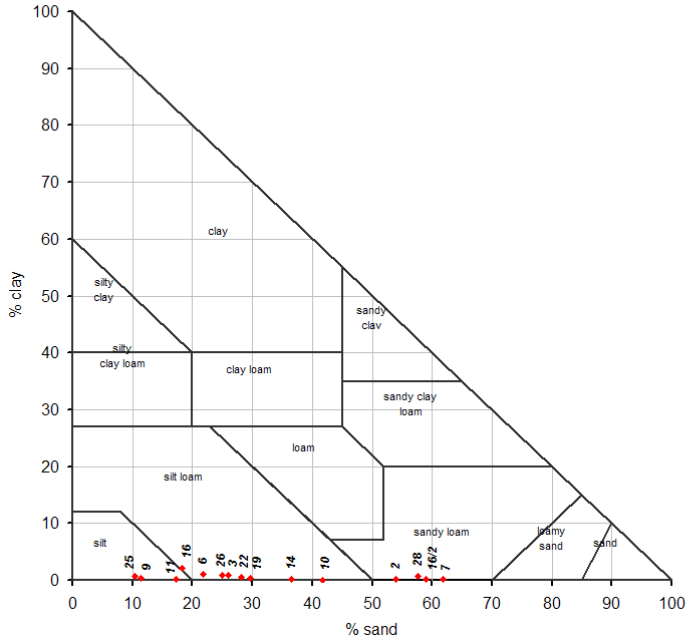

Soil Samples 30 through 68

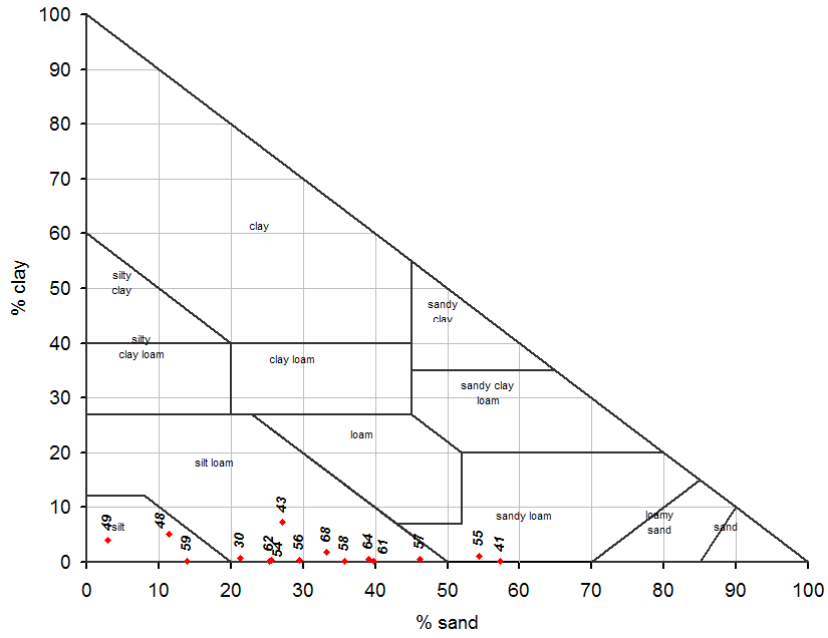

Soil Samples 72 through 103

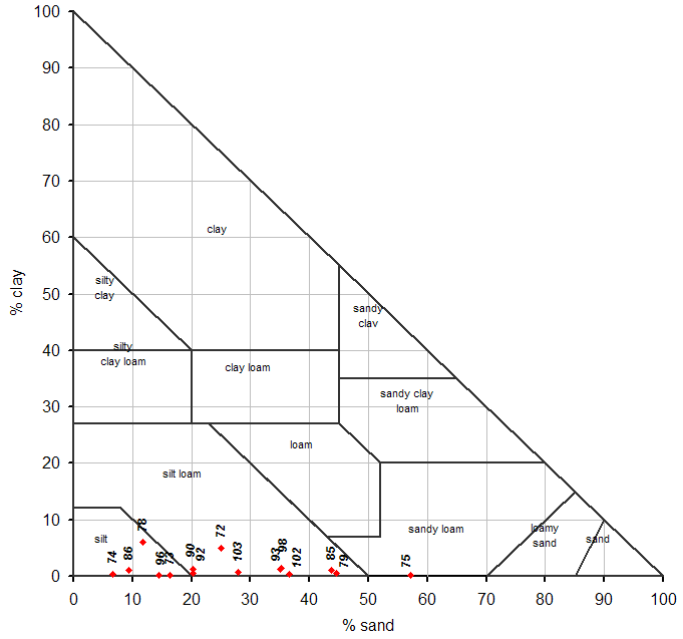

Soil Samples 104 through 120

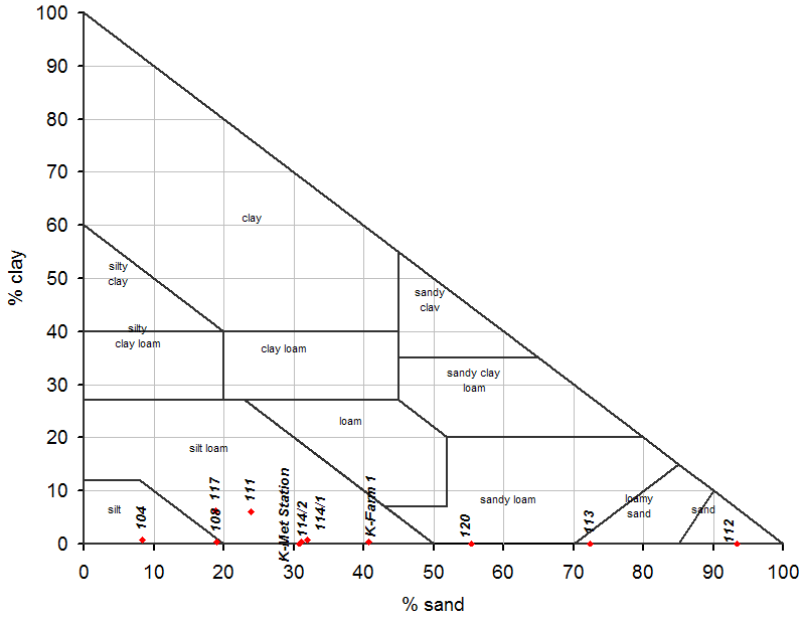

APPENDIX E. IN-FIELD H_{RMS} VALUES

Site	hRMS
3	0,515
5	2,254
7	1,072
8	1,469
9	1,041
10	0,789
11	2,437
14	2,334
16	1,771
19	1,601
22	0,962
25	2,319
26	1,575
28	1,105
30	0,918
39	1,389
41	1,079
43	1,001
48	1,522
48	0,887
49	1,949
51	1,847
52	0,791
54	1,255
55	1,759
56	2,846
57	0,553
58	1,387
59	2,068
62	1,378
64	0,656
68	1,862
72	1,071
74	0,925
76	0,447
78	1,127
85	1,688
88	1,019
92	1,836
93	1,577
96	2,190
98	1,199
103	1,462
104	2,607
109	1,239
110	2,326
111	1,407
113	1,845
117	0,758
120	0,894
KFarm1	2,495
Kachina Met Station	2,381
Navajo Farm	1,434
Navajo Farm	0,547

APPENDIX F. FIELD WORK RESULTS TABLE

Site #	Easting	Northing	Altitude (m)	Aspect	hRMS	SoilMoist%	Vegetation	Soil Texture	% Sand	% Clay	Raleigh Criterion	Peake&Oliver	Lc
2	557100,56	3944578,69	1728.52			12,9		Sandy Loam	54	0,2			
3	535613,61	4002192,81	6150,46	3-5% W	0,51	8,6	grassland	Silt Loam	26	0,8	smooth	intermediate	1,6
5	557545,25	3941323,29	1714,02	<5%	2,25		shrubland				rough	intermediate	5,1
6	517021,78	3976409,37	1728.60	<2% N		6,2		Silt Loam	22	1,1			
7	550998,72	3992464,51	1821,98	0	1,07	10,6	shrubland	Sandy Loam	62	0,1	rough	intermediate	1,6
8	519706,04	3944003,70	1596,67	<2% S	1,47		grassland				rough	intermediate	2,2
9	503719,50	3991546,99	1678.46	3-5% W	1,04	4,7	grassland	Silt	11	0,3	rough	intermediate	1,6
10	528437,91	3984853,51	1775,44	<2% E	0,79	7,6	grassland	Silt Loam	42	0,1	smooth	intermediate	1,6
11	503719,50	3991546,99	5506,79	5% W	2,44	2,3	grassland	Silt	17	0,2	rough	rough	5,9
14	511214,28	3928995,84	0,00	<5% W	2,33	3,5	grassland	Silt Loam	37	0,2	rough	intermediate	5,4
16	556269,80	3951631,63	5858,26	0	1,77	11,3	barren	Silt	18	2,2	rough	intermediate	3,1
19	503221,33	3947062,73	1594,88	3% NW	1,60	3,7	grassland	Silt Loam	30	0,4	rough	intermediate	2,6
22	509389,76	3972979,18	1958,93	5% N	0,96	6,6	grassland	Silt Loam	28	0,5	**smooth**	intermediate	1,6
25	535685,84	3941058,64	1588,96	<3%	2,32	3,5	shrubland	Silt	10	0,8	rough	intermediate	5,4
26	526055,72	3988978,98	6073,64	0	1,58	7,1	grassland	Silt Loam	25	1	rough	intermediate	2,5
28	558923,42	3976406,34	1799,67	3-5% W	1,10	7,5	shrubland	Sandy Loam	58	0,7	smooth	intermediate	1,6
30	526833,70	3988166,12	6124,25	0	0,92	6,5	grassland	Silt Loam	21	0,8	smooth	intermediate	1,6
39	543933,10	3947126,86	5379,67	0	1,39		grassland	Sandy Loam	57	0,1	rough	intermediate	1,9
41	547541,77	3988035,42	1796,89	0	1,08	8,8	shrubland	Silt Loam	27	7,3	smooth	intermediate	1,6
43	533583,38	3963083,85	0,00	<2% S-SW	1,00	7,2	shrubland	Silt	11	5,2	smooth	smooth	1,6
48	545048,40	3958603,80	514,94	<3%	1,52	2,1	grassland	Silt	11	5,2	rough	intermediate	2,3
48	545051,70	3958603,48	5621,00	<3%	0,89		grassland	Silt	3	4,1	smooth	intermediate	1,6
49	569876,29	3943598,81	5910,43	<5%	1,95	4,6	grassland				rough	intermediate	3,8
51	552133,60	3977834,97	0,00	0	1,85		shrubland				rough	intermediate	3,4
52	562395,71	3944760,21	5783,66	<3% N	0,79		grassland				smooth	intermediate	1,6
54	524529,86	4000714,83	1749,18	0	1,25	6,3	grassland	Silt Loam	26	0,3	smooth	intermediate	1,6
55	538929,68	3947875,73	5304,57	0	1,76	15,6	shrubland	Sandy Loam	54	1,2	rough	intermediate	3,1
56	545354,46	3935607,89	0,00	<2%	2,85	5,6	grassland	Silt Loam	29	0,4	rough	rough	8,1
57	519880,01	3950129,61	5463,36	0	0,55	7,5	grassland	Silt Loam	46	0,5	smooth	intermediate	1,6
58	558823,04	3941862,57	5662,14	0	1,39	8,9	grassland	Silt Loam	36	0,2	**rough**	intermediate	1,9
59	515469,25	3938803,40	1597,52	5-7% N-NW	2,07	2,9	shrubland	Silt	14	0,2	rough	intermediate	4,3
61	572243,65	3944655,32	1823,00	<2%		**12,9**		Silt Loam	40	0,1			
62	538980,72	3944933,77	5297,33		1,38	4,5	mixed	Silt Loam	25	0,2	rough	intermediate	1,9
64	508671,76	3996902,66	5492,39	3-5% N	0,66	2,9	shrubland	Silt Loam	39	0,5	smooth	intermediate	1,6
68	556956,52	2983167,71	1855,21	0	1,86	8,6	shrubland	Silt Loam	33	1,8	rough	intermediate	3,5
72	544417,59	3985521,41	1787,07	0	1,07	6,8	shrubland	Silt Loam	25	5	smooth	intermediate	1,6
73	528921,30	3960545,40	1676.12			2,5		Silt	16	0,2			
74	514863,85	3948038,31	1693,05	<2% E	0,92	4,9	grassland	Silt	7	0,3	rough	intermediate	1,6
76	568647,97	3945964,60	5930,00	0	0,45	11,9	grassland	Sandy Loam	57	0,1	smooth	intermediate	1,6
78	530326,71	3990024,87	1898,98	0	1,13	4,3	grassland	Silt	12	6,1	smooth	intermediate	1,6
79	518283,78	3992222,90	1810.72	<2% W		6,4		Silt Loam	45	0,6			
85	549042,42	3973417,82	1829,87	0	1,69	10,4	grassland	Silt Loam	44	1,1	smooth	intermediate	2,8
86	515050,84	3930717,78	1523.57	0		2,8		Silt	9	1,1			
88	509699,28	3964189,32	1637,34	0	1,02		shrubland				rough	intermediate	1,6
90	506618,43	3974494,40	1818.31	<2% S		3,5		Silt Loam	20	1,2			

92	524407,26	3960430,53	1734,88	<2% S	1,84	4,6	shrubland	Silt Loam	20	0,5	smooth	intermediate	3,4
93	534260,66	3988579,94	1804,81	<2% E	1,58	3,7	shrubland	Silt Loam	35	1,2	rough	intermediate	2,5
96	510071,57	3987537,56	5779,09	<2% NE	2,19	3,2	grassland	Silt	14	0,2	rough	rough	4,8
98	530581,92	399581,97	1881,74	0	1,20	7,4	shrubland	Silt Loam	35	1,4	smooth	intermediate	1,6
102	537211,92	3973753,75	1729.83	<3% E-NE		4,7		Silt Loam	37	0,4			
103	545579,90	3942386,72	5688,74	<3% E	1,46	4,7	grassland	Silt Loam	28	0,8	rough	intermediate	2,1
104	503601,42	3994338,51	5476,72	3-5% N	2,61	3,8	grassland	Silt	8	0,8	rough	rough	6,8
109	511442,94	3952324,07	1688,60	0	1,24	4,5	grassland	Silt	19	0,4	rough	intermediate	1,6
110	556903,18	39726002,28	1779,67	5% W	2,33	3,5	shrubland				smooth	intermediate	5,4
111	551325,95	3989613,15	1826,16	na	1,41	5,8	shrubland	Silt Loam	24	6	smooth	intermediate	2,0
112	511549,84	3946350,77	1626.16	0		13,2		~~Sand~~	93	0			
113	546654,27	3982847,18	1829,30	5% W	1,84	8,4	grassland	Sandy Loam	72	0	rough	intermediate	3,4
114	512593,71	3995011,71	1709.43	<2% N		1,9		Silt Loam	31	0,3			
117	530975,63	3990557,88	6241,00	0	0,76	6,9	grassland	Silt	19	6,2	smooth	intermediate	1,6
120	503481,12	3988878,78	5558,23	0	0,89	7,2	grassland	Sandy Loam	55	0,1	rough	intermediate	1,6
Kachina Met St.	521773,50	3942881,30	1589,44	0	2,38	3,8	shrubland	Silt Loam	31	0,1	**rough**	intermediate	5,7
KFarm1	527318,85	3980681,23	1758,43	0	2,50	8,7	grassland	Silt Loam	41	0,3	rough	rough	6,2
Navajo Farm			0,00		1,43		grassland				rough	intermediate	2,1
Navajo Farm			0,00		0,55		grassland				smooth	intermediate	1,6
Site #	Easting	Northing	Altitude (m)	Aspect	hRMS	SoilMoist%	Vegetation	Soil Texture	% Sand	% Clay	Raleigh Criterion	Peake&Oliver	Lc

APPENDIX G. ASAR METADATA STRUCTURE, METADATA FILE HEADER AND MAP PROJECTION

6.2.1 ASA_APG_1P: ASAR Alternating Polarization Ellipsoid Geocoded Image

Table 6.4

ASA_APG_1P

ASAR Alternating Polarization Ellipsoid Geocoded Image

File Structure

Data Sets 14

MPH 6.6.1.	ENVISAT-1 MPH
SPH 6.6.11.	ASAR Image Products SPH
MDS1 SQ ADS 6.6.16.	SQ ADSRs
MDS2 SQ ADS 6.6.16.	SQ ADSRs
MAIN PROCESSING PARAMS ADS 6.6.12.	Main Processing parameters
DOP CENTROID COEFFS ADS 6.6.8.	Doppler Centroid parameters
SR GR ADS 6.6.17.	Slant Range to Ground Range conversion parameters
CHIRP PARAMS ADS 6.6.7.	Chirp parameters
MDS1 ANTENNA ELEV PATT ADS 6.6.6.	Antenna Elevation patterns(s)
MDS2 ANTENNA ELEV PATT ADS 6.6.6.	Antenna Elevation patterns(s)
GEOLOCATION GRID ADS 6.6.9.	Geolocation Grid ADSRs
MAP PROJECTION GADS 6.6.13.	Map Projection parameters
MDS1 6.6.10.	Measurement Data Set 5
MDS2 6.6.10.	Measurement Data Set 5

Format Version 114.0

Name	Value	Type	Unit
PRODUCT	ASA_APG_1PNDPA20040508_172050_000000162026_00370_11446_0011.N1	null	Product name
PRODUCT_TYPE	ASA_APG_1P	null	Product type
SPH_DESCRIPTOR	AP Mode Geocoded Image	null	Description
MISSION	ENVISAT	null	Satellite mission
PROC_TIME	03-JUN-2004 07:29:44.000000	utc	Processed time
Processing system identifier	ASAR/3.08	null	Processing system identifier
CYCLE	26	null	Cycle
REL_ORBIT	370	null	Track
ABS_ORBIT	11446	null	Orbit
STATE_VECTOR_TIME	08-MAY-2004 17:21:00.000000	utc	Time of orbit state vector
VECTOR_SOURCE	FR	null	State vector source
NUM_SLICES	1	null	Number of slices
first_line_time	08-MAY-2004 17:20:50.878385	utc	First zero doppler azimuth time
last_line_time	08-MAY-2004 17:21:06.885083	utc	Last zero doppler azimuth time
first_near_lat	3.655.612.564.086.910	deg	
first_near_long	-11.104.022.979.736.300	deg	
first_far_lat	3.655.231.475.830.070	deg	
first_far_long	-11.004.521.179.199.200	deg	
last_near_lat	3.550.026.321.411.130	deg	
last_near_long	-1.110.396.957.397.460	deg	
last_far_lat	354.965.934.753.418	deg	
last_far_long	-11.005.786.895.751.900	deg	
SWATH	IS6	null	Swath name
PASS	DESCENDING	null	ASCENDING or DESCENDING
SAMPLE_TYPE	DETECTED	null	DETECTED or COMPLEX
mds1_tx_rx_polar	HV	null	Polarization
mds2_tx_rx_polar	HH	null	Polarization
ALGORITHM	SPECAN	null	Processing algorithm
AZIMUTH_LOOKS	2	null	
RANGE_LOOKS	3	null	
RANGE_SPACING	12. Mai	m	Range sample spacing
AZIMUTH_SPACING	12. Mai	m	Azimuth sample spacing
pulse_repetition_frequency	1.705.227.294.921.870	Hz	PRF
radar_frequency	5.331.004.416	MHz	Radar frequency
LINE_TIME_INTERVAL	0.0	s	
total_size	267472375	Mb	Total product size
num_output_lines	9370		
num_samples_per_line	7128		
srgr_flag	1	flag	SRGR applied
avg_scene_height	0.0	m	Average ccene height ellipsoid
map_projection	UTM Zone 12	null	Map projection applied
is_terrain_corrected	0	flag	orthorectification applied
dem		null	Digital Elevation Model used
geo_ref_system	WGS-84	null	geographic reference system
lat_pixel_res	0.0	deg	pixel resolution in geocoded image
lon_pixel_res	0.0	deg	pixel resolution in geocoded image
slant_range_to_first_pixel	1.039.775.728.241.870	m	Slant range to 1st data sample
ant_elev_corr_flag	1	flag	Antenna elevation applied
range_spread_comp_flag	1	flag	range spread compensation applied
replica_power_corr_flag	0	flag	Replica pulse power correction applied
abs_calibration_flag	0	flag	Product calibrated
calibration_factor	944.449.875		Calibration constant
range_sampling_rate	1.920.768	MHz	Range Sampling Rate
multilook_flag	0	flag	Product multilooked
external_calibration_file	ASA_XCA_AXVIEC20040406_160451_20030211_000000_20041231_000000	null	External calibration file used
orbit_state_vector_file	AUX_FRO_AXVPDS20040511_000526_20040507_221000_20040510_005000	null	Orbit file used
time	08-MAY-2004 17:20:50.878386	utc	
x_pos	-1420989.81		
y_pos	-5671853.08		
z_pos	4131368.71		
x_vel	-276.193.637		
y_vel	-368.186.393		
z_vel	-598.775.316		
time	08-MAY-2004 17:20:54.080026	utc	
x_pos	-1429827.4		
y_pos	-5683607.61		
z_pos	4112175.08		
x_vel	-275.872.218		
y_vel	-366.094.392		
z_vel	-60.021.113		
time	08-MAY-2004 17:20:57.281667	utc	
x_pos	-1438654.64		
y_pos	-5695295.09		
z_pos	4092935.58		
x_vel	-275.546.779		
y_vel	-363.998.485		
z_vel	-601.640.285		
time	08-MAY-2004 17:21:00.483307	utc	
x_pos	-1447471.39		
y_pos	-5706915.41		
z_pos	4073650.43		
x_vel	-275.217.303		
y_vel	-361.898.689		
z_vel	-603.062.745		
time	08-MAY-2004 17:21:03.684947	utc	
x_pos	-1456277.53		
y_pos	-5718468.44		
z_pos	4054319.85		
x_vel	-274.883.792		
y_vel	-359.795.027		
z_vel	-604.478.462		
zero_doppler_time	08-MAY-2004 17:20:50.878386	utc	
ground_range_origin	0.0	m	
srgr_coef	9.802.743.125		
srgr_coef	0.6319937705993652		
srgr_coef	3,67E+09		
srgr_coef	-2,39E+02		
srgr_coef	8,91E-05		

Name	Value	Type
map_descriptor	UNIVERSAL_TRANSVERSE_MERCATOR	ascii
samples	7128	*
lines	9370	*
sample_spacing	12. Mai	m
line_spacing	12. Mai	m
orientation	0.0	deg
heading	-16.642.825	deg
ellipsoid_name	WGS84	ascii
semi_major	6378137.0	m
semi_minor	6356752.0	m
shift_dx	0.0	m
shift_dy	0.0	m
shift_dz	0.0	m
avg_height	18.466.307	*
projection_description	UTM	ascii
utm_descriptor	UNIVERSAL_TRANSVERSE_MERCATOR	ascii
utm_zone	12	ascii
utm_origin_easting	500000.0	m
utm_origin_northing	0.0	m
utm_center_long	-111000000	(1e-6) degrees
utm_center_lat	0	(1e-6) degrees
utm_para1	-112.5	deg
utm_para2	-109.5	deg
utm_scale	0.9996	*
ups_descriptor	UNIVERSAL_POLAR_STEREOGRAPHIC	ascii
ups_center_long	0	(1e-6) degrees
ups_center_lat	0	(1e-6) degrees
ups_scale	0.0	*
nsp_descriptor		ascii
origin_easting	0.0	m
origin_northing	0.0	m
center_long	0	(1e-6) degrees
center_lat	0	(1e-6) degrees
ASAR_Map_GADS.sd/standard_parallel_parameters.para1	0.0	deg
ASAR_Map_GADS.sd/standard_parallel_parameters.para2	0.0	deg
ASAR_Map_GADS.sd/standard_parallel_parameters.para3	0.0	deg
ASAR_Map_GADS.sd/standard_parallel_parameters.para4	0.0	deg
ASAR_Map_GADS.sd/central_meridian_parameters.central_m1	0.0	deg
ASAR_Map_GADS.sd/central_meridian_parameters.central_m2	0.0	deg
ASAR_Map_GADS.sd/central_meridian_parameters.central_m3	0.0	deg
ASAR_Map_GADS.sd/position_northings_eastings.tl_northing	4045641.0	m
ASAR_Map_GADS.sd/position_northings_eastings.tl_easting	496393.38	m
ASAR_Map_GADS.sd/position_northings_eastings.tr_northing	4045641.0	m
ASAR_Map_GADS.sd/position_northings_eastings.tr_easting	585480.9	m
ASAR_Map_GADS.sd/position_northings_eastings.br_northing	3928528.5	m
ASAR_Map_GADS.sd/position_northings_eastings.br_easting	585480.9	m
ASAR_Map_GADS.sd/position_northings_eastings.bl_northing	3928528.5	m
ASAR_Map_GADS.sd/position_northings_eastings.bl_easting	496393.38	m
ASAR_Map_GADS.sd/position_lat_long.tl_lat	36556186	(1e-6) degrees
ASAR_Map_GADS.sd/position_lat_long.tl_long	-111040302	(1e-6) degrees
ASAR_Map_GADS.sd/position_lat_long.tr_lat	36552367	(1e-6) degrees
ASAR_Map_GADS.sd/position_lat_long.tr_long	-110044865	(1e-6) degrees
ASAR_Map_GADS.sd/position_lat_long.br_lat	35496637	(1e-6) degrees
ASAR_Map_GADS.sd/position_lat_long.br_long	-110057525	(1e-6) degrees
ASAR_Map_GADS.sd/position_lat_long.bl_lat	35500311	(1e-6) degrees
ASAR_Map_GADS.sd/position_lat_long.bl_long	-111039768	(1e-6) degrees
image_to_map_coefs	496380.88,0.0,12.499999,0.0,4045653.5,-12.5,0.0,0.0	*
map_to_image_coefs	323652.28,-9.752071E-19,-0.08,0.0,-39710.47,0.08,7.4176263E-19,0.0	*

APPENDIX H. RAW IMAGE DATA

Band 1
HV

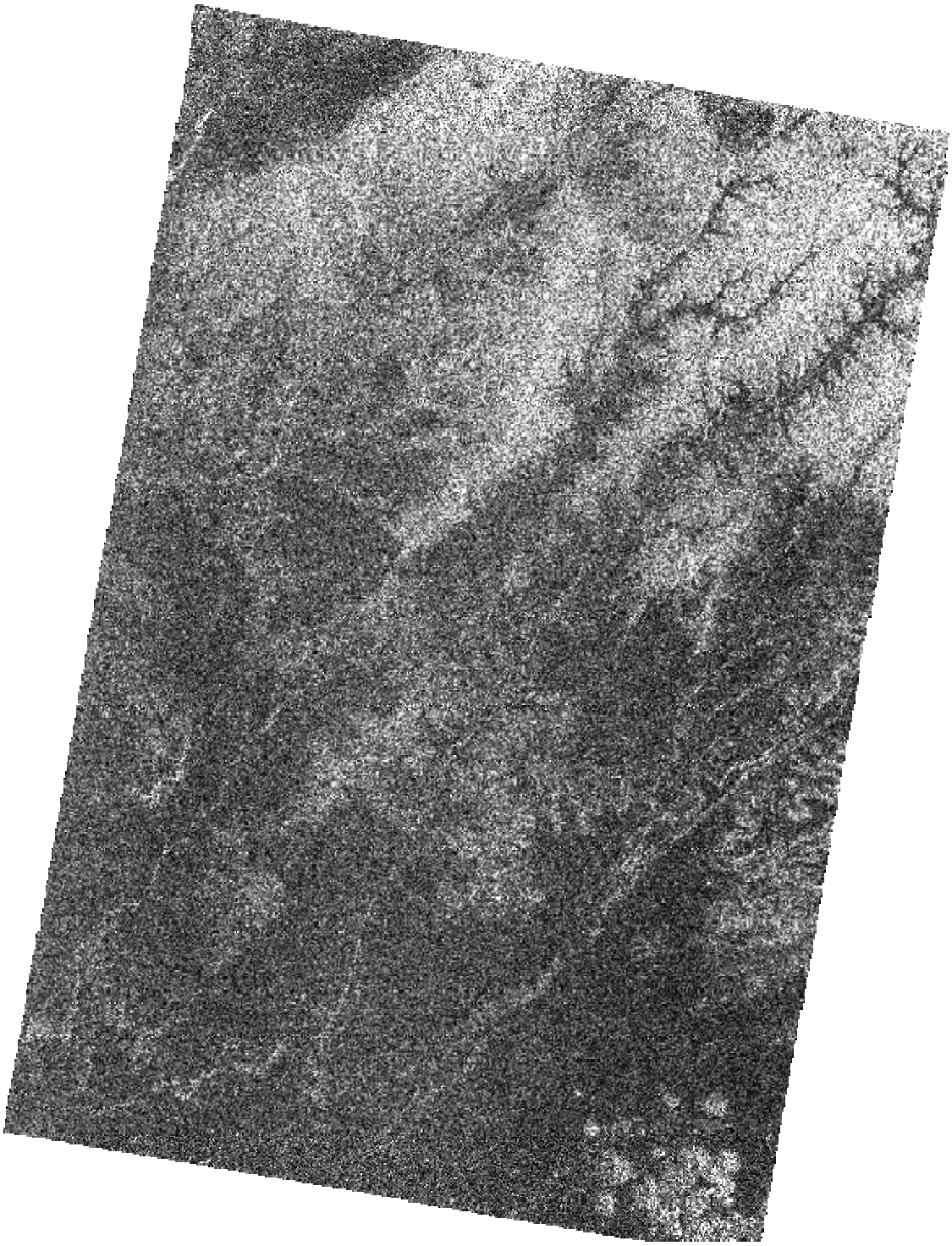

Band 2
HH

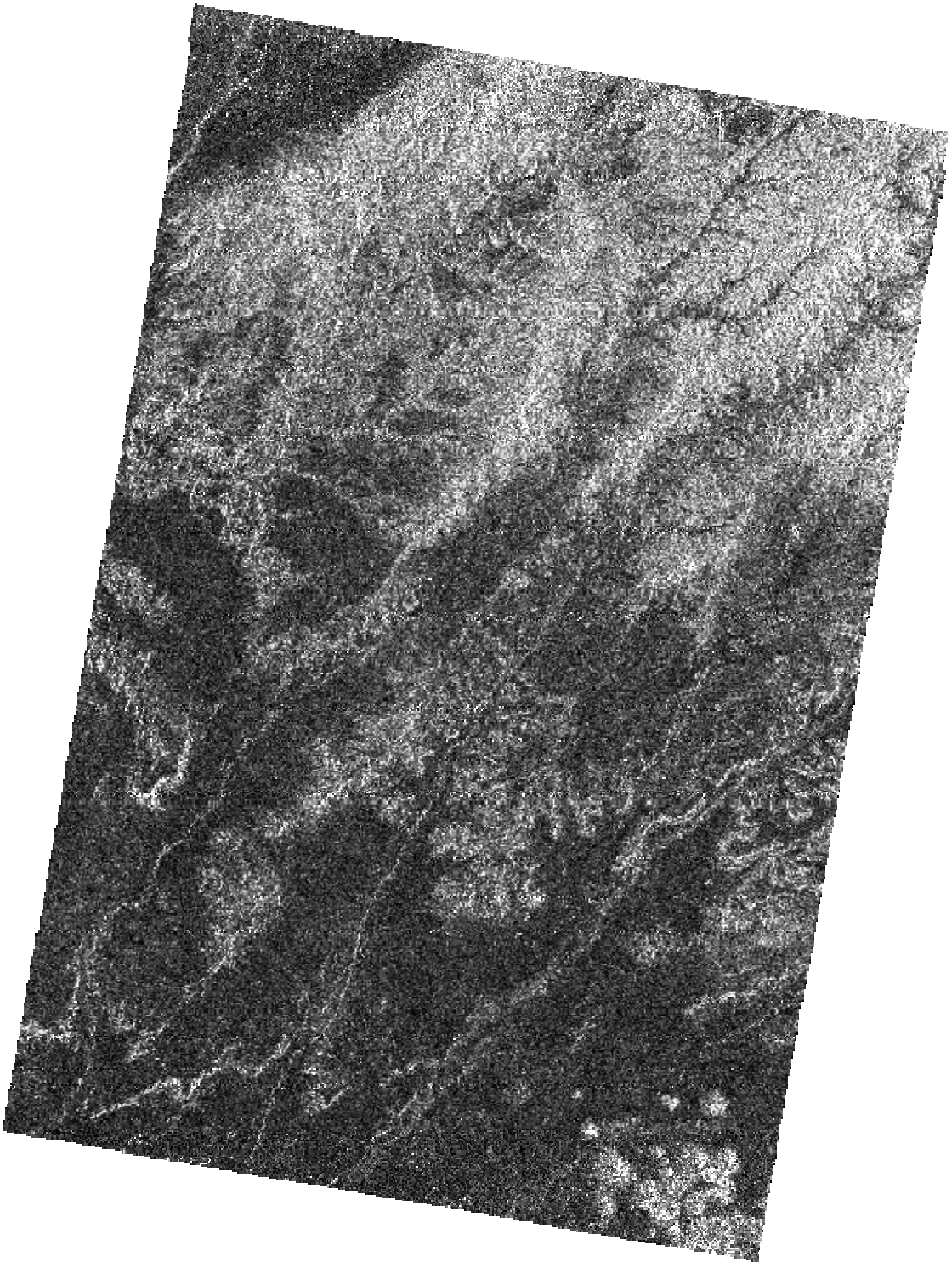

APPENDIX I. IMAGE DATA AFTER SPECKLE FILTERING AND DB CONVERSION

Band 1 HV

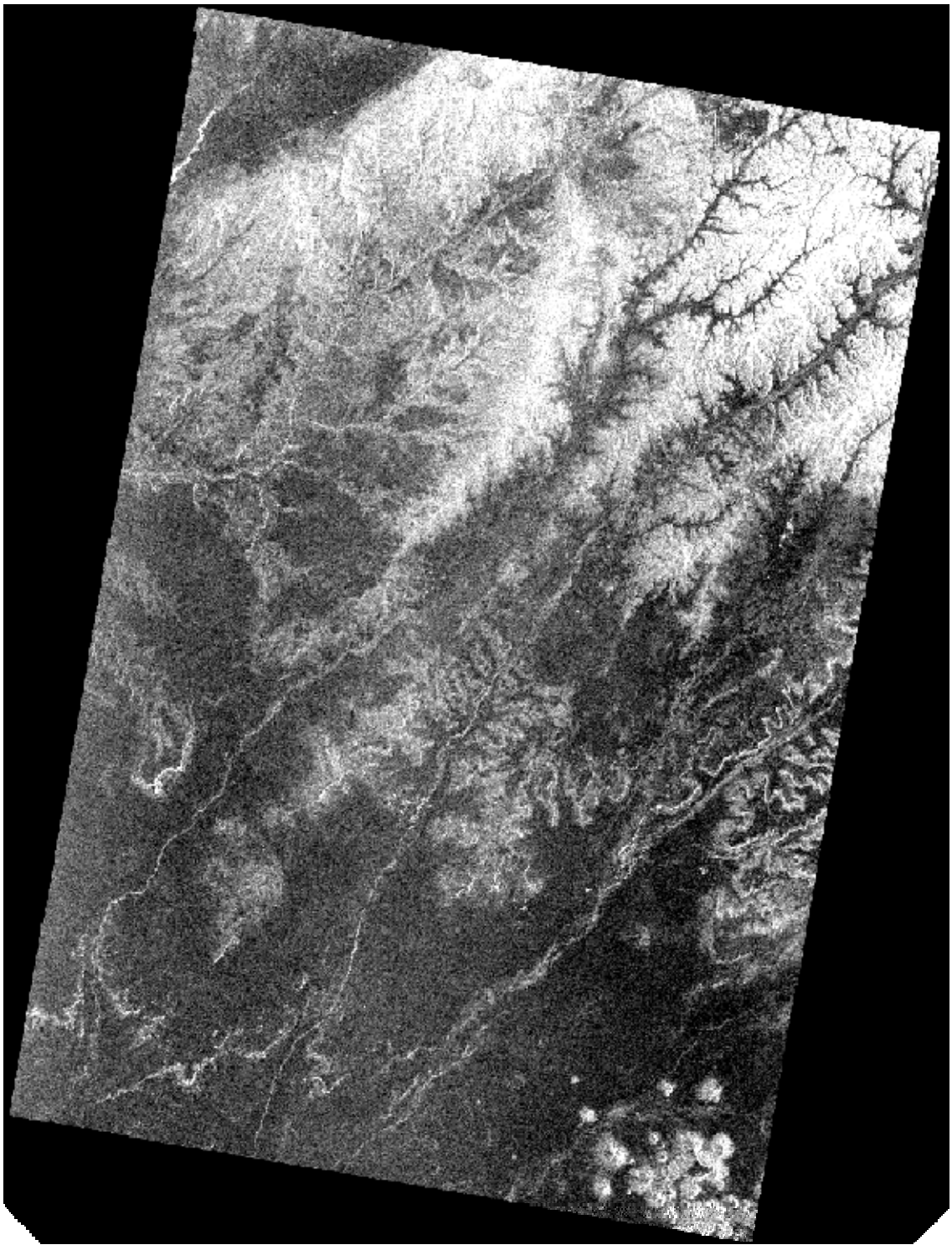

Band 2 HH

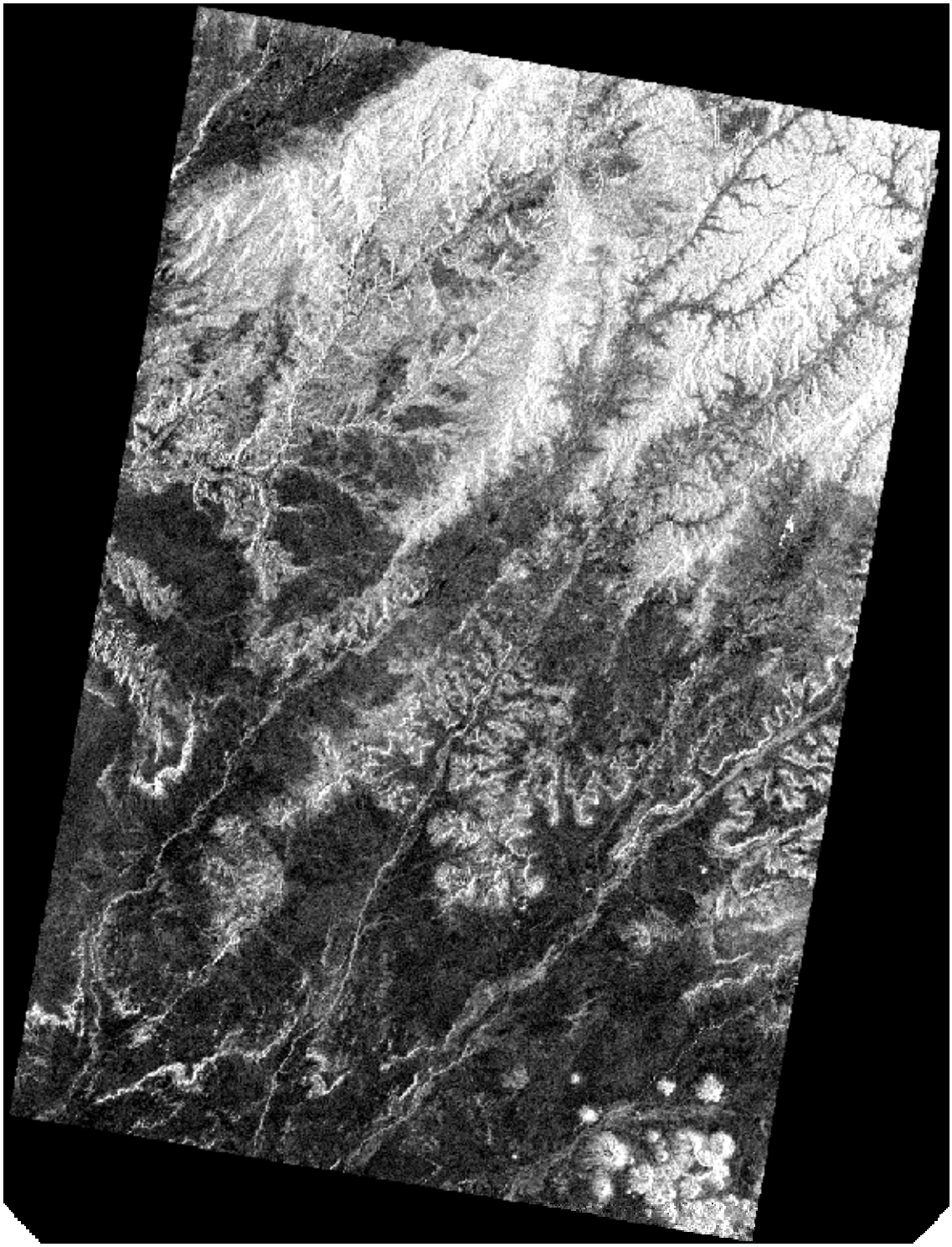

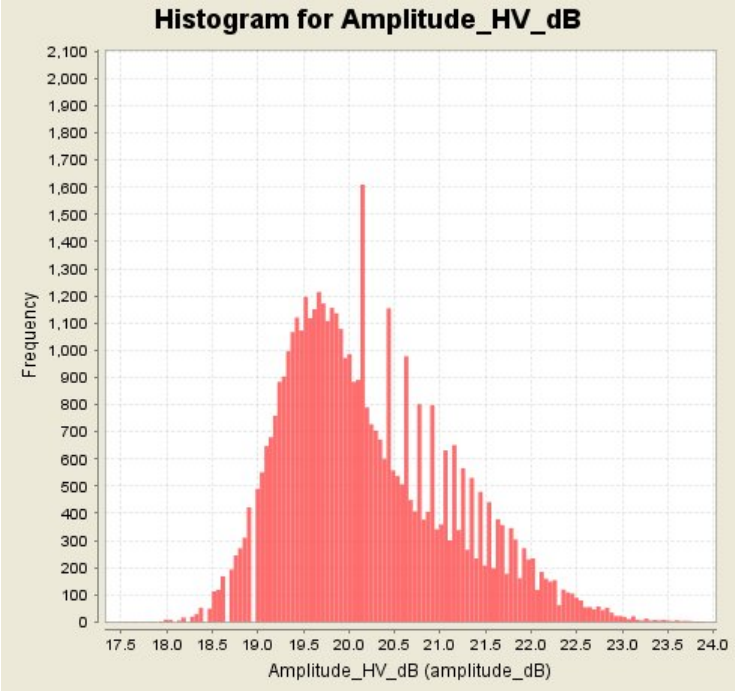
Histogram for Amplitude_HV_dB
Frequency
2,100
2,000
1,900
1,800
1,700
1,600
1,500
1,400
1,300
1,200
1,100
1,000
900
800
700
600
500
400
300
200
100
0
17.5 18.0 18.5 19.0 19.5 20.0 20.5 21.0 21.5 22.0 22.5 23.0 23.5 24.0
Amplitude_HV_dB (amplitude_dB)

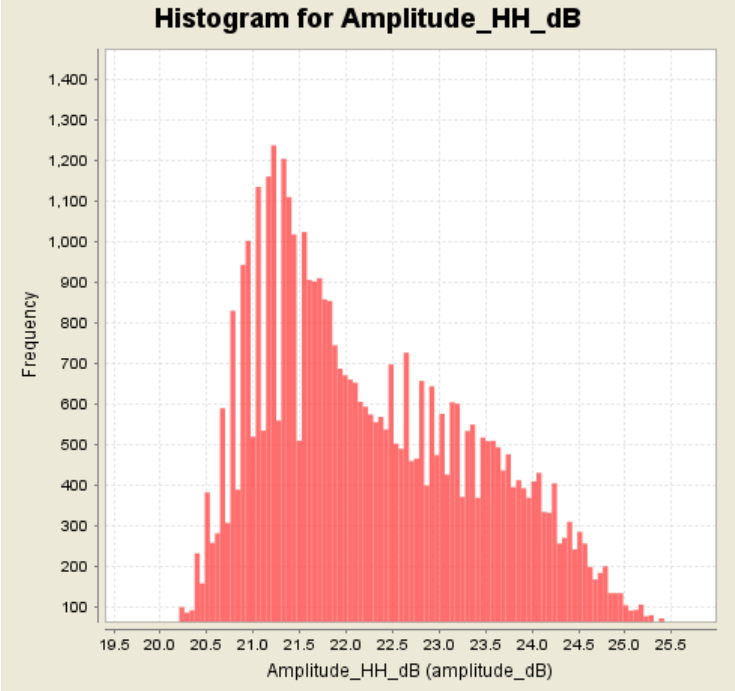
Histogram for Amplitude_HH_dB
Frequency
1,400
1,300
1,200
1,100
1,000
900
800
700
600
500
400
300
200
100
19.5 20.0 20.5 21.0 21.5 22.0 22.5 23.0 23.5 24.0 24.5 25.0 25.5
Amplitude_HH_dB (amplitude_dB)

Band: Amplitude_HV_dB
Only ROI pixels considered: No
Number of pixels total: 66789360
Number of considered pixels: 66789360
Ratio of considered pixels: 100.0 %

Minimum: 0.0 amplitude_dB
Maximum: 25.563024520874023 amplitude_dB

Mean: 14.628729211880351 amplitude_dB
Std-Dev: 9.066932969802487 amplitude_dB
Coefficient of Variation: 0.6268496521098054 amplitude_dB

Band: Amplitude_HH_dB
Only ROI pixels considered: No
Number of pixels total: 66789360
Number of considered pixels: 66789360
Ratio of considered pixels: 100.0 %

Minimum: 0.0 amplitude_dB
Maximum: 30.718820571899414 amplitude_dB

Mean: 16.185127945503847 amplitude_dB
Std-Dev: 10.053462488495423 amplitude_dB
Coefficient of Variation: 0.6322963995506239 amplitude_dB

APPENDIX J. BACKSCATTER DIFFERENCE IMAGE AND Z-INDEX MAP

Backscatter Image

$\Delta\sigma^0 = \sigma^0 HH - \sigma^0 HV$

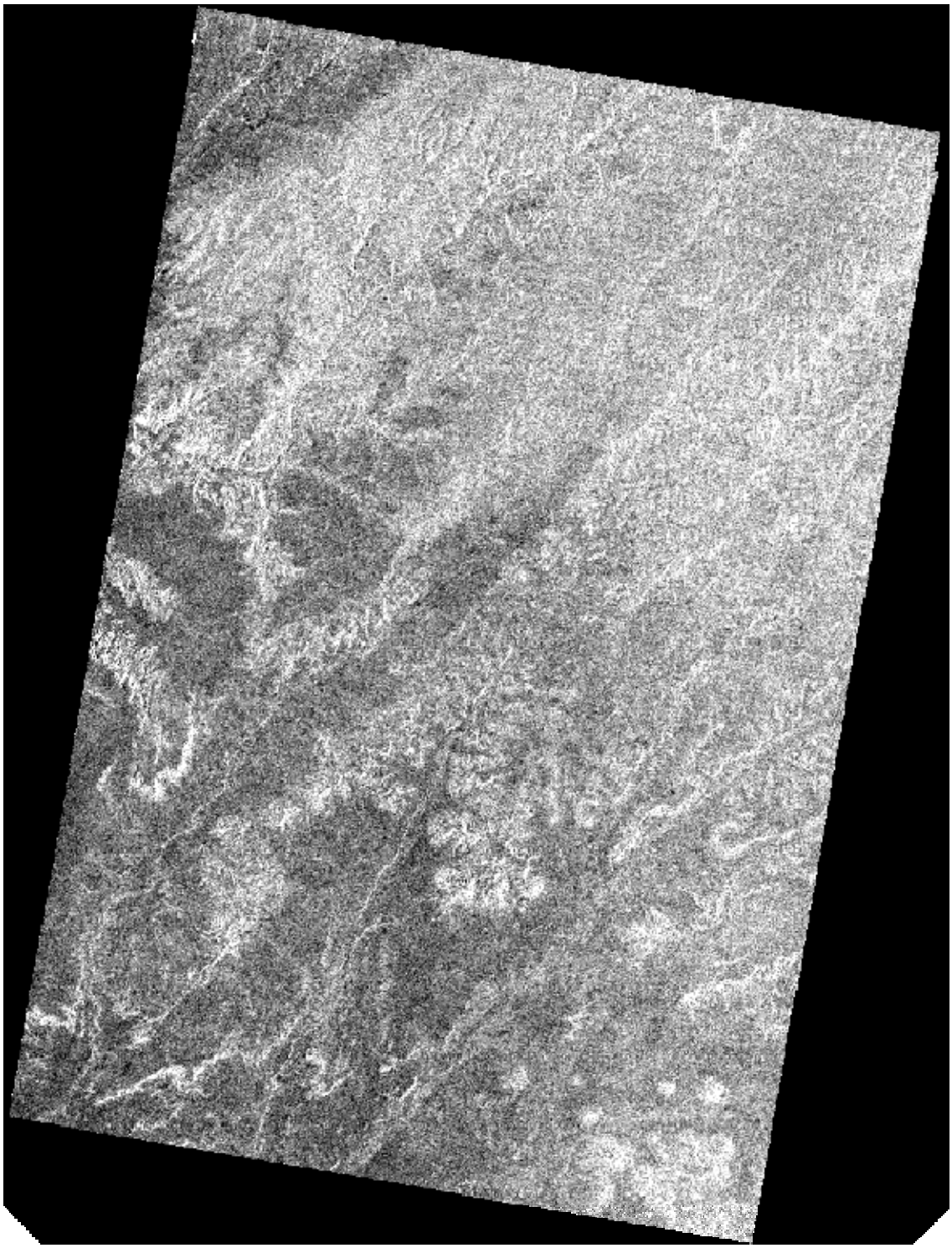

Z-index Map $\frac{\left(0.618 + 0.09 * \Delta\sigma^0\right)}{\left(1 - 0.138 * \Delta\sigma^0\right)}$

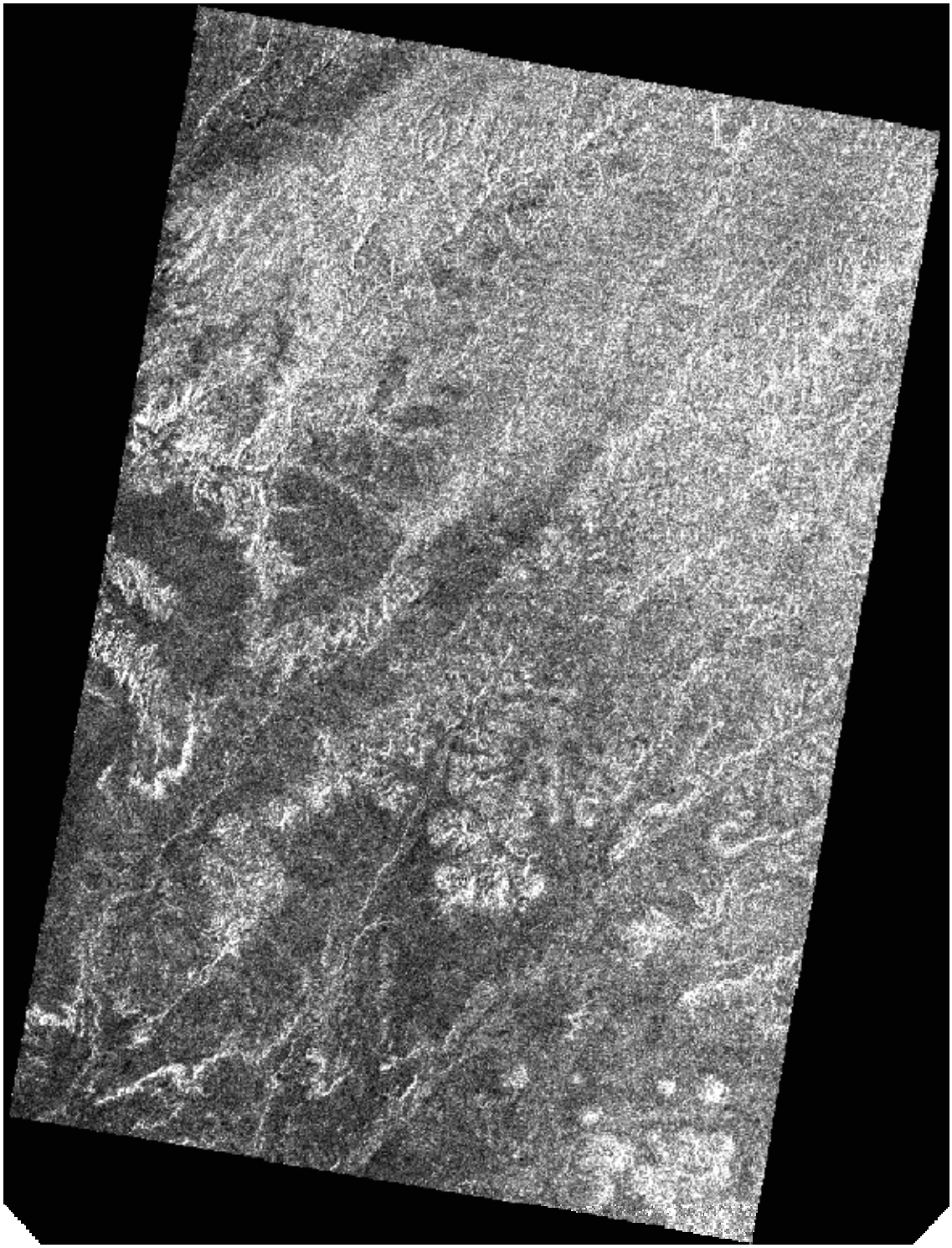

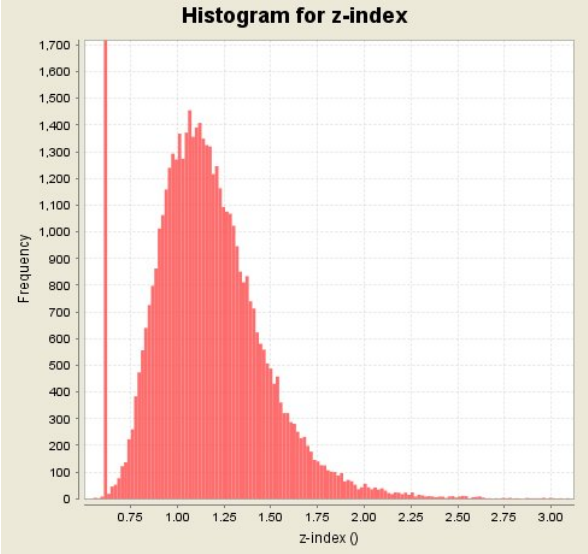

Band: HH-HV
Only ROI pixels considered: No
Number of pixels total: 66789360
Number of considered pixels: 66789360
Ratio of considered pixels: 100.0 %

Minimum: -23.24282455444336 1
Maximum: 22.648178100585938 1

Mean: 1.5563987336234886 1
Std-Dev: 1.1502677346896022 1
Coefficient of Variation: 1.3125757426850428 1

Z-index
(0.618+ (0.09* 'HH-HV'))/ (1- (0.138* 'HH-HV'))

Band: Z-index
Only ROI pixels considered: No
Number of pixels total: 66789360
Number of considered pixels: 66789360
Ratio of considered pixels: 100.0 %

Minimum: -1057.1448974609375 1
Maximum: 1089.78564453125 1

Mean: 1.0345145778675149 1
Std-Dev: 0.46303314749511487 1
Coefficient of Variation: 182.41845276214084 1

APPENDIX K. NUMERICAL SOLUTIONS TO THE IEM DERIVATIVE EQUATION

Z-index/hRMS	0,10	0,20	0,30	0,40	0,50	0,60	0,70	0,80	0,90	1,00	1,10	1,20	1,30	1,40	1,50	1,60	1,70	1,80	1,90	2,00	2,10	2,20	2,30
-5,00	-25	-22	-20	-18	-16	-15	-13	-12	-12	-11	-11	-11	-11	-12	-12	-13	-14	-15	-16	-18	-19	-21	-22
-4,50	-25	-22	-20	-18	-16	-15	-13	-12	-12	-11	-11	-11	-11	-12	-12	-13	-14	-15	-16	-18	-19	-21	-22
-4,00	-25	-22	-20	-18	-16	-15	-13	-12	-12	-11	-11	-11	-11	-12	-12	-13	-14	-15	-17	-18	-19	-21	-23
-3,50	-25	-22	-20	-18	-16	-15	-13	-12	-12	-11	-11	-11	-11	-12	-13	-13	-14	-15	-17	-18	-20	-21	-23
-3,00	-25	-22	-20	-18	-16	-15	-13	-12	-12	-11	-11	-11	-11	-12	-13	-13	-14	-16	-17	-18	-20	-22	-24
-2,50	-25	-22	-20	-18	-16	-14	-13	-12	-12	-11	-11	-11	-11	-12	-13	-13	-14	-16	-17	-19	-20	-22	-24
-2,00	-25	-22	-20	-18	-16	-14	-13	-12	-12	-11	-11	-11	-11	-12	-13	-14	-15	-16	-17	-19	-21	-23	-26
-1,50	-25	-22	-20	-18	-16	-14	-13	-12	-12	-11	-11	-11	-11	-12	-13	-14	-15	-16	-18	-20	-22	-25	-28
-1,00	-25	-22	-20	-18	-16	-14	-13	-12	-11	-11	-11	-11	-11	-12	-13	-14	-16	-17	-20	-22	-25	-29	-33
-0,50	-25	-22	-20	-18	-16	-14	-13	-12	-11	-11	-10	-11	-11	-12	-14	-15	-18	-21	-25	-30	-35	-42	-50
0,01	-25	-24	-24	-25	-23	-18	-7	10	30	47	46	8	-101	-325	-728	-1389	-2416	-3938	-6122	-9164	-13306	-18833	-26080
0,50	-25	-22	-20	-18	-16	-15	-14	-13	-13	-12	-12	-12	-12	-12	-12	-12	-12	-12	-12	-11	-11	-11	-11
1,00	-25	-22	-20	-18	-16	-15	-14	-13	-12	-12	-12	-12	-12	-12	-12	-12	-13	-13	-13	-13	-13	-13	-13
1,50	-25	-22	-20	-18	-16	-15	-14	-13	-12	-12	-12	-12	-12	-12	-12	-12	-13	-13	-14	-14	-14	-15	-15
2,00	-25	-22	-20	-18	-16	-15	-14	-13	-12	-12	-11	-11	-12	-12	-12	-13	-13	-14	-14	-15	-15	-16	-16
2,50	-25	-22	-20	-18	-16	-15	-14	-13	-12	-12	-11	-11	-12	-12	-12	-13	-13	-14	-14	-15	-16	-16	-17
3,00	-25	-22	-20	-18	-16	-15	-14	-13	-12	-12	-11	-11	-12	-12	-12	-13	-13	-14	-15	-16	-16	-17	-17
3,50	-25	-22	-20	-18	-16	-15	-14	-13	-12	-12	-11	-11	-12	-12	-12	-13	-13	-14	-15	-16	-16	-17	-18
4,00	-25	-22	-20	-18	-16	-15	-14	-13	-12	-12	-11	-11	-12	-12	-12	-13	-13	-14	-15	-16	-16	-17	-18
4,50	-25	-22	-20	-18	-16	-15	-13	-13	-12	-12	-11	-11	-12	-12	-12	-13	-13	-14	-15	-16	-17	-17	-18
5,00	-25	-22	-20	-18	-16	-15	-13	-13	-12	-12	-11	-11	-12	-12	-12	-13	-14	-14	-15	-16	-17	-17	-18
5,50	-25	-22	-20	-18	-16	-15	-13	-13	-12	-12	-11	-11	-12	-12	-12	-13	-14	-14	-15	-16	-17	-18	-18
6,00	-25	-22	-20	-18	-16	-15	-13	-13	-12	-12	-11	-11	-12	-12	-12	-13	-14	-14	-15	-16	-17	-18	-19
6,50	-25	-22	-20	-18	-16	-15	-13	-13	-12	-12	-11	-11	-12	-12	-12	-13	-14	-14	-15	-16	-17	-18	-19
7,00	-25	-22	-20	-18	-16	-15	-13	-13	-12	-12	-11	-11	-12	-12	-12	-13	-14	-14	-15	-16	-17	-18	-19
7,50	-25	-22	-20	-18	-16	-15	-13	-13	-12	-12	-11	-11	-12	-12	-12	-13	-14	-14	-15	-16	-17	-18	-19

Numerical Solution of hRMS
hRMS Classification LUT
1

Z-index/hRMS	2,40	2,50	2,60	2,70	2,80	2,90	3,00	3,10	3,20	3,30	3,40	3,50	3,60	3,70	3,80	3,90
-5,00	-24	-26	-27	-29	-31	-33	-35	-38	-40	-42	-44	-46	-49	-51	-53	-56
-4,50	-24	-26	-28	-30	-32	-34	-36	-39	-41	-43	-46	-48	-51	-54	-56	-59
-4,00	-25	-26	-28	-31	-33	-35	-38	-40	-43	-45	-48	-51	-54	-57	-60	-64
-3,50	-25	-27	-29	-32	-34	-36	-39	-42	-45	-48	-51	-54	-58	-62	-65	-70
-3,00	-26	-28	-30	-33	-35	-38	-41	-44	-48	-51	-55	-59	-63	-68	-73	-78
-2,50	-27	-29	-32	-35	-38	-41	-44	-48	-52	-57	-61	-66	-71	-77	-83	-90
-2,00	-28	-31	-34	-38	-41	-45	-50	-54	-59	-65	-71	-77	-85	-92	-101	-110
-1,50	-31	-35	-38	-43	-48	-53	-59	-65	-72	-80	-89	-98	-109	-121	-133	-148
-1,00	-37	-42	-48	-55	-62	-70	-80	-91	-103	-116	-131	-148	-167	-188	-212	-238
-0,50	-60	-72	-85	-101	-120	-141	-166	-195	-228	-267	-311	-361	-418	-482	-556	-639
0,01	-35440	-47368	-62388	-81096	-104173	-132388	-166605	-207791	-257026	-315510	-384569	-465669	-560418	-670582	-798093	-945054
0,50	-12	-12	-13	-15	-17	-21	-25	-31	-39	-49	-62	-78	-98	-122	-150	-185
1,00	-13	-13	-12	-12	-11	-10	-9	-9	-8	-7	-7	-7	-7	-8	-9	-11
1,50	-15	-15	-14	-14	-13	-13	-12	-11	-9	-8	-6	-4	-2	0	2	4
2,00	-16	-16	-16	-16	-16	-15	-14	-13	-12	-11	-9	-7	-5	-2	1	4
2,50	-17	-17	-17	-17	-17	-17	-16	-15	-14	-13	-12	-10	-8	-5	-2	1
3,00	-18	-18	-18	-18	-18	-18	-18	-17	-16	-15	-14	-12	-10	-8	-5	-2
3,50	-18	-19	-19	-19	-19	-19	-19	-19	-18	-17	-16	-14	-12	-10	-8	-5
4,00	-18	-19	-20	-20	-20	-20	-20	-20	-19	-18	-17	-16	-14	-12	-10	-7
4,50	-19	-19	-20	-20	-21	-21	-21	-20	-20	-19	-18	-17	-15	-14	-11	-9
5,00	-19	-20	-20	-21	-21	-21	-21	-21	-21	-20	-19	-18	-17	-15	-13	-10
5,50	-19	-20	-21	-21	-21	-22	-22	-22	-21	-21	-20	-19	-18	-16	-14	-12
6,00	-19	-20	-21	-21	-22	-22	-22	-22	-22	-22	-21	-20	-19	-17	-15	-13
6,50	-20	-20	-21	-22	-22	-22	-23	-23	-23	-22	-21	-21	-19	-18	-16	-14
7,00	-20	-20	-21	-22	-22	-23	-23	-23	-23	-23	-22	-21	-20	-19	-17	-15
7,50	-20	-21	-21	-22	-23	-23	-23	-23	-23	-23	-23	-22	-21	-19	-18	-16

Numerical Solution of hRMS
hRMS Classification LUT
2

APPENDIX L. THE H_{RMS} AND L_C MAPS

h_{RMS}
Map

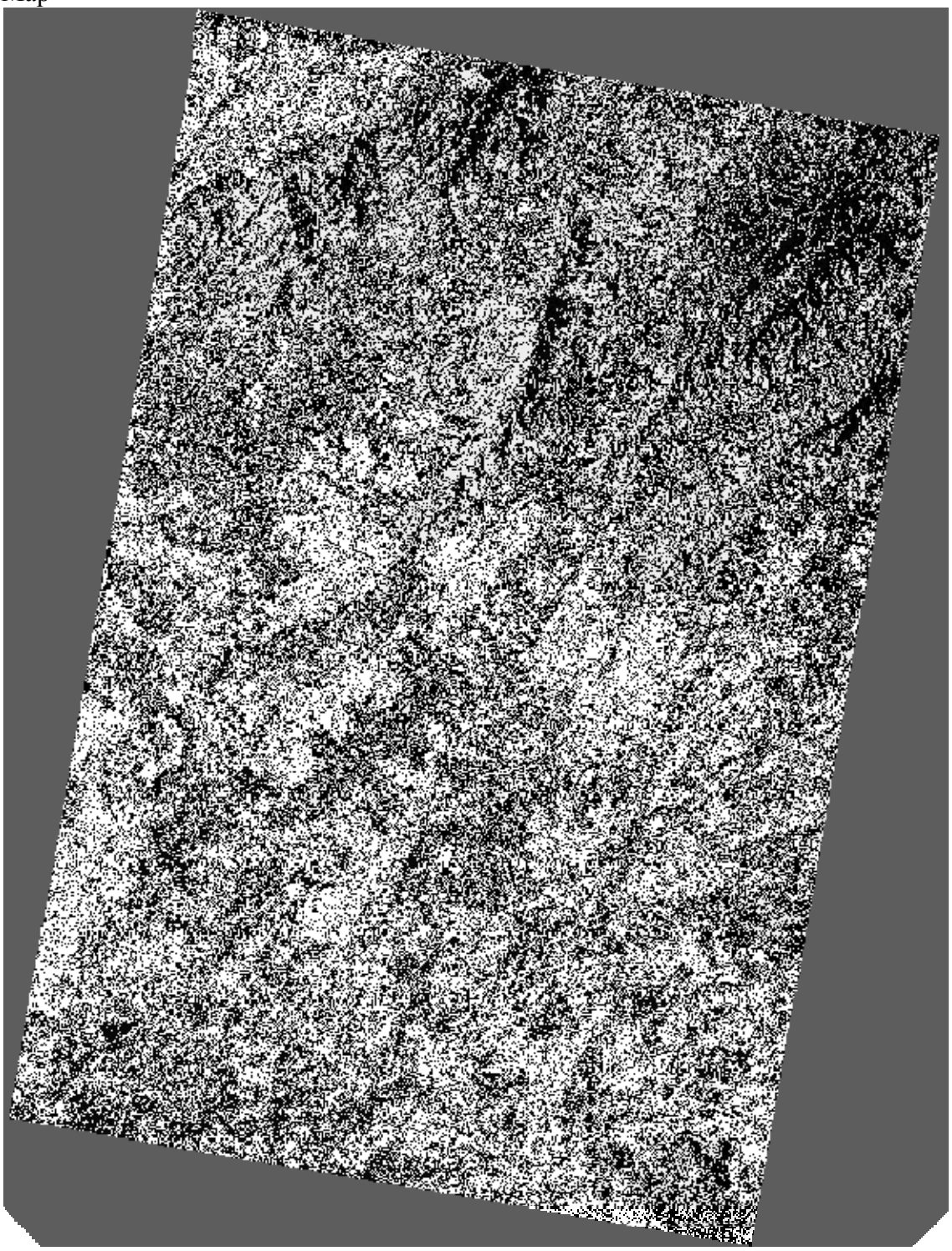

L_c
Map

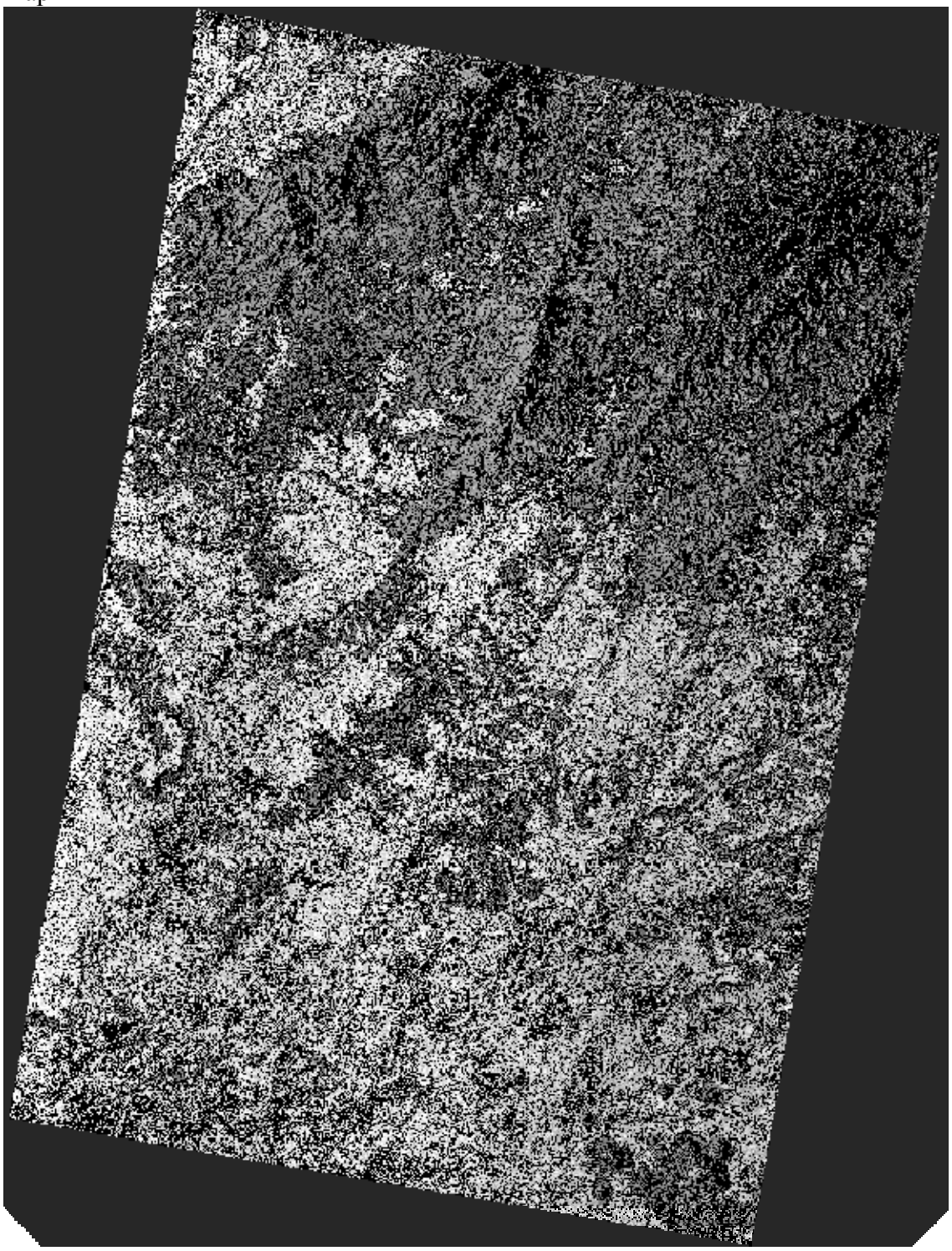

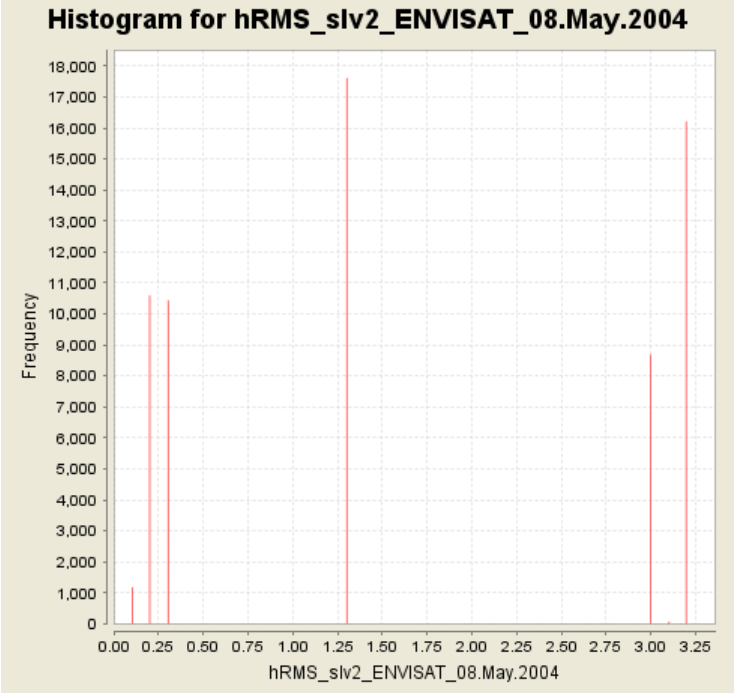
Histogram for hRMS_slv2_ENVISAT_08.May.2004
Frequency
18,000
17,000
16,000
15,000
14,000
13,000
12,000
11,000
10,000
9,000
8,000
7,000
6,000
5,000
4,000
3,000
2,000
1,000
0
0.00 0.25 0.50 0.75 1.00 1.25 1.50 1.75 2.00 2.25 2.50 2.75 3.00 3.25
hRMS_slv2_ENVISAT_08.May.2004

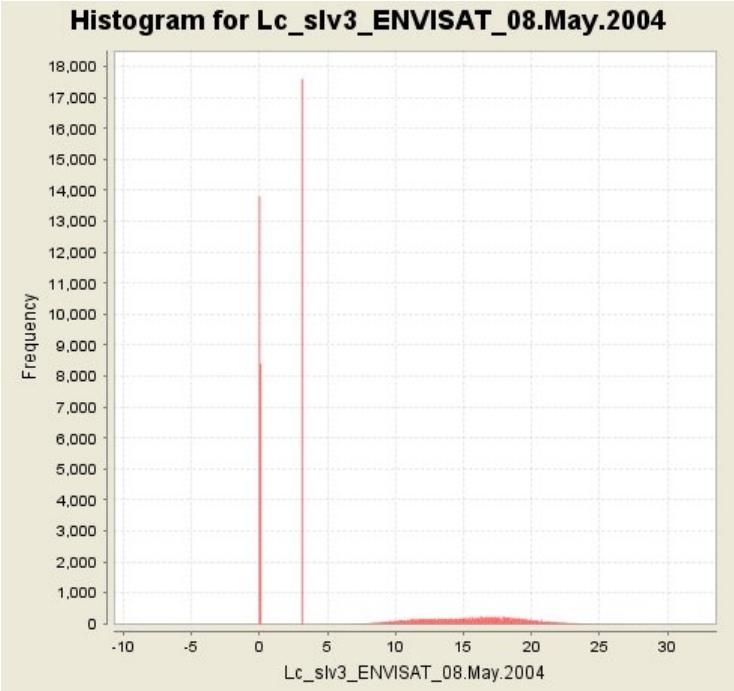
Histogram for Lc_slv3_ENVISAT_08.May.2004
Frequency
18,000
17,000
16,000
15,000
14,000
13,000
12,000
11,000
10,000
9,000
8,000
7,000
6,000
5,000
4,000
3,000
2,000
1,000
0
-10 -5 0 5 10 15 20 25 30
Lc_slv3_ENVISAT_08.May.2004

APPENDIX N. MAPS OF IMPORTED ASAR BANDS AND XY-DATA POINTS.

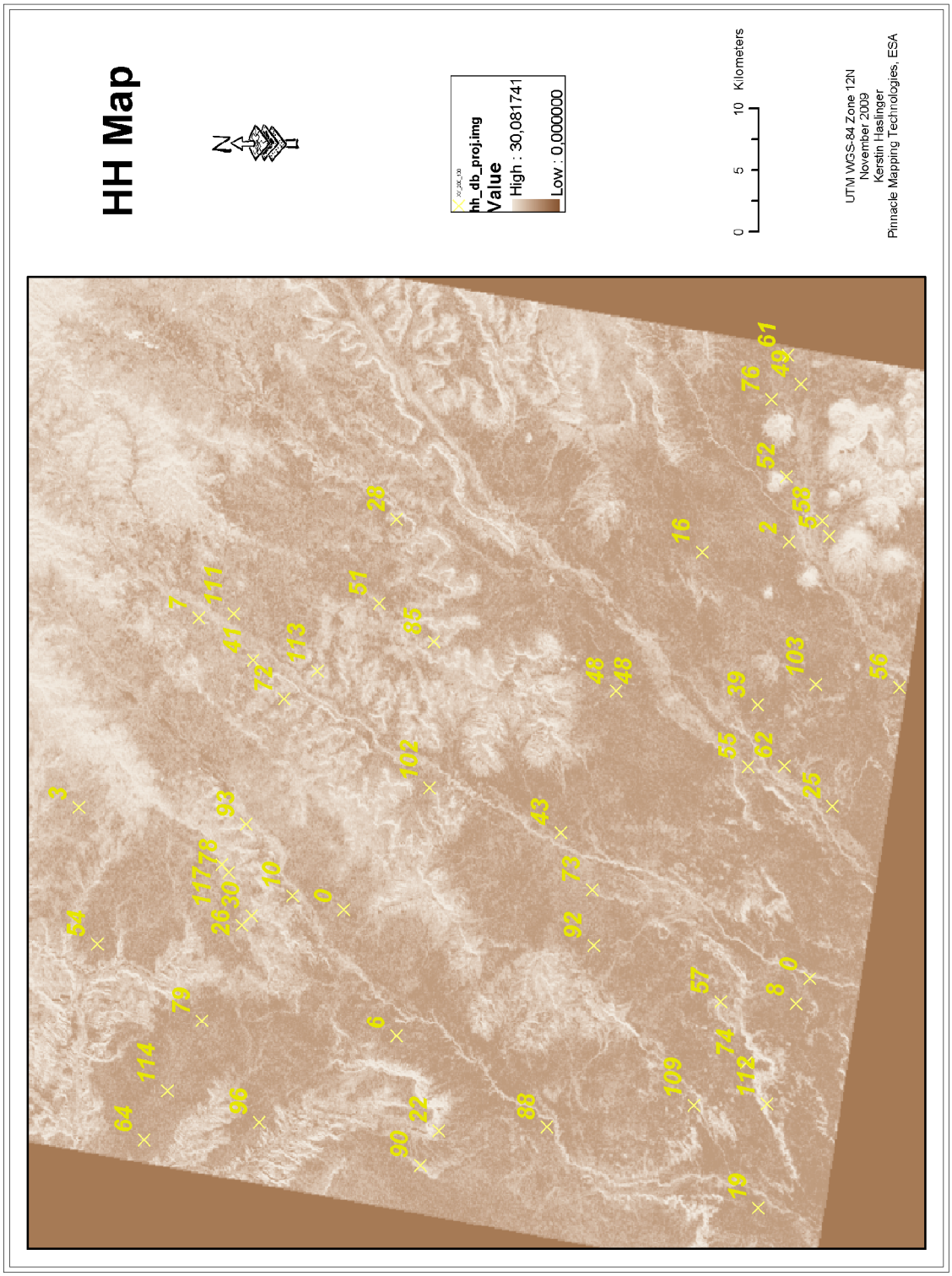


Z-Index Map
N
XY_200_100
zindex_proj.img
Value
High : 23,085211
Low : -33,217167
0 5 10 Kilometers
UTM WGS-84 Zone 12N
November 2009
Kerstin Haslinger
Pinnacle Mapping Technologies, ESA
54
3
64
114
79
7
111
117
78
26
30
93
41
96
72
10
113
0
51
28
6
90
22
102
85
88
43
92
73
48
48
109
16
57
74
55
39
19
112
62
76
61
2
52
49
8
0
103
58
5
25
56

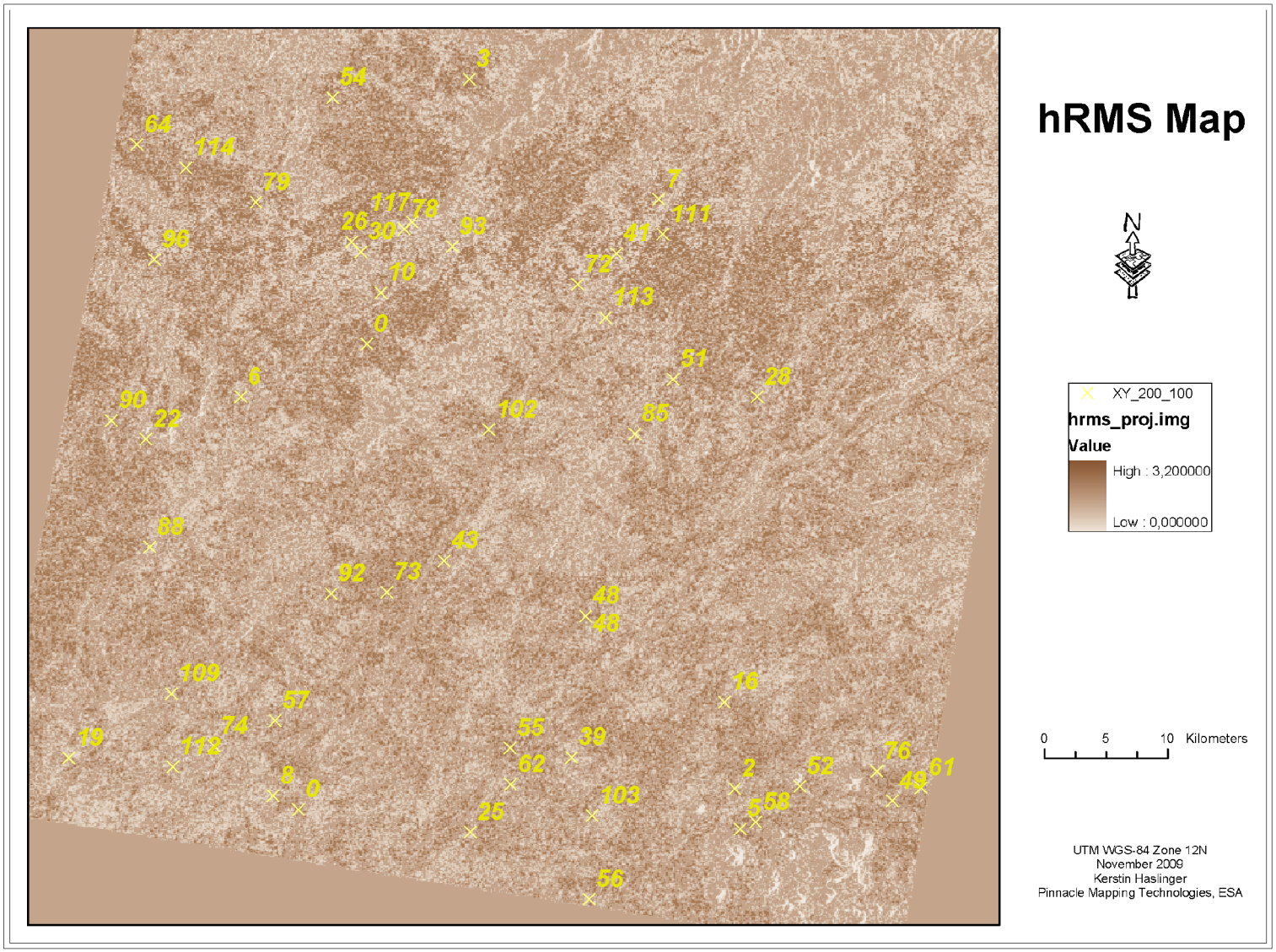
hRMS Map
N
XY_200_100
hrms_proj.img
Value
High : 3,200000
Low : 0,000000
0 5 10 Kilometers
UTM WGS-84 Zone 12N
November 2009
Kerstin Haslinger
Pinnacle Mapping Technologies, ESA
54
3
64
114
79
7
117
78
111
26
30
93
41
96
72
10
113
0
51
6
28
90
22
102
55
88
43
92
73
48
48
109
16
57
74
19
112
55
39
62
2
52
76
61
8
0
103
49
25
5
58
56

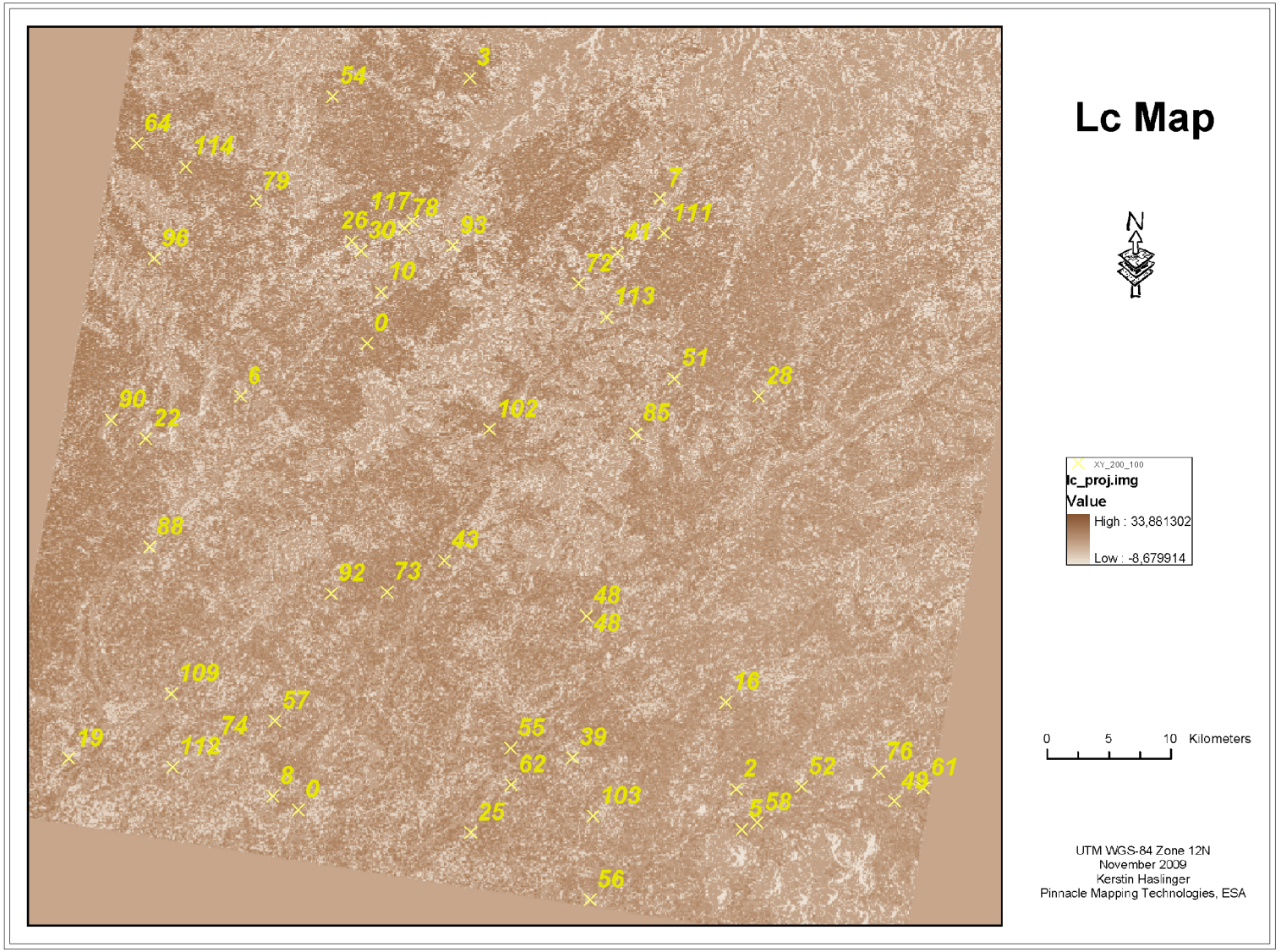
Lc Map
N
3
54
64
114
79
7
111
117
78
26
30
93
41
96
72
10
113
0
51
28
6
90
22
102
85
68
43
92
73
48
48
109
16
57
74
55
39
19
112
62
76
61
8
0
2
52
49
103
58
25
5
56
XY_200_100
lc_proj.img
Value
High : 33,861302
Low : -8,679914
0
5
10
Kilometers
UTM WGS-84 Zone 12N
November 2009
Kerstin Haslinger
Pinnacle Mapping Technologies, ESA

APPENDIX N. COMPARISON OF H_{RMS} VALUES IN VONOROI PLOTS.

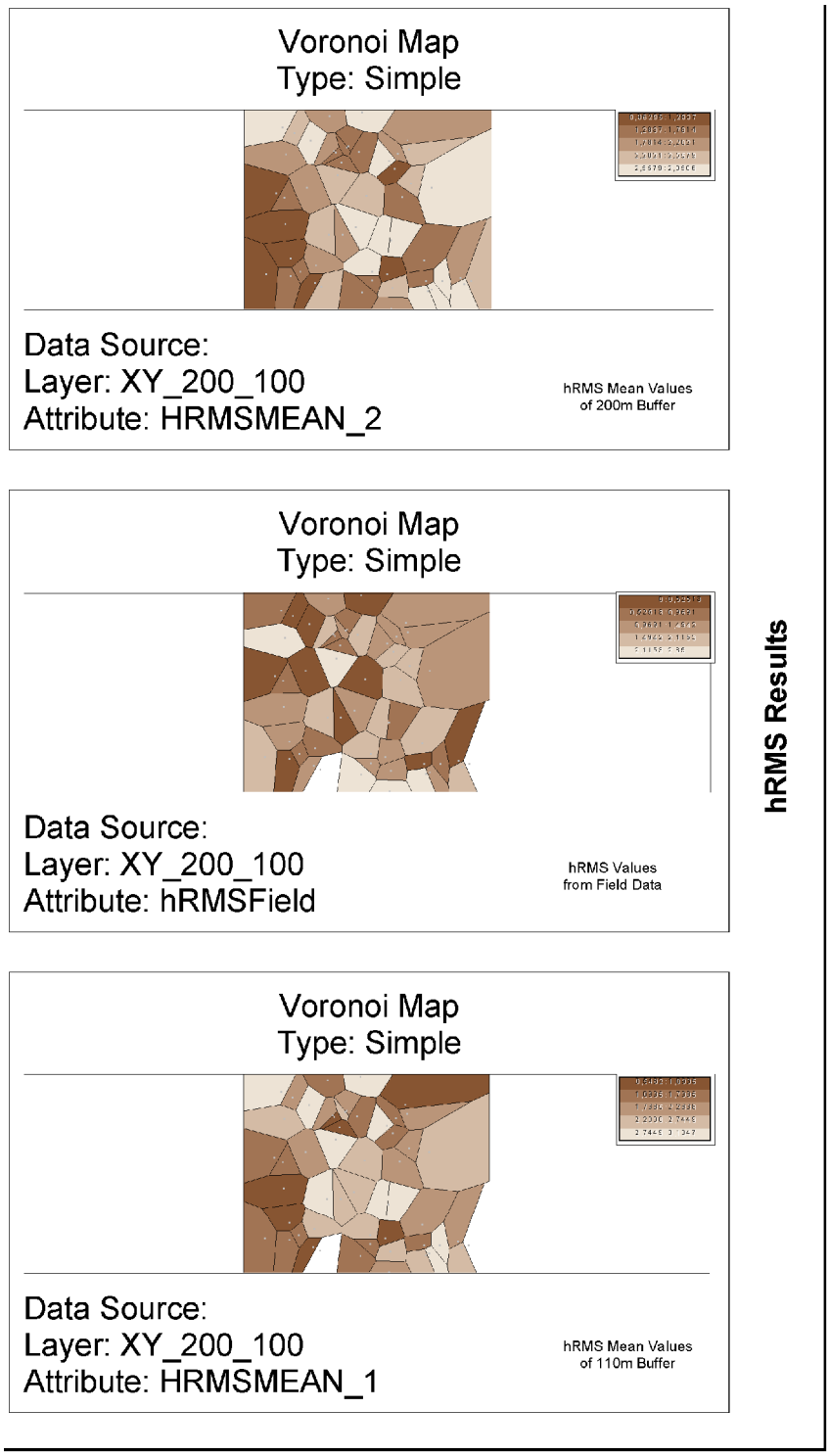

APPENDIX M. STATISTICS.

Site	Hrms_in_field	HH2	Hrms2	Zi2	Hrms1	Zi1
2	0.51	20.9083	1.70594001	1.10713995	1.51612997	1.15665996
3	2.25	21.6849	2.73580003	1.01867998	2.90136003	1.01954997
6	1.07	21.0725	2.13533998	1.01493001	1.88303006	0.95893198
7	1.47	22.244	1.81675994	1.35977006	0.97297299	1.49948001
8	0.79	20.7892	1.09502995	0.89775002	0.95999998	0.80686098
10	1.77	21.2765	1.61108005	0.96712101	1.01364005	0.88539702
16	1.6	21.0374	1.77607	1.13382995	1.77636003	1.16272998
19	0.96	20.7702	0.92142898	0.82250601	1.27533996	0.839504
22	2.32	21.436	1.51613998	1.04633999	1.32196999	0.87693298
25	1.58	20.9351	1.61585999	0.92409998	1.49491	0.97957402
26	1.1	21.6015	1.95139003	1.06277001	1.96273005	1.01943004
28	0.92	21.82	2.62641001	1.18779004	2.70363998	1.14321005
30	1.39	22.5873	1.65799999	1.17079997	0.830769	1.18909001
39	1.08	20.7391	0.862948	0.896043	0.93272698	0.92882502
41	1	21.3488	2.15557003	0.95183998	1.47567999	0.86902499
43	1.52	21.4788	2.60221004	1.05660999	2.54727006	1.05817997
48	0.89	21.2581	2.73986006	1.04114997	3.00226998	1.11321998
48	1.95	21.2601	2.74301004	1.04042995	3.00226998	1.11249006
49	1.85	21.2554	2.60468006	1.17367005	2.3447001	1.14119005
51	0.79	21.4268	2.28298998	1.12331998	2.17972994	1.08842003
52	1.25	21.5152	2.82356	1.15840006	3.13468003	1.15627003
54	1.76	21.0036	1.84985995	0.94723201	1.49954998	0.87920803
55	2.85	21.4204	2.64650011	1.05061996	2.43559003	1.06677997
56	0.55	21.2961	1.88817	1.02350998	2.10090995	1.10230005
57	1.39	21.2917	1.97478998	1.01382005	2.30864	1.09998
61	1.38	21.2454	2.3566699	1.10279	2.03999996	1.10500002
62	0.66	20.88	1.44254005	0.89560002	1.72387004	0.98858202
64	1.07	21.3088	2.85861993	0.94662303	2.91167998	0.97834098
73	0.92	21.504	2.09309006	1.11152995	2.30091	1.08539999
74	0.45	21.0044	1.69695997	0.930143	1.65602005	0.90470302
76	1.13	21.0261	1.92548001	1.12267005	2.06413007	1.18396997
79	1.69	21.2983	2.83397007	1.01015997	2.90598989	1.02225006
85	1.02	23.0698	1.57581997	1.37291002	1.89273	1.38156998
90	1.84	22.6822	1.25136995	1.31740999	1.40987003	1.48064995
92	1.58	21.3561	2.54863	1.05857003	3.00091004	1.02091002
93	2.19	22.7692	1.61003995	1.28713	1.30682003	1.32939994
102	1.46	21.3151	2.21193004	0.97141403	2.47788	1.01266003
103	1.24	21.2384	2.4145999	1.10316002	2.39591002	1.03840995
109	1.41	20.7529	0.96317202	0.85464799	0.70138901	0.869874
112	1.84	22.2817	1.70000005	1.32804	1.35385001	1.31742001
114	0.76	21.1785	2.24022007	0.97910202	2.06860995	0.95694703
117	2.38	22.8754	1.60792994	1.25409997	1.83182001	1.28995001
0	2.5	21.6799	2.5427599	1.16789997	3.09139991	1.17707002

Correlation	Hrms_in_field	Hrms1
Hrms_in_field	1	
Hrms1	0.117810979	1

SUMMARY OUTPUT

Regression Statistics	
Multiple R	0.117810979
R Square	0.013879427
Adjusted R Square	-0.010172295
Standard Error	0.702000169
Observations	43

ANOVA

	df	SS	MS	F	Significance F
Regression	1	0.284380492	0.284380492	0.577065841	0.451810671
Residual	41	20.20497372	0.492804237		
Total	42	20.48935421			

	Coefficients	Standard Error	t Stat	P-value	Lower 95%	Upper 95%	Lower 99.0%	Upper 99.0%
Intercept	1.768585449	0.285957005	6.184794971	2.3617E-07	1.191083567	2.346087331	0.996163734	2.541007164
Hrms_in_field	0.144045964	0.189621864	0.759648499	0.451810671	-0.238903155	0.526995083	-0.368157068	0.656248997

	Hrms_in_fiel	Hrms2
Hrms_in_fi	1	
Hrms2	0.174432	1

SUMMARY OUTPUT

Regression Statistics	
Multiple R	0.174432
R Square	0.030426
Adjusted F	0.006778
Standard E	0.558087
Observatio	43

ANOVA

	df	SS	MS	F	ignificance F
Regressior	1	0.400737	0.400737	1.286633	0.263258
Residual	41	12.76992	0.311461		
Total	42	13.17065			

	Coefficients	tandard Err	t Stat	P-value	Lower 95%	Upper 95%	ower 99.0%	pper 99.0%
Intercept	1.765845	0.227335	7.767601	1.39E-09	1.306733	2.224957	1.151773	2.379917
Hrms_in_fi	0.170994	0.150749	1.134299	0.263258	-0.13345	0.475437	-0.23621	0.578193

	Hrms_in_fiel	Zi1
Hrms_in_fi	1	
Zi1	0.240316	1

SUMMARY OUTPUT

Regression Statistics	
Multiple R	0.240316
R Square	0.057752
Adjusted F	0.03477
Standard E	0.160832
Observatio	43

ANOVA

	df	SS	MS	F	ignificance F
Regressior	1	0.065002	0.065002	2.512947	0.120598
Residual	41	1.060541	0.025867		
Total	42	1.125543			

	Coefficients	tandard Err	t Stat	P-value	Lower 95%	Upper 95%	ower 99.0%	pper 99.0%
Intercept	0.980357	0.065514	14.96404	3.28E-18	0.848048	1.112665	0.803391	1.157322
Hrms_in_fi	0.068868	0.043443	1.585228	0.120598	-0.01887	0.156603	-0.04848	0.186216

	Hrms_in_fiel	Zi2
Hrms_in_fi	1	
Zi2	0.298208	1

SUMMARY OUTPUT

Regression Statistics	
Multiple R	0.298208
R Square	0.088928
Adjusted F	0.066707
Standard E	0.131731
Observatio	43

ANOVA

	df	SS	MS	F	ignificance F
Regressior	1	0.069446	0.069446	4.001941	0.0521
Residual	41	0.711474	0.017353		
Total	42	0.78092			

	Coefficients	tandard Err	t Stat	P-value	Lower 95%	Upper 95%	ower 99.0%	pper 99.0%
Intercept	0.970322	0.05366	18.08276	3.8E-21	0.861954	1.078691	0.825377	1.115268
Hrms_in_fi	0.071183	0.035583	2.000485	0.0521	-0.00068	0.143043	-0.02493	0.167298

	Hrms1	Hrms2
Hrms1	1	
Hrms2	0.889112	1

SUMMARY OUTPUT

Regression Statistics	
Multiple R	0.889112
R Square	0.79052
Adjusted F	0.785411
Standard E	0.259408
Observatio	43

ANOVA

	df	SS	MS	F	ignificance F
Regressior	1	10.41166	10.41166	154.7226	1.68E-15
Residual	41	2.75899	0.067292		
Total	42	13.17065			

	Coefficients	tandard Err	t Stat	P-value	Lower 95%	Upper 95%	ower 99.0%	pper 99.0%
Intercept	0.60064	0.119629	5.020865	1.05E-05	0.359045	0.842235	0.277501	0.923779
Hrms1	0.712846	0.057308	12.43875	1.68E-15	0.59711	0.828583	0.558046	0.867647

	HH2	Hrms1
HH2	1	
Hrms1	-0.04125	1

SUMMARY OUTPUT

Regression Statistics	
Multiple R	0.041248
R Square	0.001701
Adjusted F	-0.02265
Standard E	0.706322
Observatio	43

ANOVA

	df	SS	MS	F	ignificance F
Regressior	1	0.034861	0.034861	0.069877	0.79284
Residual	41	20.45449	0.49889		
Total	42	20.48935			

	Coefficients	tandard Err	t Stat	P-value	Lower 95%	Upper 95%	ower 99.0%	pper 99.0%
Intercept	3.008423	3.929734	0.765554	0.448327	-4.92784	10.94468	-7.6065	13.62335
HH2	-0.04838	0.183022	-0.26434	0.79284	-0.418	0.321239	-0.54276	0.445995

	HH2	Hrms2
HH2	1	
Hrms2	0.002859	1

SUMMARY OUTPUT

Regression Statistics	
Multiple R	0.002859
R Square	8.17E-06
Adjusted F	-0.02438
Standard E	0.566774
Observatio	43

ANOVA

	df	SS	MS	F	ignificance F
Regressior	1	0.000108	0.000108	0.000335	0.985484
Residual	41	13.17055	0.321233		
Total	42	13.17065			

	Coefficients	tandard Err	t Stat	P-value	Lower 95%	Upper 95%	ower 99.0%	pper 99.0%
Intercept	1.947257	3.153339	0.617522	0.540305	-4.42104	8.315555	-6.57048	10.465
HH2	0.002688	0.146862	0.018305	0.985484	-0.29391	0.299283	-0.39401	0.39939

	HH2	Zi1
HH2	1	
Zi1	0.779453	1

SUMMARY OUTPUT

Regression Statistics	
Multiple R	0.779453
R Square	0.607547
Adjusted F	0.597975
Standard E	0.103797
Observatio	43

ANOVA

	df	SS	MS	F	ignificance F
Regressior	1	0.68382	0.68382	63.47105	7.37E-10
Residual	41	0.441723	0.010774		
Total	42	1.125543			

	Coefficients	tandard Err	t Stat	P-value	Lower 95%	Upper 95%	ower 99.0%	pper 99.0%
Intercept	-3.52239	0.577489	-6.0995	3.12E-07	-4.68866	-2.35613	-5.0823	-1.96249
HH2	0.214275	0.026896	7.966872	7.37E-10	0.159958	0.268592	0.141625	0.286925

	HH2	Zi2
HH2	1	
Zi2	0.836323	1

SUMMARY OUTPUT

Regression Statistics	
Multiple R	0.836323
R Square	0.699436
Adjusted F	0.692105
Standard E	0.075662
Observatio	43

ANOVA

	df	SS	MS	F	ignificance F
Regressior	1	0.546203	0.546203	95.41003	2.91E-12
Residual	41	0.234717	0.005725		
Total	42	0.78092			

	Coefficients	tandard Err	t Stat	P-value	Lower 95%	Upper 95%	ower 99.0%	pper 99.0%
Intercept	-3.04045	0.42096	-7.22265	8.01E-09	-3.8906	-2.1903	-4.17754	-1.90336
HH2	0.191504	0.019606	9.767806	2.91E-12	0.15191	0.231098	0.138546	0.244462

	Zi1	Zi2
Zi1	1	
Zi2	0.927581	1

SUMMARY OUTPUT

Regression Statistics	
Multiple R	0.927581
R Square	0.860406
Adjusted F	0.857001
Standard E	0.061905
Observatio	43

ANOVA

	df	SS	MS	F	ignificance F
Regressior	1	0.968423	0.968423	252.7086	3.92E-19
Residual	41	0.157119	0.003832		
Total	42	1.125543			

	Coefficients	tandard Err	t Stat	P-value	Lower 95%	Upper 95%	ower 99.0%	pper 99.0%
Intercept	-0.11474	0.075538	-1.51896	0.136446	-0.26729	0.037813	-0.31878	0.089302
Zi2	1.1136	0.070052	15.89681	3.92E-19	0.972128	1.255073	0.924378	1.302823

	HH2	rms_in_field
HH2	1	
Hrms_in_fi	0.370213	1

SUMMARY OUTPUT

Regression Statistics	
Multiple R	0.370213
R Square	0.137058
Adjusted F	0.116011
Standard E	0.559885
Observatio	43

ANOVA

	df	SS	MS	F	ignificance F
Regressior	1	2.041285	2.041285	6.511883	0.01454
Residual	41	12.8523	0.313471		
Total	42	14.89358			

	Coefficients	tandard Err	t Stat	P-value	Lower 95%	Upper 95%	ower 99.0%	pper 99.0%
Intercept	20.92366	0.228067	91.74358	4.44E-49	20.46307	21.38425	20.30761	21.53971
Hrms_in_fi	0.385925	0.151234	2.551839	0.01454	0.080502	0.691348	-0.02259	0.794436